AWARD NUMBER: W81XWH-15-1-0725

TITLE: Multifunctional PSCA Antibody Fragments for PET and Optical Prostate Cancer Imaging

PRINCIPAL INVESTIGATOR: Anna M. Wu

CONTRACTING ORGANIZATION: University of California, Los Angeles
4B557
10889 Wilshire Blvd. Suite 700
Los Angeles, CA 90095-0001

REPORT DATE: December 2019

TYPE OF REPORT: Final

PREPARED FOR: U.S. Army Medical Research and Materiel Command
Fort Detrick, Maryland 21702-5012

REPORT DOCUMENTATION PAGE

Form Approved
OMB No. 0704-0188

1. REPORT DATE	2. REPORT TYPE	3. DATES COVERED
December 2019	Final	30 Sep 2015 - 29 Sep 2019

4. TITLE AND SUBTITLE

Multifunctional PSCA Antibody Fragments for PET and Optical Prostate Cancer Imaging

5a. CONTRACT NUMBER

5b. GRANT NUMBER
W81XWH-15-1-0725

5c. PROGRAM ELEMENT NUMBER

6. AUTHOR(S)
Anna M. Wu

E-Mail: awu@mednet.ucla.edu

5d. PROJECT NUMBER

5e. TASK NUMBER

5f. WORK UNIT NUMBER

7. PERFORMING ORGANIZATION NAME(S) AND ADDRESS(ES)

University of California, Los Angeles
4B557
10889 Wilshire Blvd. Suite 700
Los Angeles CA 90095-0001

8. PERFORMING ORGANIZATION REPORT NUMBER

9. SPONSORING / MONITORING AGENCY NAME(S) AND ADDRESS(ES)

U.S. Army Medical Research and Materiel Command
Fort Detrick, Maryland 21702-5012

10. SPONSOR/MONITOR'S ACRONYM(S)

11. SPONSOR/MONITOR'S REPORT NUMBER(S)

12. DISTRIBUTION / AVAILABILITY STATEMENT

Approved for Public Release; Distribution Unlimited

13. SUPPLEMENTARY NOTES

14. ABSTRACT

The goals of this funding were to develop and evaluate universal optimized cys-diabody and cys-minibody fragments against prostate stem cell antigen (PSCA) for PET imaging of prostate cancer. During the three-year project period, we developed and produced a novel anti-PSCA cys-minibody and employed it for singly- and dually-labeled (PET or PET/optical) imaging in mouse models of prostate cancer. In addition, focusing on the smaller anti-PSCA cys-diabody, we demonstrated dual labeling and imaging in models of pancreatic cancer, which also express PSCA. Novel linker chemistry was developed to attach both fluorescent labels and F-18 in a single moiety. This tag, fluorescently labeled, was site-specifically conjugated to the anti-PSCA cys-diabody and rapidly labeled with F-18 using click chemistry. Successful sequential microPET and optical imaging were demonstrated in mouse models. As all these agents are based on a fully humanized antibody, they would be suitable for clinical translation.

15. SUBJECT TERMS

NONE LISTED

16. SECURITY CLASSIFICATION OF:			17. LIMITATION OF ABSTRACT	18. NUMBER OF PAGES	19a. NAME OF RESPONSIBLE PERSON
a. REPORT	b. ABSTRACT	c. THIS PAGE			USAMRMC
U	U	U	UU	64	19b. TELEPHONE NUMBER *(include area code)*

Table of Contents

Page

1. INTRODUCTION

Imaging remains a major unmet need in the management of prostate cancer. We are developing imaging probes based on engineered antibodies that recognize PSCA (prostate stem cell antigen), a cell surface protein highly expressed in prostate cancer. These engineered antibody fragments (cys-minibodies and cys-diabodies) can be labeled with radioisotopes for non-invasive PET imaging for use at multiple points in the prostate cancer treatment continuum, including staging at diagnosis, monitoring treatment, and re-staging at various points during management. Engineered fragments can also be labeled with fluorescent dyes for visual guidance in an intraoperative setting to ensure complete resection with negative margins. In this project, dually-labeled PSCA imaging agents are being developed that can be used for pre- and intra-operative detection of prostate cancer.

2. KEYWORDS

Prostate cancer, imaging, antibody fragment, positron emission tomography, fluorescence imaging, PSCA

3. ACCOMPLISHMENTS

What were the major goals of the project?

Specific Aim 1. Develop universal optimized cys-diabody and cys-minibody fragments against PSCA for PET imaging of prostate and pancreatic cancer.
Subtasks:

Major Task 1. Develop and evaluate cys-diabody and cys-minibody fragments
Major Task 2. Design, optimize and test multifunctional, F-18, and alternatively labeled fragments
Major Task 3. New technologies: alternative site-specific labeling methods, use of click chemistry

Specific Aim 2. Evaluate the ability of lead PSCA fragments to imaging prostate cancer in disease progression in xenograft and genetically engineered models of prostate cancer
Subtasks:
Major Task 4. Image bone and lymph node in xenograft models
Major Task 5. Image transgenic mouse models
Major Task 6. Development and evaluation of singly labeled and optimized optical probes for surgery
Major Task 7. Development of dual labeled probes for PET and optical imaging.

For **Dr. Wu (Partnering PI)** the subtasks were:

Major Task 1

Subtask 1. Produce and purify A2 cys-diabody and A2-cys-minibody in mg quantities (months 1-6) **Completed.**

Subtask 2. Optimize radiolabeling conditions with I-124 (tyrosine) and Zr-89 (DFO conjugation to lysine and cysteine residues). Confirm retention of binding by QCM and cell binding. (months 3-9) **Completed.**

Subtask 3. Conduct microPET imaging and biodistribution in subcutaneous models using I-124 and/or Zr-89; provide PET tracers to Aim 2. (months 6-18) **Completed.**

Major Task 2: Design, optimize, and evaluate cys-diabody and cys-minibody fragments.

Subtask 1: Optimize dual-labeling of cys-minibody and cys-diabody and confirm targeting and imaging in subcutaneous models. (months 12-18) **Completed.**

Subtask 2: Develop and establish cysteine specific F-18 labeling of A2 cys-diabody. (months 12-18) **Completed**.

Subtask 3: Conduct microPET imaging and biodistriubtion in subcutaneous models using F-18 cys-diabody. (months 14-24) **Completed**.

Subtask 4: Produce mannosylated proteins and develop cold chemistry for conjugation. (months 18-30) **Discontinued** previously due to lack of feasibility. Focus shifted to multifunctional linkers.

Subtask 5. Design multifunctional linkers, establish and optimize conjugation conditions. (months 12-36) **Completed.**

Subtask 6. Continue to provide PET, optical, and dual-labeled probes to Aims 2 and 3. (months 1-36) **Completed**.

Major Task 3: New technologies

Subtask 1: Focus on alternative approaches including radiolabeling mannosylated cys-diabody and cys-minibody. **Discontinued** previously due to poor labeling efficiency. Efforts shifted to multifunctional linkers.

Subtask 2: Continue work on multifunctional linkers to produce labeled cys-diabody with "click" handle. (months 12-36) **Completed**.

Subtask 3. Work on "click" F-18 radiolabeling of multifunctionally modified cys-diabody. (months 24-36) **Completed**.

Major Task 4: Image bone and lymph node in xenograft models

Subtask 1: Image bone implant/metastatic models with best approach labeling cys-diabody and cys-minibody. (months 6-24) **Provided to Partnering PI**.

Major Task 7: Development of dual labeled probes for PET and optical imaging

Subtask 1: Dual labeling for optical/PET imaging. (months 24-36) **Completed**.

Subtask 2: In vivo dual labeling in xenograft and possibly transgenic model systems. (months 24-36) **Completed**.

What was accomplished under these goals?

Results from these studies are provided in the publications in the Appendix.

1. Tsai, W.-T. K., Zettlitz, K.A., Tavaré, R., Kobayashi, N., Reiter, R.E., and **Wu, A.M.** (2018) Dual-modality PET/fluorescence imaging of prostate cancer with anti-PSCA cys-minibody. *Theranostics* 8:5903-5914.

2. Zhang, M., Kobayashi, N., Zettlitz, K.A., Kono, E.E., Yamashiro, J.M., Tsai, W.-T. K., Zhang, Z. K., Tran, C.P., Wang, C., Guan, J., **Wu, A.M.,** and Reiter, R.E. (2019) Near-infrared-dye labeled anti-prostate stem cell antigen (PSCA) A11 minibody enables real-

time fluorescence imaging and targeted surgery in translational mouse models. *Clin. Canc. Res.* 25:188-200. Doi: 10.1158/1078-0432.CCR-18-1382.

3. Zettlitz, K.A., Waldmann, C.M., Tsai, W.-T.K., Tavaré, R., Collins, J., Murphy, J.M., and **Wu, A.M**. (2019). A dual-modality linker enables site-specific conjugation of antibody fragments for ^{18}F-immunoPET and fluorescence imaging. *J. Nucl. Med.* in press.

What opportunities for training and professional development has the project provided?

Nothing to report.

How were results disseminated to communities of interest?

Nothing to report

What do you plan to do during the next reporting period to accomplish the goals?

Nothing to report.

4. IMPACT

What was the impact on the development of the principle discipline of the project?

Nothing to report.

What was the impact on other disciplines?

Nothing to report.

What was the impact on technology transfer?

Nothing to report.

What was the impact on society beyond science and technology?

Nothing to report.

5. CHANGES/PROBLEMS

Nothing to report.

6. PRODUCTS

Publications, conference papers, and presentations

Journal publications:

1. Sonn, G.A., Behesnilian, A.S., Jiang, Z.K., Zettlitz, K.A., Lepin, E.J., Bentolilla, L.A., Knowles, S.M., Lawrence, D., **Wu, A.M.**, and Reiter, R.E. (2016) Fluorescent image-guided surgery with an anti-Prostate Stem Cell Antigen (PSCA) diabody enables targeted resection of mouse prostate cancer xenografts in real-time. *Clin. Canc. Res.* 22:1403-1412.

2. Tsai, W.-T. K., Zettlitz, K.A., Tavaré, R., Kobayashi, N., Reiter, R.E., and **Wu, A.M.** (2018) Dual-modality PET/fluorescence imaging of prostate cancer with anti-PSCA cys-minibody. *Theranostics* 8:5903-5914.

3. Zhang, M., Kobayashi, N., Zettlitz, K.A., Kono, E.E., Yamashiro, J.M., Tsai, W.-T. K., Zhang, Z. K., Tran, C.P., Wang, C., Guan, J., **Wu, A.M.,** and Reiter, R.E. (2019) Near-infrared-dye labeled anti-prostate stem cell antigen (PSCA) A11 minibody enables real-time fluorescence imaging and targeted surgery in translational mouse models. *Clin. Canc. Res.* 25:188-200. Doi: 10.1158/1078-0432.CCR-18-1382.

4. Zettlitz, K.A., Waldmann, C.M., Tsai, W.-T.K., Tavaré, R., Collins, J., Murphy, J.M., and **Wu, A.M**. (2019). A dual-modality linker enables site-specific conjugation of antibody fragments for ^{18}F-immunoPET and fluorescence imaging. *J. Nucl. Med.* in press.

Submitted:

1. Zettlitz, K.A., Tsai, W.-T. K., Knowles, S.M., Salazar, F.B., Kobayashi, N., Reiter, R.E., and **Wu, A.M.** ^{89}Zr-A2cDb immuno-PET of prostate cancer in a human prostate stem cell antigen knock in (hPSCA KI) syngeneic model.

In preparation:

1. Gamache, R., Zettlitz, K.A., Tsai, W.-T. K., **Wu, A.M.** and Murphy, J.M. Site-specific construction of a modular antibody fragment for in vivo ^{18}F-PET/NIRF molecular imaging of prostate stem call antigen (PSCA)

2. Zettlitz, K.A., Gamache, R., Tsai, W.-T. K., Murphy, J.M. and **Wu, A.M.** A tetra-functional linker for site-specific conjugation of antibody fragments towards immunoPET, near-infrared fluorescence (NIRF) imaging and radioimmunotherapy (RIT)

Abstracts/conference presentations:

1. Tsai, Wen-ting, Tavaré, R., Zettlitz, K.A., Salazar, F.B., Knowles, S., Reiter, R., and **Wu, A.M.** (2015). Dual modality immunoPET/fluorescence imaging of prostate cancer. World Molecular Imaging Congress, Honolulu, HI.

2. Tsai, W.-T., Tavaré, R., Zettlitz, K.A., Salazar, F.B., Reiter, R.E., and **Wu, A.M**. (2015) Dual-modality immunoPET/fluorescence imaging of prostate cancer using anti-PSCA cys-minibody. Antibody Engineering and Therapeutics 2015, San Diego, CA.

3. Tsai, W.-T., Zettlitz, K., Tavaré, R., Salazar, F., Reiter, R., and **Wu, A**. Dual-modality immune-PET/fluorescence imaging of prostate cancer using anti-PSCA A11 cys-minibody. (2016) Antibody Technology Resource Center Symposium, San Francisco, CA.

4. Tsai, W., Zettlitz, K., Tavaré, R., Salazar, F., Reiter, R., and Wu, A. (2017) Dual-modality immunoPET/fluorescence imaging of prostate cancer utilizing ^{89}Zr- or ^{124}I-anti-PSCA cys-minibody. American Association for Cancer Research Annual Meeting; 2017 April 1-5. Washington, DC.

5. Zettlitz, K., Tsai, W., Reiter, R., and **Wu, A**. (2017) Dual-modality immunoPET and NIRF imaging of pancreatic cancer using an anti-PSCA cys-diabody. World Molecular Imaging Congress, Philadelphia, PA.

6. Tsai, W.-T.,K., Zettlitz, K.A., Tavaré, R., Reiter, R.E., and Wu, A.M. (2017) ImmunoPET/fluorescence imaging of PSCA-positive prostate cancer using A11 cys-minibody. World Molecular Imaging Congress, Philadelphia, PA.

7. Zettlitz, K.A., Waldmann, C.M., Tsai, W.-T. K., Murphy, J.M., and **Wu, A.M**. (2017) A dual-modality linker for 18F-immunoPET and fluorescence imaging of prosatate cancer using an anti-prostate stem cell antigen (PSCA) cys-diabody. Antibody Engineering and Therapeutics, San Diego, CA.

8. Zettlitz, K.A., Tsai,W.-T. K., Kobayashi, N., Reiter, R.E., and **Wu, A.M**. (2018) ImmunoPET of prostate cancer in a human prostate stem cell antigen knock in (hPSCA KI) syngeneic mouse model. World Molecular Imaging Congress, Seattle, WA.

9. Zettlitz, K.A., Gamache, R.F., Tsai, W.-T. K., Murphy, J.M., and **Wu, A.M.** (2018) A tetra-functional linker enables site-specific conjugation of antibody fragments for immunoPET, near-infrared fluorescence (NIRF) imaging and radioimmunotherapy (RIT). World Molecular Imaging Congress, Seattle, WA.

7. PARTICIPANTS AND OTHER COLLABORATING ORGANIZATIONS

What individuals have worked on the project?

Three year totals:

Name:	*Anna M. Wu*
Project Role:	Partnering Principal Investigator
Researcher Identifier (e.g. ORCID ID):	0000-0001-8487-823X
Nearest person month worked:	4
Contribution to Project:	*Dr. Wu oversaw all aspects of work performed and accomplished to-date.*

Funding Support:	

Name:	*Jennifer Murphy*
Project Role:	Co-Investigator
Researcher Identifier (e.g. ORCID ID):	
Nearest person month worked:	4
Contribution to Project:	*Dr. Murphy performed work on the design and evaluation of the chemical and radiochemical strategies for combined PET/optical labeling.*
Funding Support:	

Name:	*Kirstin Zettlitz*
Project Role:	Assistant Researcher
Researcher Identifier (e.g. ORCID ID):	
Nearest person month worked:	11
Contribution to Project:	*Dr. Zettlitz performed work on site-specific conjugation, radiolabeling, and imaging of engineered antibody fragments.*
Funding Support:	

Name:	*Maruthi Narayanam*
Project Role:	Postdoctoral Researcher
Researcher Identifier (e.g. ORCID ID):	
Nearest person month worked:	3
Contribution to Project:	*Dr. Narayanam performed work on developing methods for F-18 labeling of engineered antibody fragments.*
Funding Support:	

Name:	*Christopher Waldmann*
Project Role:	Postdoctoral Researcher
Researcher Identifier (e.g. ORCID ID):	
Nearest person month worked:	2

Contribution to Project:	*Dr. Waldmann performed work on developing methods for F-18 labeling of engineered antibody fragments.*
Funding Support:	

Name:	*Felix Bergara Salazar*
Project Role:	Staff Research Associate
Researcher Identifier (e.g. ORCID ID):	
Nearest person month worked:	1
Contribution to Project:	*Mr. Bergara performed work on imaging in murine tumor models.*
Funding Support:	

Name:	*Amanda Freise*
Project Role:	Graduate Student Researcher
Researcher Identifier (e.g. ORCID ID):	
Nearest person month worked:	2
Contribution to Project:	*Ms. Freise performed work on site-specific conjugation, radiolabeling, and imaging of engineered antibody fragments.*
Funding Support:	

Name:	*Arely Perez Rodriguez*
Project Role:	Student Researcher
Researcher Identifier (e.g. ORCID ID):	
Nearest person month worked:	2
Contribution to Project:	*Ms. Perez performed work on buffer preparation and sample analysis.*
Funding Support:	

Has there been a change in the active other support of the PD/PI(s) or senior/key personnel since the last reporting period?

Nothing to report.

What other organizations were involved as partners?

Nothing to report.

8. SPECIAL REPORTING REQUIREMENTS

Collaborative awards

This report covers the activities of the Partner PI, Dr. Anna Wu.

9. APPENDICES

1. Tsai, W.-T. K., Zettlitz, K.A., Tavaré, R., Kobayashi, N., Reiter, R.E., and **Wu, A.M.** (2018) Dual-modality PET/fluorescence imaging of prostate cancer with anti-PSCA cys-minibody. *Theranostics* 8:5903-5914.

2. Zhang, M., Kobayashi, N., Zettlitz, K.A., Kono, E.E., Yamashiro, J.M., Tsai, W.-T. K., Zhang, Z. K., Tran, C.P., Wang, C., Guan, J., **Wu, A.M.,** and Reiter, R.E. (2019) Near-infrared-dye labeled anti-prostate stem cell antigen (PSCA) A11 minibody enables real-time fluorescence imaging and targeted surgery in translational mouse models. *Clin. Canc. Res.* 25:188-200. Doi: 10.1158/1078-0432.CCR-18-1382.

3. Zettlitz, K.A., Waldmann, C.M., Tsai, W.-T.K., Tavaré, R., Collins, J., Murphy, J.M., and **Wu, A.M**. (2019). A dual-modality linker enables site-specific conjugation of antibody fragments for ^{18}F-immunoPET and fluorescence imaging. *J. Nucl. Med.* in press.

IVYSPRING INTERNATIONAL PUBLISHER

Theranostics

2018; 8(21): 5903-5914. doi: 10.7150/thno.27679

Research Paper

Dual-Modality ImmunoPET/Fluorescence Imaging of Prostate Cancer with an Anti-PSCA Cys-Minibody

Wen-Ting K Tsai[1], Kirstin A Zettlitz[1], Richard Tavaré[1,2], Naoko Kobayashi[3], Robert E Reiter[3], Anna M Wu[1,4]✉

1. Crump Institute for Molecular Imaging, Department of Molecular and Medical Pharmacology, David Geffen School of Medicine, UC Los Angeles
2. Current address: Regeneron Pharmaceuticals, Inc., Tarrytown, New York
3. Department of Urology, David Geffen School of Medicine, UC Los Angeles
4. Current address: Department of Molecular Imaging and Therapy, Beckman Research Institute, City of Hope, Duarte

✉ Corresponding author: Anna M Wu, Department of Molecular Imaging and Therapy, Beckman Research Institute, City of Hope, 1500 E. Duarte Rd. Duarte, CA 91010, USA. Tel: 1 (626) 218-8051; email: awu@coh.org

Received: 2018.06.05; Accepted: 2018.09.04; Published: 2018.11.12

Abstract

Inadequate diagnostic methods for prostate cancer lead to over- and undertreatment, and the inability to intraoperatively visualize positive margins may limit the success of surgical resection. Prostate cancer visualization could be improved by combining the complementary modalities of immuno-positron emission tomography (immunoPET) for preoperative disease detection, and fluorescence imaging-guided surgery (FIGS) for real-time intraoperative tumor margin identification. Here, we report on the evaluation of dual-labeled humanized anti-prostate stem cell antigen (PSCA) cys-minibody (A11 cMb) for immunoPET/fluorescence imaging in subcutaneous and orthotopic prostate cancer models.

Methods: A11 cMb was site-specifically conjugated with the near-infrared fluorophore Cy5.5 and radiolabeled with ^{124}I or ^{89}Zr. ^{124}I-A11 cMb-Cy5.5 was used for successive immunoPET/fluorescence imaging of prostate cancer xenografts expressing high or moderate levels of PSCA (22Rv1-PSCA and PC3-PSCA). ^{89}Zr-A11 cMb-Cy5.5 dual-modality imaging was evaluated in an orthotopic model. *Ex vivo* biodistribution at 24 h was used to confirm the uptake values, and tumors were visualized by post-mortem fluorescence imaging.

Results: A11 cMb-Cy5.5 retained low nanomolar affinity for PSCA-positive cells. Conjugation conditions were established (dye-to-protein ratio of 0.7:1) that did not affect the biodistribution, pharmacokinetics, or clearance of A11 cMb. ImmunoPET using dual-labeled ^{124}I-A11 cMb-Cy5.5 showed specific targeting to both 22Rv1-PSCA and PC3-PSCA s.c. xenografts in nude mice. *Ex vivo* biodistribution confirmed specific uptake to PSCA-expressing tumors with 22Rv1-PSCA:22Rv1 and PC3-PSCA:PC3 ratios of 13:1 and 5.6:1, respectively. Consistent with the immunoPET, fluorescence imaging showed a strong signal from both 22Rv1-PSCA and PC3-PSCA tumors compared with non-PSCA expressing tumors. In an orthotopic model, ^{89}Zr-A11 cMb-Cy5.5 immunoPET was able to detect intraprostatically implanted 22Rv1-PSCA cells. Importantly, fluorescence imaging clearly distinguished the prostate tumor from surrounding seminal vesicles.

Conclusion: Dual-labeled A11 cMb specifically visualized PSCA-positive tumor by successive immunoPET/fluorescence, which can potentially be translated for preoperative whole-body prostate cancer detection and intraoperative surgical guidance in patients.

Key words: immunoPET, fluorescence, prostate cancer, antibody fragment, molecular imaging

Introduction

Despite recent advances in prostate cancer treatment, definitive diagnosis requires taking biopsy cores, and there is a critical demand for improved disease detection, staging and stratification. Noninvasive imaging methods, including ultrasound, magnetic resonance imaging (MRI), positron emission

tomography (PET), and single-photon emission computed tomography (SPECT), have been adapted to aid prostate cancer diagnosis, yet each has its limitations [1, 2]. For example, ^{99m}Tc-methylene diphosphonate bone scintigraphy is widely used to detect bone metastases, but it is not specific for prostate cancer [2]. MRI is a highly sensitive and reliable strategy for local staging and identification of soft tissue lesions, but may not be sensitive enough to detect lymph node metastases or differentiate from inflammation [1]. Additional challenges occur during surgery, where difficulty visualizing positive margins, including extracapsular extensions and lymph node metastases, can increase the probability of incomplete resection and therefore tumor recurrence [3, 4]. Wide-resection strategies can damage surrounding tissues such as rectum, urinary sphincter, and erectile nerves, which can lead to urinary incontinence and impotence [5]. The transition to robot-assisted radical prostatectomy has improved oncological, continence, and potency outcomes [6], and this surgical advancement can be complemented with disease-specific optical imaging agents for further improvement in patient outcome. An effective imaging agent can provide a preoperative whole-body image by PET, and intraoperatively identify tumor margins by fluorescence to improve surgical outcome.

Molecular imaging of prostate cancer by PET has been successful in identifying primary and metastatic disease, and it is a powerful tool to guide therapy selection, stratify patients, and monitor response to treatment. The most commonly used PET tracer, 2-deoxy-2-[^{18}F]fluoro-D-glucose (^{18}F-FDG), had limited success in differentiating primary prostate carcinoma from hyperplasia due to the low metabolism of prostate cancer, and therefore other PET tracers have emerged. ^{11}C-choline, ^{18}F-fluorocholine, and ^{11}C-acetate are used to image lipogenesis in prostate cancer, while the recently approved ^{18}F-fluociclovine (FACBC) targets amino acid transport systems [7]. These processes are upregulated in prostate cancer, but they can also occur in benign tissues. Therefore, antibodies, antibody fragments, and peptides based on targeting prostate cancer biomarkers such as prostate-specific membrane antigen (PSMA) [8, 9] and gastrin-releasing peptide receptor (GRPR) [2, 10], have also been developed for PET imaging as well as therapy.

A promising target for imaging and therapy is Prostate Stem Cell Antigen (PSCA), a cell-surface marker upregulated in the majority of prostate cancers and metastases, as well as pancreatic, bladder, and stomach cancer [11]. Increased expression of PSCA correlates with more severe tumor stage, Gleason score, and progression towards androgen independence [12, 13], and pre-clinical molecular imaging has previously been used to detect PSCA-positive prostate [14-16] and pancreatic cancer [17]. As a cell-surface marker, PSCA is a promising target for prostate cancer imaging due to overexpression in primary prostate cancer (88-94%), bone metastases (87-100%), as well as lymph nodes and liver metastases (67%). PSCA can be targeted by immunoPET, which combines the high specificity of antibodies with the sensitivity of PET.

Engineered antibody fragments, such as the minibody (scFv-C_H3 dimer, 80 kDa), clear more quickly compared to full-length antibodies for high tumor-to-background images at short imaging times (next day for the minibody) [18]. The serum half-life ($t_{1/2}$) of the minibody (5-6 h in mice) pairs well with longer-lived radionuclides, including positron-emitting iodine-124 (^{124}I, $t_{1/2}$ = 4.2 days) and zirconium-89 (^{89}Zr, $t_{1/2}$ = 3.3 days), both of which also have been successfully used in the clinic [18]. Tumor uptake of ^{124}I and ^{89}Zr-minibodies peaks around 8 h post injection (p.i.), and unbound tracer is sufficiently cleared by 20 h p.i. to enable imaging in mice.

The humanized parental anti-PSCA A11 minibody (Mb) was previously radiolabeled for high-contrast immunoPET of PSCA-expressing prostate cancers [14]. Both ^{124}I-A11 Mb and ^{89}Zr-A11 Mb successfully targeted transduced (22Rv1-PSCA) and endogenous (LAPC-9) PSCA-expressing prostate cancer xenografts, and ^{124}I-A11 Mb resulted in higher tumor-to-tissue contrast images. Additionally, ^{124}I-A11 Mb was successfully used to monitor PSCA downregulation in LAPC-9 xenografts in response to enzalutamide treatment [15]. Therefore, we propose that A11 Mb can be modified and successfully employed for dual-modality PET imaging and fluorescence imaging.

Near-infrared fluorescence (NIRF) imaging-guided surgery has emerged as a tool to visualize tumor margins for improved resection [19, 20]. NIRF dyes (traditional window 700-900 nm, recently extended to 1,700 nm [21]) allow for light penetration at a greater depth (millimeters) than fluorophores in the visible light range (micrometers) [20], as well as decreased background fluorescence and scattering. NIR fluorophores used to conjugate to target-specific probes include IRDye800CW (available clinical grade), indocyanine green (ICG), and the cyanines Cy5, Cy5.5, or Cy7, which are more easily detected in a preclinical setting [20, 22]. For example, anti-prostate-specific membrane antigen (PSMA) antibody J591-ICG was used to successfully detect PSMA-positive tumors [23], and anti-PSMA antibody and antibody fragments-IR700 were evaluated as

photoimmunotherapy agents [24]. PSCA has also been targeted for FIGS of prostate cancer in a study using Cy5-labeled anti-PSCA A2 cys-diabody (A2 cDb) to detect tumors implanted intramuscularly to mimic invasive growth [25].

A dual-labeled molecule ensures that the radioactive and optical signals are carried on the same molecule, and therefore targeting and imaging will be consistent. Dual-labeled antibodies and peptides for SPECT/fluorescence and PET/fluorescence have been evaluated in several preclinical models [26] including PSMA-positive prostate cancer [27-30]. Indium-111-DOTA-girentuximab-IRDye800CW was successfully used in a recent clinical trial for preoperative and intraoperative guidance in renal cell carcinoma patients [31]. We propose that engineered antibody fragments are highly suited for dual-labeling without perturbation of their kinetics and targeting, and offer next-day high contrast immunoPET and fluorescence images. A recent study successfully used a dual-labeled antibody fragment, ^{124}I-A2 cDb-IRDye800CW, for same-day immuno-PET/fluorescence to detect PSCA-positive patient-derived pancreatic cancer xenografts [32]. Therefore, dual immunoPET/fluorescence imaging with an anti-PSCA antibody fragment could be used to detect PSCA-positive prostate cancer.

In the present study, a cysteine-modified humanized anti-PSCA A11 Mb (A11 cMb) was developed and dually labeled for successive immunoPET/fluorescence imaging. The efficacy was demonstrated in two subcutaneous models and one orthotopic prostate cancer model, and dual-labeled A11 cMb was successfully used to detect PSCA-positive tumors with both imaging modalities.

Methods

Protein production and characterization

Details of protein cloning, expression, and purification, and cell binding assays can be found in the supplemental methods.

Cell lines and tumor models

Details on cell lines and tumor models can be found in the supplemental methods. Briefly, the 22Rv1 human prostate cell line (ATCC CRL-2505) was previously transduced with retrovirus to express PSCA (22Rv1-PSCA) [33]. The PC3 human prostate cell line (ATCC CRL-1435) was previously transfected to express PSCA [33] and FLuc to produce the PC3-PSCA-FLuc cell line. Tumors were established in 8- to 10-week-old male nu/nu mice (*Foxn1^{nu}*, Jackson Laboratories). Bilateral s.c. tumors were implanted using 22Rv1 and 22Rv1-PSCA cells, or PC3 and PC3-PSCA-FLuc cells ($0.5\text{-}1\times10^6$), and allowed to grow to 100-200 mm^3 before imaging (measured bilaterally). 22Rv1-PSCA-FLuc cells (5×10^3) were implanted orthotopically, and the tumors were measured to be 1.8 ± 0.6 g at time of sacrifice. Protocols for all animal studies were approved by the UCLA Animal Research Committee.

Site-specific mal-Cy5.5 conjugation

A11 cMb was site-specifically labeled with maleimide-Cy5.5 (mal-Cy5.5) by selective reduction of and conjugation to C-terminal cysteines. In a typical reaction, 200 µg of protein at 1 mg/mL in phosphate-buffered saline (PBS) was reduced using a 2-fold molar excess of tris(2-carboxyethyl)phosphine (TCEP, Pierce) for 30 min at room temperature. Equimolar mal-Cy5.5 (Amersham, GE Healthcare) was added to the reduced A11 cMb for 2 h at room temperature. Excess mal-Cy5.5 was removed using a Micro Bio-Spin™ Size Exclusion Columns (Bio-Rad) pre-equilibrated with PBS. Dye-to-protein ratio (D:P) was determined by measuring the protein (280 nm) and Cy5.5 absorbance (675 nm) with a spectrophotometer (NanoDrop 2000). Successful conjugation was confirmed by sodium dodecyl sulfate polyacrylamide gel electrophoresis (SDS-PAGE) and size exclusion chromatography (SEC).

For SEC, a Superdex 200 10/30 GL column (GE Healthcare) was used with an ÄKTA purifier (GE Healthcare) with PBS as the mobile phase (0.5 mL/min). Absorbance at 280 nm (protein) and 675 nm (Cy5.5) was recorded. The following protein standards were used: beta-amylase (200 kDa), bovine serum albumin (66 kDa), and carbonic anhydrase (29 kDa) (Sigma).

SCN-DFO conjugation

A11 cMb was conjugated with the metal chelator p-isothiocyanatobenzyl-deferoxamine (p-SCN-Bn-DFO, B-705, Macrocyclics) for ^{89}Zr-radiolabeling [34]. In a typical reaction, 3-fold molar excess p-SCN-Bn-DFO was added to A11 cMb or A11 cMb-Cy5.5, and the reaction was immediately adjusted to pH 9 using 0.1 M sodium bicarbonate (1/10 volume). The reaction was allowed to proceed for 30 min at 37 °C, and excess SCN-DFO was removed by size exclusion spin column.

Cell binding (flow cytometry)

The apparent affinity of A11 cMb was determined by flow cytometry using 22Rv1-PSCA and 22Rv1 control cells, or PC3-PSCA and PC3 control cells. A11 cMb and A11 cMb-Cy5.5 were each incubated with 100,000 cells at concentrations varying from 0-1 µM (2 h on ice, triplicate). Samples were washed three times with PBS + 1% FBS + 0.02%

sodium azide. Goat anti-human IgG-Dylight 649 (Jackson ImmunoResearch Laboratory, Inc.) was the secondary antibody used to detect bound A11 cMb as previously described [14]. Samples were run on the BD-LSRFortessa X-20 analyzer and the results were analyzed using FlowJo (v9.3.2) to determine mean fluorescence intensity of the cells. GraphPad Prism 7.0a was used to fit the data using the one site saturation binding model.

Radiolabeling with ^{89}Zr and ^{124}I

^{89}Zr-oxalate (3D Imaging LLC) in 1 M oxalic acid was buffered in 2 M Na_2CO_3 (0.4× volume of ^{89}Zr) and 1 M HEPES pH 7.2-7.5 (2.5× volume of ^{89}Zr) [34]. In a typical reaction, ^{89}Zr-A11 cMb-Cy5.5 was prepared by incubating 100 µg of 1 mg/mL DFO-A11 cMb-Cy5.5 with 0.5 mCi (18.5 MBq) ^{89}Zr at pH 7 for 1 h at room temperature.

^{124}I-A11 cMb, and ^{124}I-A11 cMb-Cy5.5 were prepared using pre-coated Iodogen tubes according to the manufacturer's instructions (Pierce). In a typical reaction, 100 µg of 1 mg/mL A11 cMb or A11 cMb-Cy5.5 was incubated with 0.5 mCi (18.5 MBq) Na-^{124}I (3D Imaging LLC) in 0.1 M Tris, pH 8.0 for 10 min at room temperature.

Radiolabeled proteins were purified by size exclusion spin columns pre-equilibrated with 1% fetal bovine serum (FBS)/PBS. Radiolabeling efficiency and radiochemical purity were assessed by Instant Thin Layer Chromatography (ITLC strips for radiolabeled antibodies, Biodex Medical System) with 20 mM citrate pH 5.0 as the solvent for ^{89}Zr-labeled proteins and saline (0.9% sodium chloride) as the solvent for radioiodinated proteins. The strips were analyzed by gamma counting (Wizard 3" 1480 Automatic Gamma Counter, Perkin-Elmer).

The immunoreactive fraction was determined by the Lindmo method (1-50×10^6 cells) [35]. Radiolabeled A11 cMb (0.9-1.8 ng) was incubated with excess antigen using 22Rv1-PSCA (50×10^6 cells) or PC3-PSCA (50×10^6 cells) in 0.5 mL 1% FBS/PBS in triplicate for 1 h at room temperature. 22Rv1 or PC3 cells were used as a negative control. Cells were centrifuged and washed twice in 1% FBS/PBS, and the cell pellet and supernatant were assessed using a gamma counter.

MicroPET/CT imaging

Mice were administered Lugol's potassium iodide solution (Sigma-Aldrich) and potassium perchlorate (Sigma-Aldrich) to block nonspecific thyroid and stomach uptake, respectively [36, 37]. ^{124}I-A11 cMb (n=3, bilateral 22Rv1 and 22Rv1-PSCA s.c.), ^{124}I-A11 cMb-Cy5.5 (n=3, bilateral 22Rv1 and 22Rv1-PSCA s.c.; n=5, bilateral PC3 and PC3-PSCA s.c.), or ^{89}Zr A11 cMb-Cy5.5 (n=5, orthotopic 22R1-PSCA) (20-90 µCi, 0.74-3.33 MBq, 10-20 µg) in 0.1 mL saline was injected via tail vein. Immediately after injection or at 22 h p.i., mice were anesthetized with 1.5% isoflurane and 10-min static scans were acquired using an Inveon microPET scanner (Siemens), followed by 1-min microCT scans (CrumpCAT [38]). Following the final imaging time point, blood and organs were collected, weighed, and gamma-counted for *ex vivo* biodistribution. Uptake was calculated as % injected dose per gram of tissue (%ID/g) based on a standard containing 1% of the ID.

Dual PET/optical imaging

Following microPET/CT scans, post-mortem NIRF imaging was completed with the skin removed in the IVIS Lumina II (Perkin Elmer) using the following settings: emission = Cy5.5, excitation = 675 nm, 1 s exposure. The tumors and organs were excised and imaged *ex vivo* to compare relative fluorescence signals without obstruction by other organs.

Data analysis

MicroPET images were reconstructed by ordered subset expectation maximization-maximum a posteriori (OSEM-MAP, Inveon Acquisition Workplace). Images were analyzed and displayed using AMIDE [39]. MicroPET/CT overlays are displayed as maximum intensity projections (MIP) of the whole-body or 0.2 mm transverse slices. Fluorescence images were analyzed using the Living Image software (Perkin Elmer). Biodistribution graphs are depicted as scatter plots (with median and range) using GraphPad Prism (version 7.0a for Mac OS X, GraphPad Software). Statistical analysis was performed using multiple Student's *t*-tests, $P<0.05$, and p-values were corrected using the Holm-Šídák method. All values in the tables are reported as mean ± SD.

Results

Biochemical characterization of A11 cMb and conjugated derivatives

Purity and correct assembly of the A11 cMb (scFv-C_H3 dimer) and A11 cMb site-specifically conjugated with the near-infrared dye mal-Cy5.5 (**Figure 1**) was confirmed by SDS-PAGE analysis and size exclusion chromatography (SEC) (**Figure 2** and **Figure S1A-B**). A11 cMb and A11 cMb-Cy5.5 migrated as a single band approximately at the molecular weight calculated from the sequence (80.02 kDa) (**Figure S1A-B**). The size of the A11 cMb was estimated to be 70 kDa from interpolation of the SEC elution profile with known SEC standards (**Figure S1C**). A11 cMb-Cy5.5 and dual-labeled DFO-A11 cMb-Cy5.5 eluted as single peaks (27.07 min and 27.01 min, respectively) similar to the unconjugated A11

cMb, confirming that dimeric minibody conformation was not impaired (**Figure 2A**). Similar elution profiles of the absorbance at 280 nm (protein) and 675 nm (Cy5.5) demonstrated the fluorophore was associated with the protein (**Figure 2A**). A mean hydrodynamic diameter of 7.5 nm for A11 cMb was determined by dynamic light scattering (**Figure S1D**).

Mass spectrometry confirmed modification with Cy5.5 was specific to the C-terminal cysteine leaving the hinge unmodified (**Figure S1E**). Preliminary imaging studies (data not shown) with a higher D:P of 2:1 showed altered pharmacokinetics and biodistribution with higher uptake in the liver. Therefore, the optimized dye-to-protein (D:P) molar ratio of 0.6-0.8:1 was used to minimize impact on the biodistribution.

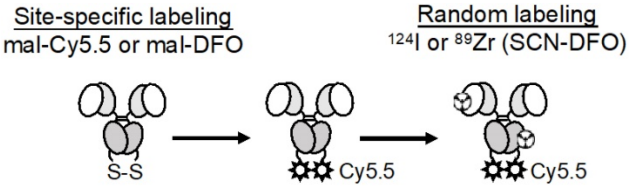

Figure 1. Schematic of the dual-labeled A11 cMb. Site-specific labeling to the A11 cMb C-terminal cysteines (reduced with TCEP) by maleimide-thiol chemistry. For radiolabeling, ^{124}I and SCN-DFO (chelates ^{89}Zr) are randomly labeled to surface-exposed tyrosine or lysine residues, respectively.

A11 cMb-Cy5.5 retains low nanomolar affinity binding to PSCA$^+$ cells

Flow cytometry analysis showed strong binding of A11 cMb-Cy5.5 to PSCA-expressing cells (22Rv1-PSCA). The selectivity for PSCA was confirmed using PSCA-negative cells (22Rv1) (**Figure 2B**). The apparent affinity (K_D value) calculated from saturation binding curves for A11 cMb-Cy5.5 (16.7 ± 3.4 nM, n=4, **Figure 2C**) was comparable to that of the parental A11 Mb (13.7 ± 1.4 nM, [15]). This was also similar to the apparent affinities of A11 cMb-Cy5.5 (22.7 ± 2.7 nM, n=7) and dual-labeled DFO-A11 cMb-Cy5.5 (26.8 ± 2.3 nM, n=3) to PC3-PSCA cells (data not shown) (P>0.05 for all).

ImmunoPET and fluorescence imaging of subcutaneous 22Rv1-PSCA tumors using single-labeled ^{124}I-A11 cMb and dual-labeled ^{124}I-A11 cMb-Cy5.5

^{124}I-A11 cMb and ^{124}I-A11 cMb-Cy5.5 had specific activities of 1.0-3.9 μCi/μg (37-144 kBq/μg) and 0.6-5.9 μCi/μg (22-219 kBq/μg), respectively, and both probes retained high immunoreactivity to PSCA-positive cells (>70%) (**Table 1**). For the 22Rv1-PSCA s.c. model, 20 μg of ^{124}I-A11 cMb or ^{124}I-A11 cMb-Cy5.5 with a final D:P of 0.7:1 was injected into nude mice. High-contrast immunoPET images acquired 22 h p.i. showed specific uptake of ^{124}I-A11 cMb or ^{124}I-A11 cMb-Cy5.5 in the 22Rv1-PSCA tumors compared to minimal uptake in the antigen-negative 22Rv1 tumors, blood, and background tissues (**Figure 3A-B**).

Specific uptake in the PSCA-positive tumors was confirmed by *ex vivo* biodistribution at 22 h p.i., with similar values for both ^{124}I-A11 cMb-Cy5.5 (12 ± 1.3 %ID/g) and ^{124}I-A11 cMb (12 ± 4.2 %ID/g, P>0.05) (**Figure 3C** and **Table 2**). Antigen-specific uptake in 22Rv1-PSCA tumors was significantly higher than nonspecific uptake in 22Rv1 tumors, resulting in positive-to-negative tumor ratios of 13:1 and 8:1, for ^{124}I-A11 cMb-Cy5.5 and ^{124}I-A11 cMb, respectively (**Table 2**). Importantly, no significant difference in uptake, clearance, and biodistribution between the single (^{124}I-A11 cMb) and the dual-modality (^{124}I-A11 cMb-Cy5.5) tracer was observed (**Figure 3C** and **Table 2**).

Table 1. Radiolabeling and immunoreactivity.

	^{124}I-A11 cMb	^{124}I-A11 cMb-Cy5.5	^{89}Zr-A11 cMb-Cy5.5
Radiolabeling Efficiency	81 ± 21% n=3	69 ± 23% n=6	99 ± 1% n=3
Radiochemical Purity	99.1 ± 0.6% n=3	99.1 ± 0.90% n=6	99.7 ± 0.1% n=2
Specific Activity	2.5 ± 1.5 μCi/μg n=3	3.3 ± 2.1 μCi/μg n=6	5.8 ± 0.7 μCi/μg n=3
Immunoreactive Fraction (r) for 22Rv1-PSCA	>0.76 n=3	>0.76 n=4	0.77 n=1
Immunoreactive Fraction (r) for PC3-PSCA	n/a	0.82 n=1	0.80 n=1

Values are reported as mean ± standard deviation (SD)

Table 2. Mice bearing 22Rv1-PSCA and 22Rv1 xenografts show similar *ex vivo* biodistribution of ^{124}I-A11 cMb or ^{124}I-A11 cMb-Cy5.5 at 22 h post-injection (P=n.s. for all tissues).

	^{124}I-A11 cMb %ID/g ± SD	^{124}I-A11 cMb-Cy5.5 %ID/g ± SD
22Rv1-PSCA	12 ± 4.2	12 ± 1.3
22Rv1	1.7 ± 1.0	1.2 ± 0.6
Blood	3.3 ± 0.1	1.9 ± 0.5
Heart	1.2 ± 0.1	0.7 ± 0.3
Lung	1.7 ± 0.1	1.2 ± 0.1
Liver	0.6 ± 0.0	0.9 ± 0.1
Kidney	1.1 ± 0.0	1.0 ± 0.1
Spleen	0.7 ± 0.1	0.5 ± 0.1
Stomach	2.1 ± 0.3	1.3 ± 0.0
Intestine	0.4 ± 0.0	0.2 ± 0.1
Muscle	0.2 ± 0.0	0.1 ± 0.0
Pos:Neg Tumor	8.1 ± 2.8	13 ± 7.7
Pos Tum:Blood	3.7 ± 1.2	6.6 ± 1.9
Neg Tum:Blood	0.5 ± 0.3	0.6 ± 0.2
Pos Tum:Muscle	54 ± 20 n=3	130 ± 39 n=3

%ID/g: % injected dose per gram; tum: tumor.
Values are reported as mean ± SD.

Post-mortem fluorescence imaging was completed with the skin removed in order to mimic an

intraoperative setting. In mice injected with ^{124}I-A11 cMb-Cy5.5, strong fluorescence signal was detected in the 22Rv1-PSCA tumors with minimal background signal in 22Rv1 tumors and surrounding muscle (**Figure 3D**). *Ex vivo* optical imaging of the resected tumors allowed comparison of relative fluorescence signals without obstruction by other organs. Consistent with the *in situ* results, high fluorescence signal was seen in the 22Rv1-PSCA tumors compared to 22Rv1 tumors (**Figure 3E**).

ImmunoPET and fluorescence imaging of subcutaneous PC3-PSCA tumors using ^{124}I-A11 cMb-Cy5.5

A subcutaneous PC3-PSCA tumor model was used to test the feasibility of imaging moderate levels of PSCA (5.2 ± 2.6×10^5 antigens/cell). MicroPET/CT of nude mice (n=5) bearing PC3-PSCA and control PC3 tumors showed high uptake of ^{124}I-A11 cMb-Cy5.5 in positive tumors at 22 h p.i. Nonspecific uptake in the stomach and thyroid is visible in images set at a scale of 0.2-2 %ID/g (**Figure 4A**), as these organs scavenge free iodine and were likely incompletely blocked. The *ex vivo* biodistribution confirms the imaging results with significantly higher uptake in PC3-PSCA tumors (2.9 ± 0.6 %ID/g) compared to PC3 tumors (0.7 ± 0.4 %ID/g) (P=0.0002), resulting in a positive-to-negative tumor ratio of 5.6:1, and PC3-PSCA tumor-to-muscle ratio of 54:1 (**Figure 4B** and **Table 3**).

Ex vivo optical imaging allowed comparison between the PC3-PSCA tumors, which were detected by Cy5.5 fluorescence, and PC3 control tumors, which had little to no fluorescence signal (**Figure 4C**). *Ex vivo* analysis showed expected autofluorescence (stomach, intestines) and additional signal in liver, kidneys, and bladder due to tracer clearance (**Figure S2**).

ImmunoPET and fluorescence imaging of intraprostatic 22Rv1-PSCA tumors using ^{89}Zr-A11 cMb-Cy5.5

In order to test dual-imaging at the natural site of prostate disease, an orthotopic model was assessed. These studies were conducted using ^{89}Zr because signal from ^{124}I clearance to the bladder interfered with visualization of activity accumulated in the prostate (data not shown). Mice were intraprostatically implanted with 22Rv1-PSCA-Fluc-GFP cells, and tumors grew extensively with significant bioluminescence signal (n=4) or low signal (n=1), which was designated "limited disease" (**Figure S3**).

^{89}Zr-A11 cMb-Cy5.5 immunoPET at 22 h p.i. showed specific uptake in the prostate tumors with extensive disease compared to minimal prostate signal in the mouse with limited disease (**Figure 5A**). *Ex vivo* biodistribution at (22 h p.i.) confirmed specific uptake in the 22Rv1-PSCA tumors (3.1 ± 0.5 %ID/g), and the tumor-to-blood ratio was quantified to be 3:1. Due to the residualizing nature of the radiometal, activity in organs of clearance was retained at high levels compared with the iodinated A11 cMb (liver: 18 ± 2.7 %ID/g, kidneys: 12 ± 1.2 %ID/g, spleen: 5.1 ± 2.1 %ID/g) (**Figure 5A-B** and **Table 4**). Nonspecific uptake in the bone is due to accumulation of free ^{89}Zr. Importantly, the prostate tumor was clearly distinguished by post-mortem fluorescence imaging compared to adjacent seminal vesicles and bladder, which supports the feasibility of fluorescence guidance for prostate cancer surgery (**Figure 5C**). PSCA-positive tumor growth in the prostate and absence of neoplastic tissue in the surrounding seminal vesicles was confirmed by H&E and anti-PSCA immunohistochemistry (IHC) (**Figure 5D**).

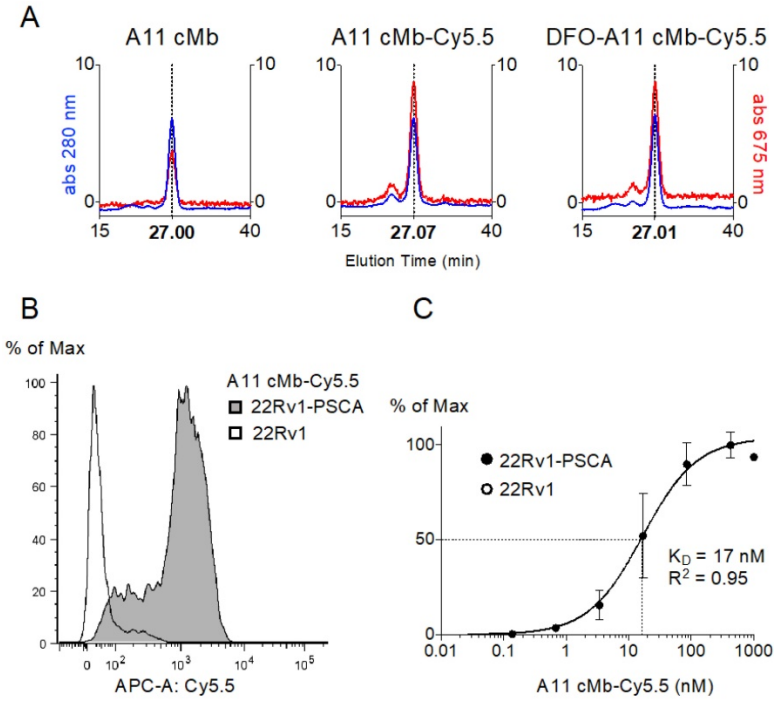

Figure 2. Biochemical characterization of A11 cMb-Cy5.5. (A) Size exclusion chromatography (SEC) elution profiles show A11 cMb, A11 cMb-Cy5.5, and DFO-A11 cMb-Cy5.5 elute in a single peak (27.00 min, 27.07 min, and 27.01 min, respectively), demonstrating the conjugations did not disrupt the minibody dimeric conformation (protein at 280 nm, Cy5.5 at 675 nm). Absorption at 675 nm (Cy5.5) is higher for the conjugated A11 cMb samples. **(B)** Flow cytometry analysis shows A11 cMb-Cy5.5 binding specifically to 22Rv1-PSCA cells. No binding to control 22Rv1 cells was detected. **(C)** Saturation binding study of A11 cMb-Cy5.5 (22Rv1-PSCA and 22Rv1 cells) was used to calculate the half-maximal binding K_D using a one-site specific binding model (n=3, GraphPad).

Table 3. *Ex vivo* biodistribution of ^{124}I-A11 cMb-Cy5.5 in mice bearing PC3-PSCA and PC3 xenografts at 22 h post-injection.

	^{124}I-A11 cMb-Cy5.5
	%ID/g ± SD
PC3-PSCA	2.9 ± 0.6
PC3	0.7 ± 0.4
Blood	1.2 ± 0.2
Heart	0.4 ± 0.2
Lung	0.6 ± 0.3
Liver	0.4 ± 0.1
Kidney	0.5 ± 0.1
Spleen	0.4 ± 0.2
Stomach	3.1 ± 0.6
Intestine	0.2 ± 0.1
Bone	0.2 ± 0.1
Muscle	0.1 ± 0.0
Pros, s.v., b	0.8 ± 0.3
Testes	0.3 ± 0.1
Pos:Neg Tumor	5.6 ± 2.9
Pos Tum:Blood	2.6 ± 0.8
Neg Tum:Blood	0.6 ± 0.3
Pos Tum:Muscle	54 ± 21
	n=5

%ID/g: % injected dose per gram; b: bladder; pros: prostate; s.v.: seminal vesicles; tum: tumor.
Values are reported as mean ± SD.

Table 4. *Ex vivo* biodistribution of ^{89}Zr-A11 cMb-Cy5.5 in mice bearing intraprostatic 22Rv1-PSCA tumors at 22 h post-injection.

	^{89}Zr-A11 cMb-Cy5.5
	%ID/g ± SD
Prostate Tumor	3.1 ± 0.5
Blood	0.9 ± 0.1
Heart	2.6 ± 0.7
Lung	2.4 ± 1.6
Liver	18 ± 2.7
Kidney	12 ± 1.2
Spleen	5.1 ± 2.1
Stomach	1.1 ± 0.2
Intestine	2.6 ± 0.3
Bone	4.4 ± 2.3
Muscle	0.4 ± 0.1
Testes	2.9 ± 1.4
Pros Tum:Blood	3.4 ± 0.2
Pros Tum:Muscle	7.7 ± 1.0
	n=4, except blood n=3

%ID/g: % injected dose per gram; pros: prostate; tum: tumor.
Values are reported as mean ± SD.

Discussion

Primary prostate cancer and regional lymph node metastases can be treated by surgical resection. However, patients often suffer from over and under-treatment due to inaccurate diagnosis or inability to visualize positive margins during surgery. Dual-modality PET/fluorescence imaging could provide non-invasive whole-body disease detection and intraoperative fluorescence guidance, and therefore improve prostate cancer treatment.

In this study, the anti-PSCA antibody fragment A11 cys-minibody (A11 cMb) was used to generate a novel dual-modality imaging probe. A11 cMb was conjugated with the near-infrared dye Cy5.5 and radiolabeled with either ^{124}I or ^{89}Zr (^{124}I-A11 cMb-Cy5.5 and ^{89}Zr-A11 cMb-Cy5.5). Both tracers showed specific targeting to PSCA-expressing prostate cancer *in vivo* resulting in whole body immunoPET scans visualizing the tumors and fluorescence imaging distinguishing PSCA-positive cancer from surrounding healthy tissue.

Fluorescent modification of A11 cMb did not impair its affinity or specificity of antigen binding. Studies have shown that binding affinity can be affected by conjugation of large hydrophobic moieties, such as near-infrared dyes [40]. Therefore, the Cy5.5 conjugation was directed to the engineered C-terminal cysteine away from the antigen binding sites. A11 cMb-Cy5.5 and DFO-A11 cMb-Cy5.5 specifically bound to PSCA-positive cells with high affinity, similar to previously published unconjugated parental A11 Mb [14] (**Figure 2**). Dual-labeled ^{124}I-A11 cMb-Cy5.5 and ^{89}Zr-A11 cMb-Cy5.5 retained high immunoreactivity for PSCA-positive cells similar to ^{124}I-A11 cMb (**Table 1**), demonstrating that dual-labeling did not impair binding. Fluorophore conjugation can also affect the pharmacokinetics and biodistribution of antibodies and small ligands [20, 28], typically in the form of enhanced liver uptake and faster blood clearance. ^{124}I-A11 cMb-Cy5.5 with a dye-to-protein ratio (D:P) of 0.7-0.8:1 demonstrated similar tumor uptake and minimal changes in biodistribution compared with ^{124}I-A11 cMb.

Fluorescence imaging-guided surgery has been shown to improve tumor resection in preclinical studies and several agents have entered clinical trials [41]. Furthermore, dual-modality imaging is increasingly studied in both preclinical and clinical studies [26, 31, 32]. Imaging with a dual-labeled antibody ensures similar biodistribution in both modalities and facilitates clinical translation by avoiding separate testing of distinct imaging tracers. While immunoPET provides whole-body, quantitative information with unlimited depth, it suffers from low resolution and time constraints due to radioactive decay. NIRF fluorophores, on the other hand, show low depth of penetration [42] but excellent cell-level resolution. Unlike the radiolabel, the fluorophore does not have a physical half-life (cellular half-life = 3.9 days [43]) and therefore allows longer detection of the signal for surgical guidance.

PSCA is expressed in virtually all prostate cancers (83-100%) as well as in prostate cancer metastases to bone and lymph nodes [11, 13, 44, 45]. However, a wide range of PSCA expression levels, correlating with progression and prognosis, was found by quantitative reverse transcriptase-PCR analysis of clinical prostate metastases specimens [44].

Because increased PSCA corresponds with increased Gleason score and clinical stage, we therefore evaluated the dual-modality A11 cMb in two s.c. models with different levels of PSCA expression: 22Rv1-PSCA (high-PSCA) and PC3-PSCA (moderate PSCA). Importantly, ^{124}I-A11 cMb-Cy5.5 immuno-PET/fluorescence imaging resulted in high-contrast PET and fluorescence images in both high- and moderate PSCA-positive prostate cancer models. Although antigen expression does not necessarily correlate with tumor uptake, as other factors such as tumor vasculature can affect accessibility, the dual-modality A11 cMb could facilitate detection in different stages of prostate cancer.

The longer-lived radionuclides ^{124}I and ^{89}Zr are most commonly used for labeling antibodies, and in this study, we compared specific tumor uptake and contrast to normal tissue of both ^{124}I- and ^{89}Zr-labeled A11 cMb-Cy5.5 in preclinical prostate cancer models. ^{124}I and ^{89}Zr differ regarding their physical properties, protein conjugation chemistry, and biological metabolism, which can lead to significant differences in uptake and retention of the radioactive signal. ^{124}I is a nonresidualizing radiolabel when radioiodinated using standard methods such as Iodogen. Upon internalization and degradation of such radioiodinated proteins, metabolites including iodotyrosine are not retained by the cell, leading to low background and thereby high contrast. These characteristics are advantageous when imaging targets retained on the cell surface, like PSCA that has previously been shown to internalize slowly [14]. Concordantly, immunoPET studies using ^{124}I-labeled parental A11 Mb [14], ^{124}I-A11 cMb and ^{124}I-A11 cMb-Cy5.5 achieved high-contrast images in the subcutaneous models (22Rv1-PSCA, PC3-PSCA). A previous study using ^{124}I-A11 Mb to image intratibial xenografts supports the hypothesis that the very low background of ^{124}I-A11 cMb-Cy5.5 will be advantageous for targeting bone metastases [15]. In contrast, free ^{89}Zr accumulates in bone and may result in false positives [46].

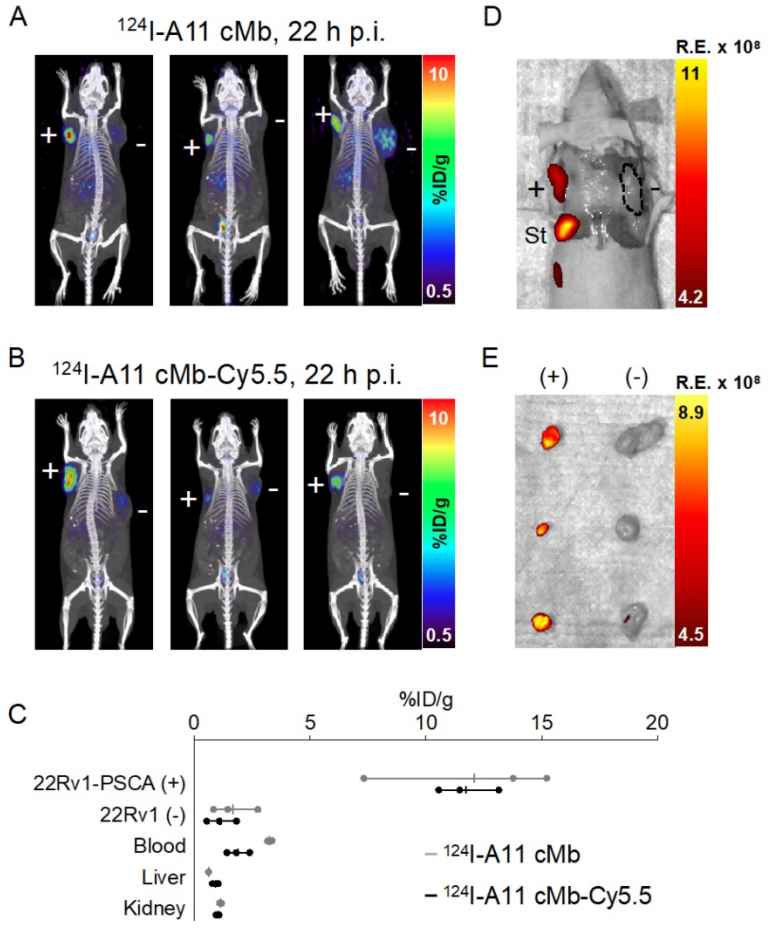

Figure 3. ^{124}I-A11 cMb-Cy5.5 PET/fluorescence shows specific targeting to 22Rv1-PSCA subcutaneous tumors. (A) ^{124}I-A11 cMb and **(B)** ^{124}I-A11 cMb-Cy5.5 PET/CT scans show antigen-specific uptake in 22Rv1-PSCA tumors (+, left shoulder) and minimal nonspecific uptake in 22Rv1 (-, right shoulder) tumors at 22 h post-injection (nude mice, n=3 per group). Images are represented as whole-body maximum intensity projections (MIPs). **(C)** *Ex vivo* biodistribution (22 hours p.i.) confirms high uptake in 22Rv1-PSCA tumors and low activity in all other tissues. The addition of Cy5.5 at a low dye-to-protein ratio did not alter biodistribution. **(D-E)** Post-mortem Cy5.5 fluorescence images show specific signal in PSCA-positive tumors. The signal from the stomach is due to autofluorescence. R.E.: radiance efficiency ($\frac{photons/sec/cm^2/sr}{\mu w/cm^2}$); St: stomach.

A major benefit of imaging with a residualizing radiometal (^{89}Zr) is better signal retention, as ^{89}Zr-radiometabolites get trapped in the cell upon internalization, and higher spatial resolution due to a shorter mean positron range (1.1 mm for ^{89}Zr vs 3.0 mm for ^{124}I). These factors are crucial when imaging small structures like the prostate; hence, ^{89}Zr-A11 cMb-Cy5.5 was used to image orthotopic prostate cancer. A further advantage compared with ^{124}I is that ^{89}Zr is not excreted through urine, assuring minimal interference from activity in the bladder.

^{89}Zr-A11 cMb-Cy5.5 immunoPET/fluorescence imaging of the orthotopic model demonstrated successful visualization and delineation of 22Rv1-PSCA tumors growing at the site of natural disease, which is an important finding as tumor localization and accessibility are known to affect tumor targeting and tracer uptake, and may account for the difference in tumor uptake between the orthotopic and s.c. models. These promising results and the fact that the dual-modality tracer is based on a humanized antibody fragment suggest that ^{89}Zr- and ^{124}I-labeled A11 cMb-Cy5.5 could be clinically translated for imaging

and surgical guidance in prostate cancer. The results from an ongoing Phase I trial evaluating ^{124}I-parental A11 Mb for immunoPET (NCT02092948) will inform on the pharmacokinetics of radiolabeled minibody in patients.

Future studies should include surgical studies to mimic the clinical setting (radical prostatectomy) and confirm a survival benefit of resecting tumors guided by real-time fluorescence imaging. Furthermore, more clinically relevant metastatic prostate cancer models should be imaged to ensure that positive pelvic lymph nodes are detectable both preoperatively using ^{89}Zr-A11 cMb-Cy5.5 immunoPET and intraoperatively using fluorescence, as the current clinical standard using frozen section histology to confirm which lymph nodes to resect is time-intensive [47].

Dual-modality imaging can also be applied to antibodies against other prostate cancer targets. For example, GRPR has been successfully targeted by ^{68}Ga-HZ220-IRDye 650 in mice bearing PC3 xenografts for PET/NIRF imaging [29], as well as by ^{68}Ga-IRDye800CW-BBN in a first-in-human study in patients with glioblastoma [48]. Antibodies and peptides targeting PSMA have been extensively explored for PET [49], and more recently validated for optical imaging [20] and dual SPECT/fluorescence imaging [26-28]. Dual-labeled ^{111}In-PSMA-targeting-urea-IRDye800CW [27] and ^{111}In-anti-PSMA antibody D2B-IRDye800CW [28] successfully detected prostate cancer lesions in mice by SPECT/NIRF, and the anti-PSMA antibody MDX1201-A488 is currently being evaluated for FIGS in patients receiving robot-assisted laparoscopic prostatectomy (NCT02048150). However, PSMA is also expressed in normal tissues, such as the ganglia close to the location of typical lymph node metastases, which could result in false positives, and PSMA overexpression is not present in 10% of patients [50]. Therefore, it would be useful to also explore PSCA as an additional target for prostate cancer diagnosis and therapy.

In summary, specific targeting to human PSCA -positive prostate cancer was achieved by *in vivo* administration of ^{124}I-A11 cMb-Cy5.5 and ^{89}Zr-A11 cMb-Cy5.5 for immunoPET and fluorescence imaging. Dual-modality imaging was successful in s.c. models with high and moderate PSCA expression, demonstrating the ability of the A11 cMb to target a range of antigen expression. In the intraprostatic model, fluorescence clearly distinguished the prostate tumor from surrounding relevant tissues. This work has translational potential for noninvasive preoperative whole-body imaging and additional real-time intraoperative guidance in PSCA-positive prostate cancer.

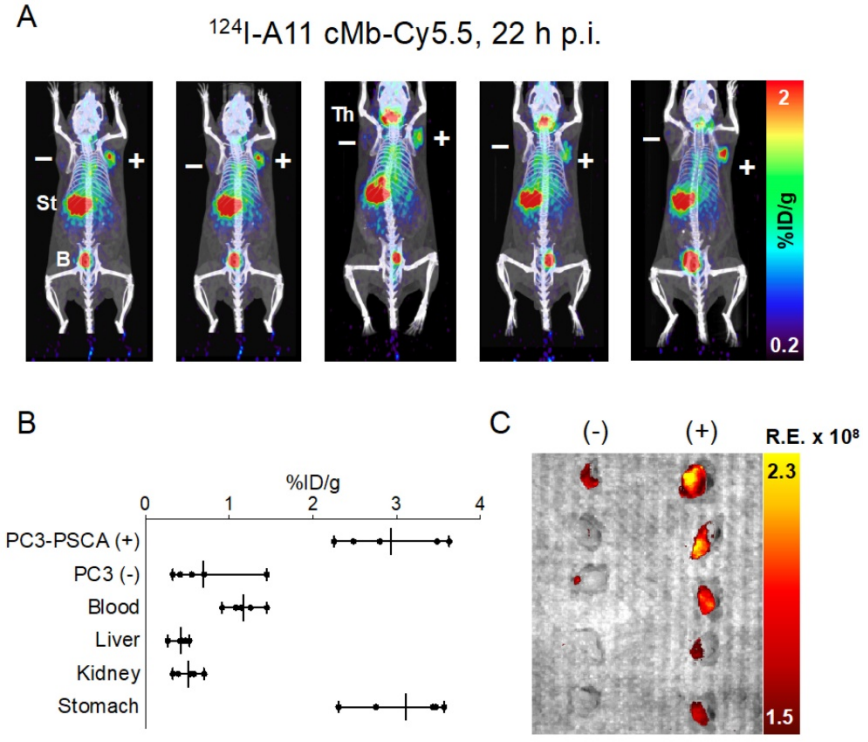

Figure 4. ^{124}I-A11 cMb-Cy5.5 PET/fluorescence shows specific targeting of PC3-PSCA subcutaneous tumors. (A) ^{124}I-A11 cMb-Cy5.5 PET/CT scans at 22 h post-injection (nude mice, n=5) show specific uptake in subcutaneous PC3-PSCA (+, right shoulder) tumors and no nonspecific uptake in PC3 tumors (PSCA-, left shoulder). Images are represented as whole-body MIPs. **(B)** *Ex vivo* biodistribution (22 h p.i.) confirms higher %ID/g uptake in PC3-PSCA tumors than PC3 tumors. **(C)** *Ex vivo* fluorescence (Cy5.5) imaging revealed strong fluorescence signal in PC3-PSCA tumors and excellent contrast to PC3 control tumors. B: bladder; R.E.: radiance efficiency ($\frac{\text{photons/sec/cm}^2\text{/sr}}{\mu\text{w/cm}^2}$); St: stomach; Th: thyroid.

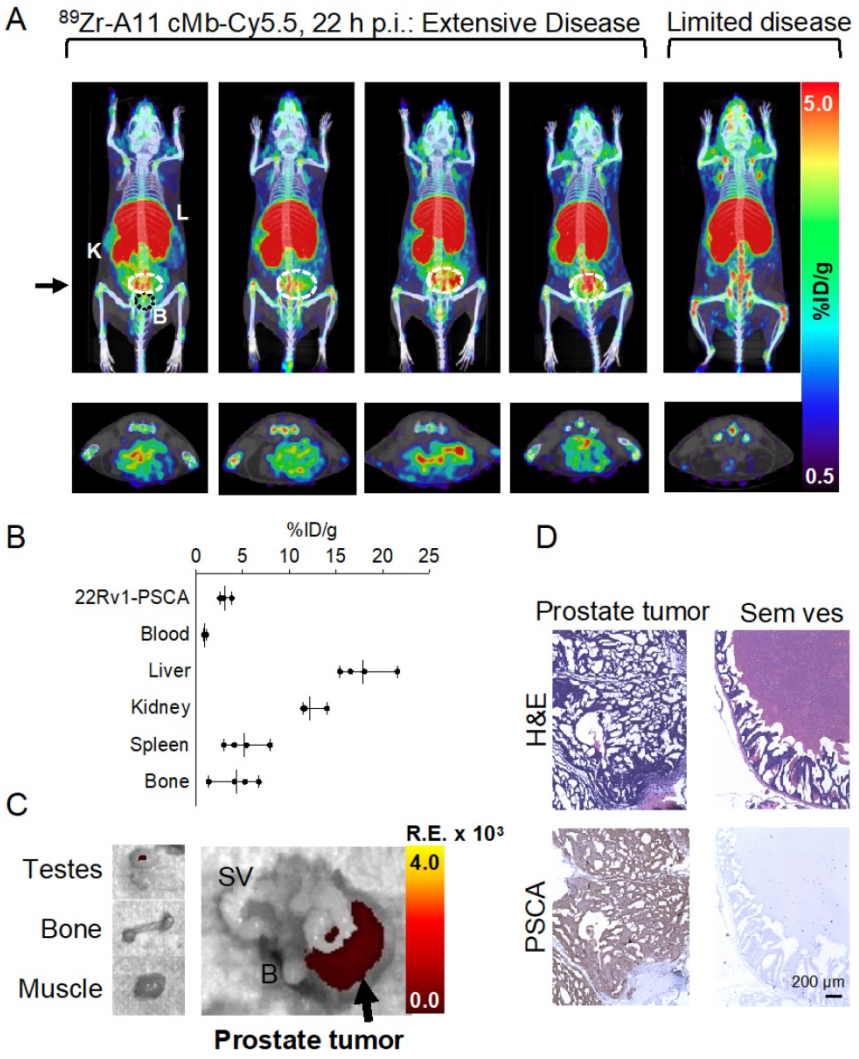

Figure 5. ^{89}Zr-A11 cMb-Cy5.5 targets 22Rv1-PSCA intraprostatic tumors by PET/fluorescence. (A) ^{89}Zr-A11 cMb-Cy5.5 PET/CT at 22 h post-injection of nude mice (n=4) bearing 22Rv1-PSCA-GFP-FLuc intraprostatic orthotopic tumors (outlined by the white dotted circle), compared to a mouse (n=1) with limited disease. The top row images are represented as coronal whole-body MIPs, and the bottom row images are represented as 0.2 mm transverse sections that correspond to the black arrow. The transverse section does not include the bladder (outlined in the left top panel by the black dotted circle). **(B)** *Ex vivo* biodistribution (22 h p.i.) confirms higher %ID/g uptake in 22Rv1-PSCA prostate tumors compared to blood, along with high clearance to the liver and kidney. **(C)** Cy5.5 fluorescence signal is specific to the resected prostate with little to no signal in surrounding seminal vesicles, bladder, or background tissues (testes, bone, and muscle). R.E.: radiance efficiency ($\frac{\text{photons/sec/cm}^2\text{/sr}}{\mu\text{w/cm}^2}$). **(D)** Hematoxylin and eosin (H&E) staining confirms tumor growth in the prostate, which stained positively for PSCA, while surrounding seminal vesicles were negative for PSCA. B: bladder; K: kidney; L: liver; SV: seminal vesicle.

Abbreviations

cMb: cys-minibody; FIGS: fluorescence imaging-guided surgery; IHC: immunohistochemistry; Mb: minibody; MRI: magnetic resonance imaging; NIRF: near-infrared fluorescence; PET: positron emission tomography; PSCA: prostate stem cell antigen; PSMA: prostate specific membrane antigen; SEC: size exclusion chromatography; SPECT: single-photon emission computed tomography.

Supplementary Material

Supplementary figures.
http://www.thno.org/v08p5903s1.pdf

Acknowledgements

The authors thank Felix B Salazar, Amanda C Freise, Kelly Huynh, and Chong Hyun Chang for technical assistance. We thank Waldemar Ladno, Theresa Falls, Olga Sergeeva, Jason Lee, and Arion Chatziioannou from the UCLA Crump Institute Preclinical Imaging Technology Center for assistance with small-animal PET and fluorescence imaging. We thank Roger Moore from City of Hope for completion of mass spectrometry studies, Jeff Calimlim from the Jonsson Comprehensive Cancer Center Flow Cytometry Core for assistance with flow cytometry, and the UCLA Translational Pathology Core Laboratory for histology assistance.

Grant Support

This work was supported by NIH grants R01 CA174294, P30 CA016042, Department of Defense W81 XWH-15-1-0725, and the Dr. Ursula Mandel fellowship. Imaging, flow cytometry, pathology core services were supported by Jonsson Comprehensive Cancer Center (P30 CA016042).

Competing Interests

A. Wu has an ownership interest in, and is a board member and consultant for ImaginAb, Inc.

References

1. Hricak H, Choyke PL, Eberhardt SC, Leibel SA, Scardino PT. Imaging prostate cancer: a multidisciplinary perspective. Radiology. 2007; 243: 28-53.
2. Wibmer AG, Burger IA, Sala E, Hricak H, Weber WA, Vargas HA. Molecular imaging of prostate cancer. Radiographics. 2016; 36: 142-59.
3. Epstein JI, Amin M, Boccon-Gibod L, Egevad L, Humphrey PA, Mikuz G, et al. Prognostic factors and reporting of prostate carcinoma in radical prostatectomy and pelvic lymphadenectomy specimens. Scand J Urol Nephrol Suppl. 2005; 243: 34-63.
4. Yossepowitch O, Briganti A, Eastham JA, Epstein J, Graefen M, Montironi R, et al. Positive surgical margins after radical prostatectomy: a systematic review and contemporary update. Eur Urol. 2014; 65: 303-13.
5. Walsh PC, Marschke P, Ricker D, Burnett AL. Patient-reported urinary continence and sexual function after anatomic radical prostatectomy. Urology. 2000; 55: 58-61.
6. Ficarra V, Novara G, Ahlering TE, Costello A, Eastham JA, Graefen M, et al. Systematic review and meta-analysis of studies reporting potency rates after robot-assisted radical prostatectomy. Eur Urol. 2012; 62: 418-30.
7. Jadvar H. Molecular imaging of prostate cancer with PET. J Nucl Med. 2013; 54: 1685-8.
8. Pandit-Taskar N, O'Donoghue JA, Ruan S, Lyashchenko S, Carrasquillo JA, Heller G, et al. First-in-human imaging with 89Zr-Df-IAB2M anti-PSMA minibody in patients with metastatic prostate cancer: pharmacokinetics, biodistribution, dosimetry, and lesion uptake. J Nucl Med. 2016; 57:1858-1864.
9. Lutje S, Slavik R, Fendler W, Herrmann K, Eiber M. PSMA ligands in prostate cancer - probe optimization and theranostic applications. Methods. 2017; 130: 42-50.
10. Wieser G, Mansi R, Grosu AL, Schultze-Seemann W, Dumont-Walter RA, Meyer PT, et al. Positron emission tomography (PET) imaging of prostate cancer with a gastrin releasing peptide receptor antagonist—from mice to men. Theranostics. 2014; 4: 412-9.
11. Reiter RE, Gu Z, Watabe T, Thomas G, Szigeti K, Davis E, et al. Prostate stem cell antigen: a cell surface marker overexpressed in prostate cancer. Proc Natl Acad Sci U S A. 1998; 95: 1735-40.
12. Han KR, Seligson DB, Liu X, Horvath S, Shintaku PI, Thomas GV, et al. Prostate stem cell antigen expression is associated with gleason score, seminal vesicle invasion and capsular invasion in prostate cancer. J Urol. 2004; 171: 1117-21.
13. Gu Z, Thomas G, Yamashiro J, Shintaku IP, Dorey F, Raitano A, et al. Prostate stem cell antigen (PSCA) expression increases with high gleason score, advanced stage and bone metastasis in prostate cancer. Oncogene. 2000; 19: 1288-96.
14. Knowles SM, Zettlitz KA, Tavare R, Rochefort MM, Salazar FB, Stout DB, et al. Quantitative immunoPET of prostate cancer xenografts with 89Zr- and 124I-labeled anti-PSCA A11 minibody. J Nucl Med. 2014; 55: 452-9.
15. Knowles SM, Tavare R, Zettlitz KA, Rochefort MM, Salazar FB, Jiang ZK, et al. Applications of immunoPET: using 124I-anti-PSCA A11 minibody for imaging disease progression and response to therapy in mouse xenograft models of prostate cancer. Clin Cancer Res. 2014; 20: 6367-78.
16. Wu H, Shi H, Zhang H, Wang X, Yang Y, Yu C, et al. Prostate stem cell antigen antibody-conjugated multiwalled carbon nanotubes for targeted ultrasound imaging and drug delivery. Biomaterials. 2014; 35: 5369-80.
17. Foss CA, Fox JJ, Feldmann G, Maitra A, Iacobuzio-Donohue C, Kern SE, et al. Radiolabeled anti-claudin 4 and anti-prostate stem cell antigen: initial imaging in experimental models of pancreatic cancer. Mol Imaging. 2007; 6: 131-9.
18. Knowles SM, Wu AM. Advances in immuno-positron emission tomography: antibodies for molecular imaging in oncology. J Clin Oncol. 2012; 30: 3884-92.
19. Vahrmeijer AL, Hutteman M, van der Vorst JR, van de Velde CJ, Frangioni JV. Image-guided cancer surgery using near-infrared fluorescence. Nat Rev Clin Oncol. 2013; 10: 507-18.
20. Zhang RR, Schroeder AB, Grudzinski JJ, Rosenthal EL, Warram JM, Pinchuk AN, et al. Beyond the margins: real-time detection of cancer using targeted fluorophores. Nat Rev Clin Oncol. 2017; 14: 347-364.
21. Hong G, Antaris AL, Dai H. Near-infrared fluorophores for biomedical imaging. Nat Biomed Eng. 2017; 1:0010.
22. Nguyen QT, Tsien RY. Fluorescence-guided surgery with live molecular navigation--a new cutting edge. Nat Rev Cancer. 2013; 13: 653-62.
23. Nakajima T, Mitsunaga M, Bander NH, Heston WD, Choyke PL, Kobayashi H. Targeted, activatable, in vivo fluorescence imaging of prostate-specific membrane antigen (PSMA) positive tumors using the quenched humanized J591 antibody-indocyanine green (ICG) conjugate. Bioconjugate Chem. 2011; 22: 1700-5.
24. Watanabe R, Hanaoka H, Sato K, Nagaya T, Harada T, Mitsunaga M, et al. Photoimmunotherapy targeting prostate-specific membrane antigen: are antibody fragments as effective as antibodies? J Nucl Med. 2015; 56: 140-4.
25. Sonn GA, Behesnilian AS, Jiang ZK, Zettlitz KA, Lepin EJ, Bentolila LA, et al. Fluorescent image-guided surgery with an anti-prostate stem cell antigen (PSCA) diabody enables targeted resection of mouse prostate cancer xenografts in real time. Clin Cancer Res. 2016; 22: 1403-12.
26. Lutje S, Rijpkema M, Helfrich W, Oyen WJ, Boerman OC. Targeted radionuclide and fluorescence dual-modality imaging of cancer: preclinical advances and clinical translation. Mol Imaging Biol. 2014; 16: 747-55.
27. Banerjee SR, Pullambhatla M, Byun Y, Nimmagadda S, Foss CA, Green G, et al. Sequential SPECT and optical imaging of experimental models of prostate cancer with a dual modality inhibitor of the prostate-specific membrane antigen. Angew Chem Int Ed Engl. 2011; 50: 9167-70.
28. Lutje S, Rijpkema M, Franssen GM, Fracasso G, Helfrich W, Eek A, et al. Dual-Modality image-guided surgery of prostate cancer with a radiolabeled fluorescent anti-PSMA monoclonal antibody. J Nucl Med. 2014; 55: 995-1001.
29. Zhang H, Desai P, Koike Y, Houghton J, Carlin SD, Tandon N, et al. Dual modality imaging of prostate cancer with a fluorescent and radiogallium-labeled GRP receptor antagonist. J Nucl Med. 2016; 58: 29-35.
30. Hekman MC, Rijpkema M, Bos D, Oosterwijk E, Goldenberg DM, Mulders PF, et al. Detection of micrometastases using SPECT/fluorescence dual-modality imaging in a CEA-expressing tumor model. J Nucl Med. 2017; 58: 706-710.
31. Hekman MC, Rijpkema M, Muselaers CH, Oosterwijk E, Hulsbergen-Van de Kaa CA, Boerman OC, et al. Tumor-targeted dual-modality imaging to improve intraoperative visualization of clear cell renal cell carcinoma: a first in man study. Theranostics. 2018; 8: 2161-70.
32. Zettlitz KA, Tsai WK, Knowles SM, Kobayashi N, Donahue TR, Reiter RE, et al. Dual-modality immunoPET and near-infrared fluorescence (NIRF) imaging of pancreatic cancer using an anti-prostate cancer stem cell antigen (PSCA) cys-diabody. J Nucl Med. 2018; 59: 1398-1405.
33. Saffran DC, Raitano AB, Hubert RS, Witte ON, Reiter RE, Jakobovits A. Anti-PSCA mAbs inhibit tumor growth and metastasis formation and prolong the survival of mice bearing human prostate cancer xenografts. Proc Natl Acad Sci U S A. 2001; 98: 2658-63.
34. Vosjan MJ, Perk LR, Visser GW, Budde M, Jurek P, Kiefer GE, et al. Conjugation and radiolabeling of monoclonal antibodies with zirconium-89 for PET imaging using the bifunctional chelate p-isothiocyanatobenzyl-desferrioxamine. Nat Protoc. 2010; 5: 739-43.
35. Lindmo T, Boven E, Cuttitta F, Fedorko J, Bunn PA, Jr. Determination of the immunoreactive fraction of radiolabeled monoclonal antibodies by linear extrapolation to binding at infinite antigen excess. J Immunol Methods. 1984; 72: 77-89.
36. Robinson MK, Doss M, Shaller C, Narayanan D, Marks JD, Adler LP, et al. Quantitative immuno-positron emission tomography imaging of HER2-positive tumor xenografts with an iodine-124 labeled anti-HER2 diabody. Cancer Res. 2005; 65: 1471-8.
37. Sundaresan G, Yazaki PJ, Shively JE, Finn RD, Larson SM, Raubitschek AA, et al. 124I-labeled engineered anti-CEA minibodies and diabodies allow high-contrast, antigen-specific small-animal PET imaging of xenografts in athymic mice. J Nucl Med. 2003; 44: 1962-9.
38. Taschereau R, Vu NT, Chatziioannou AF. Calibration and data standardization of a prototype bench-top preclinical CT. IEEE Nuclear Science Symposium and Medical Imaging Conference. Seattle, WA, USA. Nov 8-15, 2014.
39. Loening AM, Gambhir SS. AMIDE: a free software tool for multimodality medical image analysis. Mol Imaging. 2003; 2: 131-7.
40. Cilliers C, Nessler I, Christodolu N, Thurber GM. Tracking antibody distribution with near-infrared fluorescent dyes: impact of dye structure and degree of labeling on plasma clearance. Mol Pharm. 2017; 17: 757-62.
41. Zhang RR, Schroeder AB, Grudzinski JJ, Rosenthal EL, Warram JM, Pinchuk AN, et al. Beyond the margins: real-time detection of cancer using targeted fluorophores. Nat Rev Clin Oncol. 2017; 14: 347-64.
42. Chi C, Du Y, Ye J, Kou D, Qiu J, Wang J, et al. Intraoperative imaging-guided cancer surgery: from current fluorescence molecular imaging methods to future multi-modality imaging technology. Theranostics. 2014; 4: 1072-84.
43. Cilliers C, Liao J, Atangcho L, Thurber GM. Residualization rates of near-infrared dyes for the rational design of molecular imaging agents. Mol Imaging Biol. 2015; 17: 757-62.
44. Lam JS, Yamashiro J, Shintaku IP, Vessella RL, Jenkins RB, Horvath S, et al. Prostate stem cell antigen is overexpressed in prostate cancer metastases. Clin Cancer Res. 2005; 11: 2591-6.
45. Zhigang Z, Wenlv S. Prostate stem cell antigen (PSCA) expression in human prostate cancer tissues and its potential role in prostate carcinogenesis and progression of prostate cancer. World J Surg Oncol. 2004; 2: 13.
46. Deri MA, Zeglis BM, Francesconi LC, Lewis JS. PET imaging with 89Zr: from radiochemistry to the clinic. Nucl Med Biol. 2013; 40: 3-14.

47. Daneshmand S, Quek ML, Stein JP, Lieskovsky G, Cai J, Pinski J, et al. Prognosis of patients with lymph node positive prostate cancer following radical prostatectomy: long-term results. J Urol. 2004; 172: 2252-5.
48. Li D, Zhang J, Chi C, Xiao X, Wang J, Lang L, et al. First-in-human study of PET and optical dual-modality image-guided surgery in glioblastoma using (68)Ga-IRDye800CW-BBN. Theranostics. 2018; 8: 2508-2520.
49. Lutje S, Heskamp S, Cornelissen AS, Poeppel TD, van den Broek SA, Rosenbaum-Krumme S, et al. PSMA ligands for radionuclide imaging and therapy of prostate cancer: clinical status. Theranostics. 2015; 5: 1388-401.
50. Schwarzenboeck SM, Rauscher I, Bluemel C, Fendler WP, Rowe SP, Pomper MG, et al. PSMA ligands for pet imaging of prostate cancer. J Nucl Med. 2017; 58: 1545-52.

Published OnlineFirst October 9, 2018; DOI: 10.1158/1078-0432.CCR-18-1382

Precision Medicine and Imaging

Clinical Cancer Research

Near-Infrared Dye-Labeled Anti-Prostate Stem Cell Antigen Minibody Enables Real-Time Fluorescence Imaging and Targeted Surgery in Translational Mouse Models

Mo Zhang[1,2], Naoko Kobayashi[1], Kirstin A. Zettlitz[3], Evelyn A. Kono[1], Joyce M. Yamashiro[1], Wen-Ting K. Tsai[3], Ziyue K. Jiang[1], Chau P. Tran[1], Chung Wang[1], Johnny Guan[1], Anna M. Wu[3], and Robert E. Reiter[1]

Abstract

Purpose: The inability to intraoperatively distinguish primary tumor, as well as lymphatic spread, increases the probability of positive surgical margins, tumor recurrence, and surgical toxicity. The goal of this study was to develop a tumor-specific optical probe for real-time fluorescence-guided surgery.

Experimental Design: A humanized antibody fragment against PSCA (A11 minibody, A11 Mb) was conjugated with a near-infrared fluorophore, IRDye800CW. The integrity and binding of the probe to PSCA were confirmed by gel electrophoresis, size-exclusion chromatography, and flow cytometry, respectively. The ability of the probe to detect tumor-infiltrated lymph nodes and metastatic lesions was evaluated in 2 xenograft models, as well as in transgenic mice expressing human PSCA (hPSCA). An invasive intramuscular model was utilized to evaluate the efficacy of the A11 Mb-IRDye800CW-guided surgery.

Results: A11 Mb was successfully conjugated with IRDye800CW and retained specific binding to PSCA. *In vivo* imaging showed maximal signal-to-background ratios at 48 hours. The A11 Mb-IRDye800CW specifically detected PSCA-positive primary tumors, tumor-infiltrated lymph nodes, and distant metastases with high contrast. Fluorescence guidance facilitated more complete tumor resection, reduced tumor recurrence, and improved overall survival, compared with conventional white light surgery. The probe successfully identified primary orthotopic tumors and metastatic lesions in hPSCA transgenic mice.

Conclusions: Real-time fluorescence image–guided surgery with A11 Mb-IRDye800CW enabled detection of lymph node metastases and positive surgical margins, facilitated more complete tumor removal, and improved survival, compared with white light surgery. These results may be translatable into clinical practice to improve surgical and patient outcomes.

Introduction

Prostate cancer is among the most prevalent male malignancies worldwide. It represents the second leading cause of cancer-related death for men in the United States (1). Radical prostatectomy remains one of the mainstays of treatment for localized prostate cancer. Complete tumor resection is critical for optimal cancer management. Positive surgical margins increase the likelihood of tumor recurrence and the need for secondary treatments such as adjuvant or salvage radiation, which may affect overall survival in some patients (2–4). However, extracapsular extension of prostate cancer is rarely visible during prostatectomy even under extreme magnification, and extended resection risks injury to surrounding tissues that may lead to urinary incontinence and sexual impotence (5, 6). Therefore, there is an urgent need for technologies that can aid visualization of tumor boundaries intraoperatively, which may reduce the incidence of positive surgical margins while reducing surgical toxicity.

Prostate cancer metastasizes most commonly to regional and distant lymph nodes (LNs), and detection of positive LNs may affect subsequent management (7, 8). Complete removal of involved regional nodes may also affect disease progression (9). However, there is currently no reliable way to detect and remove metastatic nodes intraoperatively. As many as 35% of involved nodes are located outside of traditional surgical templates (10), and the variability of nodal spread has made reliable identification of sentinel nodes difficult. Although improved molecular imaging with PET (e.g., PSMA, FACBC, and choline) may identify men with lymphatic involvement, PET may understage patients (11–13). Additionally, there is no simple way to identify the PET-visualized LNs intraoperatively. Therefore, an intraoperative navigation system or probe that can visualize cancer-bearing LNs and facilitate complete

[1]Department of Urology, David Geffen School of Medicine, University of California Los Angeles, Los Angeles, California. [2]Department of Urology, Shengjing Hospital, China Medical University, Shenyang, China. [3]Crump Institute for Molecular Imaging, Department of Molecular and Medical Pharmacology, University of California Los Angeles, Los Angeles, California

Note: Supplementary data for this article are available at Clinical Cancer Research Online (http://clincancerres.aacrjournals.org/).

Corresponding Author: Robert E. Reiter, University of California Los Angeles, 66-128A Center for the Health Sciences, 10833 LeConte Avenue, Los Angeles, CA 90095-1738. Phone: 310-794-7224; Fax: 310-206-5343; E-mail: rreiter@mednet.ucla.edu

doi: 10.1158/1078-0432.CCR-18-1382

Published OnlineFirst October 9, 2018; DOI: 10.1158/1078-0432.CCR-18-1382

Translational Relevance

The completeness of radical prostatectomy is the cornerstone of successful treatment for localized prostate cancer. However, the inability to visualize tumor margins and metastases to regional lymph nodes intraoperatively increases the likelihood of positive margins, tumor recurrence, and possibly side effects from overtreatment. Here, we report the development of a novel targeted fluorescence-imaging probe, A11 Mb-IRDye800CW, which recognizes a cell-surface marker of prostate tumors and visualizes PSCA-positive disease with high sensitivity and specificity. A11 Mb-IRDye800CW was successfully used to detect primary tumor and lymph node metastases, and for fluorescent image–guided surgery to visualize tumor margins, facilitating more complete cytoreduction, and thereby improving overall survival. The clinical translation of such probes has the potential to improve the surgical outcome of patients with prostate cancer significantly.

excision could affect prostate cancer management and clinical outcome.

An increasing number of investigators have endeavored to improve tumor detection and visualization with radioactive and optical probes (14, 15). Hand-held gamma detectors that detect the drainage of intraprostatically injected Technetium-99m have been used in prostate cancer surgical procedures with only modest efficacy given the variable drainage pattern of the prostate (16). Technetium-labeled small molecules targeting PSMA are also being explored (17). Fluorescent probes, such as intraprostatic indocyanine green (ICG), have also been administered in the peritumoral location to identify sentinel nodes during surgery with only modest success (18).

In the present study, we used a humanized engineered minibody that targets the cell-surface protein PSCA (A11 Mb). Antibody fragments such as the minibody retain the binding specificity of the parental antibody but exhibit faster tumor uptake and more rapid clearance from nontarget tissues to produce high contrast images (19). PSCA is overexpressed in 83% to 100% prostate cancer, and higher levels correlate with poor prognosis, LN spread, and metastatic disease (20, 21). Importantly, PSCA expression in normal tissues is highly restricted with no expression in bone marrow or LNs, common sites of prostate cancer metastasis (22). A11 Mb was labeled with the near-infrared (NIR) fluorescent dye IRDye800CW and evaluated for binding to PSCA-expressing prostate cancer cells *in vitro* and *in vivo*. In particular, we examined the ability of the A11 Mb-IRDye800CW to detect primary tumors and LN metastases in xenograft models and in a novel transgenic mouse model expressing the human *PSCA* gene. Finally, we evaluated the clinical potential of A11 Mb-IRDye800CW to provide surgical guidance and thereby to reduce the incidence of positive surgical margins, local recurrence, and to improve survival.

Materials and Methods

Reagents

A11 Mb, an engineered antibody fragment (scFv-C_H3 homodimer, 80 kDa), was developed and validated for preclinical *in vivo* targeting of PSCA at UCLA (23). Detailed biodistribution data for the A11 Mb were previously determined (24). IRDye800CW NHS ester (IRDye; 773-nm absorbance, 792-nm emission) was purchased from LI-COR Biotechnology (cat# 929-70020).

Conjugation of A11 Mb–IRDye800CW probe

The IRDye800CW fluorophore was conjugated with A11 Mb using NHS ester chemistry. Indicated molar excess of fluorescent dyes was incubated with 1 mg/mL A11 Mb in 0.1 M Na_2HPO_4 buffer (pH = 8.6) at room temperature for 2 hours. Excess free dye was removed using a Micro Bio-SpinP6 column (Bio-Rad, #7326221) according to the manufacturer's instruction. The final concentrations of conjugated product were measured photometrically by NanoDrop2000C spectrophotometer. The number of fluorophore molecules conjugated to each minibody molecule was calculated from IRDye800CW (780 nm) and protein (280 nm) concentrations. Sodium dodecyl sulfate polyacrylamide gel electrophoresis (SDS-PAGE) was used to verify the conjugation. The probe was stored at 4°C.

Size-exclusion chromatography

Size-exclusion chromatography was performed using a Superdex200 10/300GL column (GE Healthcare Life Sciences) on an ÄKTA Purifier (GE Healthcare Life Sciences) with PBS as mobile phase at a flow rate of 0.5 mL/minute. Absorbances at 280 nm for protein and at 780 nm for IRDye800CW were monitored during elution. β-Amylase (200 kDa), carbonic anhydrase (29 kDa), and cytochrome C (12.4 kDa; Sigma-Aldrich) were used as protein molecular weight standards.

Cell culture

CWR22Rv1 cells were obtained from ATCC and cultured in RPMI 1640 medium containing 10% fetal bovine serum (FBS), 1 mmol/L sodium pyruvate, and 1% penicillin–streptomycin–glutamine (PSG). PC3 cells (ATCC) were cultured in the Dulbecco modified Eagle medium (DMEM) with 5% FBS + 1% PSG. The mouse prostate cancer cell line RM9 and RM9-PSCA-Firefly-Luciferase (Fluc) cells were provided by the University of Texas MD Anderson Cancer Center and Dr. Saul Priceman (City of Hope). RM9 cells were grown in DMEM supplemented with 10% FBS + 1% PSG. 22Rv1-PSCA and PC3-PSCA were generated to express PSCA as previously described and cultured in the same media as mentioned for the parental cell lines above (23). Fluc-expression lentivirus was purchased from UCLA Vector Core and used to transduce 22Rv1, 22Rv1-PSCA, PC3, PC3-PSCA, and RM9 cells. All cells were maintained in a humidified incubator at 37°C and 5% CO_2.

Flow-cytometry analysis

22Rv1-PSCA and 22Rv1 cells were detached from plates with glucose-EDTA, stained with A11 Mb-IRDye800CW (1 μg per 1×10^6 cells) on ice for 2 hours, and washed with 2% FBS/PBS 3 times. A murine anti-human PSCA antibody, 1G8 (25), was used as a positive control with Alexa Fluor 647-goat-anti-mouse IgG secondary antibody (Invitrogen). A11 Mb-IRDye800CW binding to PSCA-expressing cells was tested using PC3-PSCA, PC3 cells, RM9-PSCA, and RM9 cells by flow cytometry as described above.

To determine the apparent affinity of A11 Mb-IRDye800CW, 5×10^5 22Rv1-PSCA and 22Rv1 cells were incubated with A11 Mb-IRDye800CW (dye-to-protein ratio 0.5) at concentrations ranging from 0 to 512 nmol/L in 200 μL of 2% FBS/PBS, for 3 hours at 4°C in triplicate. The mean fluorescence intensity of

Published OnlineFirst October 9, 2018; DOI: 10.1158/1078-0432.CCR-18-1382

each sample was fitted to a one-site saturation-binding model. Acquisition was performed with an LSRFortessa X-20 SORP flow cytometer (BD Biosciences), and analysis was performed with FlowJo 9.3.2. (TreeStar).

Human PSCA knock-in mouse

The human *PSCA* knock-in (hPSCA-KI) mouse model was generated by targeted insertion of hPSCA cDNA into the murine *Psca* gene through homologous recombination in the murine embryonic stem cells by standard gene-targeting methods (Supplementary Fig. S4). The hPSCA-KI mouse model is established by backcrossing with C57BL/6J for 6 generations. PCR primers (5′ to 3′) for genotyping were as follows: sense strand, mP-F6, TGTCACTGTTGACTGTGGGTAGCA; antisense strand, mP3-R1, CTTACTTGATAGGAGGGCTCAGCA, and hPSCA-1 3′, CCAGAGCAGCAGGCCGAGTGCA. PCR was performed with Taq DNA polymerase (Invitrogen) with 35 cycles of denaturation at 94°C for 25 seconds, annealing at 59.5°C for 25 seconds, and elongation at 72°C for 45 seconds.

Quantitative RT-PCR

Total RNA was isolated from various organs of hPSCA-KI mice using RNeasy mini kit (Qiagen). One microgram of total RNA was reverse transcribed, and semiquantitative RT-PCR was performed for human *PSCA* (30 cycles) and *GAPDH* (27 cycles; loading control) using Gene Amp RNA PCR kit (Applied Biosystems) according to the manufacturer's protocol.

Bioluminescence imaging

Bioluminescence imaging (BLI) was performed using the IVIS Lumina II *In Vivo* Imaging system (PerkinElmer) to monitor tumor growth, tumor recurrence, and LN metastases. Mice were administered with 150 mg/kg D-luciferin in 100 μL of normal saline by intraperitoneal injection, and anesthetized with 2% isoflurane. BLI images were acquired 10 minutes after the D-luciferin injection. Living Image software (Xenogen) was used to quantify bioluminescence signals. The value of bioluminescence signals was quantified in units of radiance, photons per second per centimeter squared per steradian (p/sec/cm^2/sr).

Fluorescence imaging

A Maestro II small animal optical imaging system (Cambridge Research and Instrumentation) was used for fluorescence imaging. The NIR filter set was selected with the extinction band pass filter at 684 to 729 nm, the emission filter at 745-nm longpass, and the acquisition settings from 740 to 950 nm in 10-nm steps. A11 Mb-IRDye800CW probe was injected through the lateral tail vein at 25 μg per mouse. Imaging was performed at 48 hours after injection (p.i.) or as indicated. Mice were anesthetized with 2% isoflurane at each imaging session for serial imaging at multiple time points. The fluorescent signals were unmixed and then measured using the software version 2.10 provided by the manufacturer (CRI, Maestro). The fluorescence intensity of PSCA$^+$ tumor was compared with the PSCA$^-$ tumor in the same tumor-bearing mouse.

Xenograft and transgenic knock-in mouse models

All animal experiments, housing, breeding, surgical procedures including pre- and postoperative care and analgesics administration were conducted in compliance with protocols approved by the Chancellor's Animal Research Committee at UCLA. Five- to 8-week-old male athymic nude mice (Charles River Laboratories), SCID mice (Taconic Biosciences), and C57BL/6 mice (The Jackson Laboratory) were purchased. Mice were fed irradiated alfalfa-free rodent diet (Envigo Teklad) to reduce nonspecific fluorescent signals in stomach and gut for 1 week prior to imaging experiments.

Subcutaneous model: 1×10^6 22Rv1-Fluc and 22Rv1-PSCA-Fluc cells in 100 μL Matrigel/PBS (1:1, v/v, Corning) were injected subcutaneously in the flank of nude mice. For each mouse, the parental tumor was implanted on the left flank and PSCA$^+$ tumor on the right. Tumor growth was monitored by caliper measurements. When tumors reached about 15 mm in diameter (10–14 days after injection), fluorescence imaging experiments were conducted.

LN metastasis model: 5×10^5 PC3-PSCA-Fluc cells in 40 μL PBS were injected into the left hock of SCID mice. BLI was performed weekly to monitor the tumor growth and metastases. When LN metastases were detected by BLI (about 7 weeks after the inoculation), fluorescence imaging experiments were conducted.

Intracardiac model: 1×10^4 PC3-PSCA-Fluc cells in 100 μL saline solution was injected into the left ventricle of SCID mice. Tumor establishment and metastases were monitored by BLI once a week. When multiple metastatic lesions were detected by BLI, A11 Mb-IRDye800CW probe was injected and fluorescence imaging was conducted at 48 hours after injection.

Intramuscular model: 1×10^6 22Rv1-PSCA-Fluc cells in 50 μL media/Matrigel (1:1, v/v, Corning) were injected into the posterior thigh muscle of the right leg in 20 nude mice, as previously described (26). BLI was used to monitor the tumor growth.

Transgenic knock-in mouse model: 1×10^6 RM9 and RM9-PSCA-Fluc cells in 100 μL Matrigel/PBS (1:1, v/v, Corning) were injected into the bilateral flank of hPSCA-KI mice to establish the subcutaneous tumor model as described above. For the orthotopic tumor model, 5×10^4 RM9-PSCA-Fluc cells in 5 μL PBS/Matrigel (1:1, v/v, Corning) were injected into dorsal prostate lobes of hPSCA-KI mice. Tumor growth was monitored by BLI.

Fluorescence-guided survival surgery of intramuscular 22Rv1-PSCA-Fluc tumors

For the resection surgery of intramuscular 22Rv1-PSCA-Fluc tumors, 20 tumor-bearing nude mice were injected with 25-μg A11 Mb-IRDye800CW probe 48 hours prior to the operation. Mice were anesthetized with a ketamine/xylazine mixture via intraperitoneal injection. The mice were randomized into 2 cohorts ($n = 10$ in each cohort), which received either tumor resection surgery under white light or white light surgery followed by fluorescence-guided surgery. The surgeon was blinded to the groupings while performing the first-round white light surgery. In one cohort, the secondary fluorescence-guided surgery was conducted to resect the residual tumors using a fluorescence dissecting microscope (Leica M205 FA, Leica Microsystems) at 10× magnification. Images of the fluorescent signal and surgical video were captured by a Leica DFC 9000GT monochrome camera with a filter for IRDye800 (excitation 710/75 nm and emission 810/90 nm) and displayed on an adjacent computer monitor during surgery. Images were analyzed with the use of Leica Application Suite X software. After surgery, any residual fluorescent tissue and/or tumor margins were surgically collected for histologic analysis. Nonfluorescent tissue margin was also collected as control. Mice were monitored and followed by BLI every 10 days after operation. When the recurrent tumor reached 15 mm

Published OnlineFirst October 9, 2018; DOI: 10.1158/1078-0432.CCR-18-1382

in diameter or mice's mobility was impaired, the mice were euthanized in accordance with our Animal Research Committee protocol to reduce unnecessary stress.

Immunohistochemistry

Tissue samples were fixed in formalin, paraffin-embedded (FFPE), sectioned, and stained with hematoxylin and eosin (H&E) by the UCLA pathology core facility. Four-μm-thick sections from the FFPE samples were used for immunohistochemistry (IHC) analyses using M.O.M. immunodetection kit (Vector, BMK-2202) according to the manufacturer's manual with modifications as follows. The tissue slides were incubated with the mouse IgG blocking reagent for 1 hour at room temperature, followed by incubation overnight with the anti-human PSCA primary antibody (Abcam, ab56338) at 4°C, and biotinylated anti-mouse secondary antibody (Vector, BMK-2202) at room temperature for 20 minutes. The slides were washed with PBS + 0.1% Tween 20 (PBST) for 5 minutes 3 times after each antibody incubation. The slides were counterstained with hematoxylin. The image was captured by an Olympus microscope (BX41).

Statistical analysis

All quantitative data were represented as mean ± SD. The 2-tailed Student *t* test was used for normally distributed values between 2 group comparisons, while Mann–Whitney *U* test was performed for variables without normal distribution. Kaplan–Meier analysis was used to determine the mice survival and differences between 2 treatment groups. Statistical analyses were performed with GraphPad Prism (version 6.0, GraphPad Software, Inc.). $P < 0.05$ was considered statistically significant.

Results

Development and characterization of A11 Mb-IRDye800CW

IRDye800CW NHS ester was conjugated to surface-exposed lysine residues on the engineered anti-PSCA A11 Mb (Fig. 1A). Because dye conjugation can affect the biodistribution and plasma clearance of the protein, we tested 2 different dye-to-protein (D:P) molar ratios. Two- and 5-fold molar excess of IRDye800CW relative to A11 Mb produced final D:P ratios 0.5 and 1.1, respectively. Successful conjugation was shown by the specific 80-kDa fluorescent bands (red) corresponding to the Coomassie blue stained bands of the same apparent molecular weight on an SDS-PAGE gel (Fig. 1B). The 5:1 conjugation reaction yielded a brighter band compared with the 2:1 reaction. The unconjugated A11 Mb was not visible by fluorescence imaging, as expected.

Purity and integrity of the A11 Mb-IRDye800CW were evaluated by size-exclusion chromatography. The unconjugated A11 Mb and A11 Mb-IRDye800CW (both D:P ratios at 0.5 and 1.1) eluted as a single elution peak with similar retention times (27.2 and 27.1 minutes, respectively), indicating that IRDye800CW conjugation did not interfere with dimeric minibody conformation and that the probe was not aggregated (Fig. 1C). The specificity of the minibody and its parental antibody has been reported extensively in prior work (23–25, 27, 28). Flow cytometry showed specific binding of the A11 Mb-IRDye800CW probe to 22Rv1-PSCA, with an apparent affinity of 26.5 ± 3.0 nmol/L. The selectivity of A11 Mb-IRDye800CW for PSCA was demonstrated by lack of binding to PSCA-negative parental 22Rv1 cells (Fig. 1D and E). Similarly, PSCA-specific binding of the probe to PC3-PSCA and RM9-PSCA cells was confirmed by flow cytometry, whereas there was no binding to the PSCA-negative parental PC3 and RM9 lines (Supplementary Fig. S1).

Determination of optimal imaging parameters

We evaluated the *in vivo* specificity of the A11 Mb-IRDye800CW probe in PSCA-positive 22Rv1-PSCA-Fluc and PSCA-negative 22Rv1-Fluc xenografts. Mice implanted with 22Rv1-PSCA-Fluc and 22Rv1-Fluc cells formed bioluminescent tumors after 2 weeks (Fig. 2A and B). A dose ranging experiment for the A11 Mb-IRDye800CW in *in vivo* imaging showed that increasing the amount of A11 Mb-IRDye800CW resulted in increasing fluorescent signals specific to $PSCA^+$ tumors (Supplementary Fig. S2). The dosage of A11 minibody at 25-μg protein (1 mg/kg) had been shown as a safe and effective dose in our previous reports (24, 28) and was used for the present study. Fluorescence imaging (extinction, 684 to 729 nm; emission, 789 nm; acquisition, 740 to 950 nm) after i.v. injection of 25-μg A11 Mb-IRDye800CW visualized PSCA-expressing tumors clearly, whereas PSCA-negative tumors were not visible (Fig. 2C). D:P ratios may affect the affinity, biodistribution, and nonspecific retention of A11 Mb-IRDye800CW. We compared A11 Mb-IRDye800CW with the final D:P ratio 0.5 and with the final D:P ratio 1.1 by imaging the mice with 22Rv1-PSCA-Fluc and PSCA-negative 22Rv1-Fluc xenografts ($n = 5$ in each group). At 48 hours after probe injection, higher contrast was seen for the probe with a D:P ratio of 0.5 (PSCA-positive to -negative signal ratio of 4.01 ± 1.14) compared with the probe with a D:P ratio of 1.1 (PSCA-positive to -negative signal ratio of 1.94 ± 0.43; Fig. 2D), suggesting that a lower D:P ratio of 0.5 led to the fluorescent images with higher contrast, while minimizing potential changes in pharmacokinetics of A11 Mb.

Serial imaging of tumor-bearing mice (24, 48, 72, 96, and 120 hours p.i.) determined the optimal time interval from probe injection to fluorescent imaging *in vivo*. Maximum florescence intensity and ratios of $PSCA^+$ and $PSCA^-$ tumors were determined at all time points. Strong fluorescent signal was observed in $PSCA^+$ tumors from 24 to 72 hours after injection, following which signal contrast diminished (Fig. 2E), suggesting that the probe could produce long-lasting signal and provide a sufficient time window for intraoperative imaging. The maximal $PSCA^+$ to $PSCA^-$ tumor fluorescence ratio was reached at 48 hours p.i. (Fig. 2F and G), which formed the basis for all future experiments.

Detection of lymphatic and distant metastases *in vivo* using A11 Mb-IRDye800CW

We next tested the ability of the A11 Mb-IRDye800CW probe to detect lymphatic and distant metastatic lesions, reasoning that *in vivo* visualization of regional and metastatic spread could guide surgical resection and potentially improve surgical outcomes in high-risk disease. To demonstrate the ability of A11 Mb-IRDye800CW to detect LN metastases, we established a novel LN metastasis model by hock injection of PC3-PSCA-Fluc cells in SCID mice. BLI detected metastases 7 weeks after tumor inoculation (Fig. 3A). As shown in Fig. 3B, multiple tumor-infiltrated LNs (popliteal LN, sciatic LN, lumbar LN, and medial iliac LN) were clearly visualized by PSCA-targeted A11 Mb-IRDye800CW fluorescence imaging. Although most fluorescent-positive nodes appeared enlarged and could be found under white light at autopsy, we also detected subclinical metastases in normal appearing LNs less than 1 mm in diameter, such as the external iliac LN shown in Fig. 3B and C. Tumor cell invasion in the fluorescence-positive LNs was further confirmed by *ex vivo* BLI

Published OnlineFirst October 9, 2018; DOI: 10.1158/1078-0432.CCR-18-1382

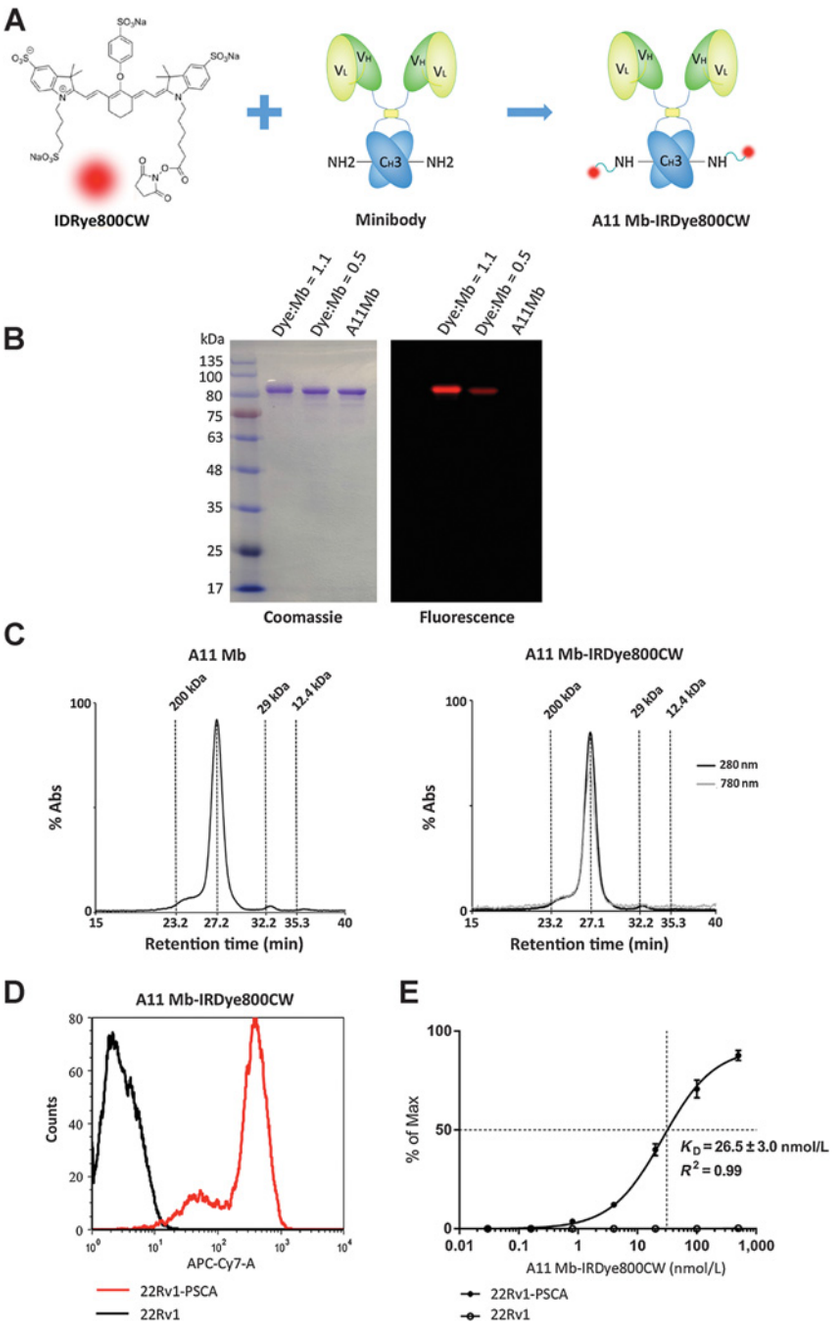

Figure 1.

Biochemical and functional characterization of IRDye800CW-conjugated anti-PSCA A11 Mb. **A,** Schematic of the conjugation of A11 Mb with IRDye800CW NHS ester (IRDye800CW). **B,** Nonreducing SDS-PAGE demonstrated the conjugation of A11 Mb with IRDye800CW. Higher dye-to-protein ratio (1.1) yielded a stronger fluorescent band than the reaction at lower ratio (0.5; right). Minibody (80 kDa) was visualized by Coomassie blue stain (left). **C,** Size-exclusion chromatography of purified A11 Mb and A11 Mb-IRDye800CW. Elution time of standard proteins is indicated. **D,** Flow cytometry analysis of the A11 Mb-IRDye800CW binding to 22Rv1-PSCA cells and to 22Rv1 parental cells. **E,** Quantitative flow cytometry showed specific binding of A11 Mb-IRDye800CW to 22Rv1-PSCA cells with an apparent affinity of 26.5 ± 3.0 nmol/L.

of the resected LN (Fig. 3C), as well as by histologic examination (Fig. 3D and E). These results demonstrate that A11 Mb-IRDye800CW can sensitively detect LN metastases.

Furthermore, A11 Mb-IRDye800CW was used to detect additional sites of metastasis established by intracardiac injection of PC3-PSCA-Fluc cells. At 6 weeks after injection, distant metastases were detected by BLI. Fluorescence imaging was performed 48 hours after administration of A11 Mb-IRDye800CW. For postmortem imaging, the skin was removed to reduce autofluorescence and to mimic an intraoperative setting. Multiple distant metastases were visualized as shown in Fig. 4A. Fluorescent signal in the liver represents minibody clearance and autofluorescence. Notably, PSCA-guided fluorescence imaging identified multiple metastases *in vivo*, including the tumor embedded in the left thigh muscle under the fat tissue, which would have been overlooked on bright field imaging (Fig. 4A). All metastatic tumor lesions were resected and confirmed by fluorescence *ex vivo* (Fig. 4B), as well as by histologic examination (Fig. 4C). These results suggest that the NIR signal generated by A11 Mb-IRDye800CW could enhance the ability of surgeons to find metastases intraoperatively, much as it enabled visualization of regional LNs.

Published OnlineFirst October 9, 2018; DOI: 10.1158/1078-0432.CCR-18-1382

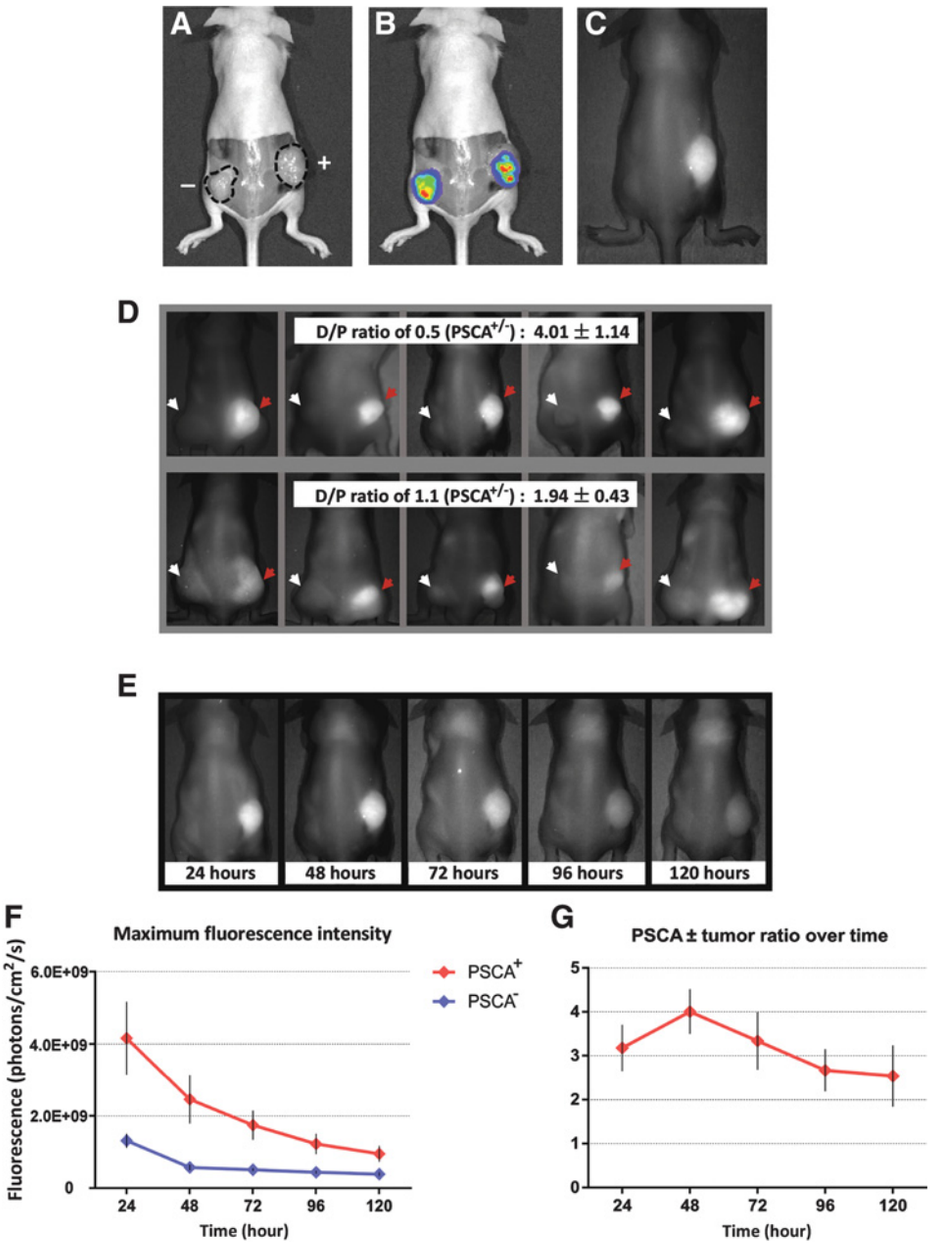

Figure 2.
Determination of the optimal imaging parameters for detection of PSCA-expressing tumors *in vivo* using A11 Mb-IRDye800CW. **A–C,** A representative mouse bearing 22Rv1-PSCA (right flank) and 22Rv1 (left flank). Tumors were imaged under white light (**A**), bioluminescence (**B**), and fluorescence (**C**). The contour of tumors is marked by the dashed line. Both 22Rv1-PSCA and 22Rv1 tumors showed bioluminescent signals due to luciferase expression. Fluorescent signals were detected by A11 Mb-IRDye800CW in the $PSCA^+$ tumor. **D,** Two different dye-to-protein ratios of A11 Mb-IRDye800CW probe intravenously administrated to tumor-bearing mice (22Rv1-PSCA, right flank; PSCA-negative 22Rv1, left flank; 5 mice per group). Fluorescence images were captured 48 hours after injection. Red arrow, $PSCA^+$ tumor; white arrow, $PSCA^-$ tumor. Mean of PSCA ± tumor signal ratios is indicated. **E–G,** Five mice bearing 22Rv1-PSCA (right flank) and PSCA-negative 22Rv1 (left flank) tumors received 25 μg of A11 Mb-IRDye800CW (D/P ratio: 0.5) intravenously and imaged at time indicated after probe injection. **E,** Serial images of a representative mouse over time. **F,** Average maximum fluorescence intensity of $PSCA^+$ and $PSCA^-$ tumors over time after probe injection. **G,** The average ratios of the maximum fluorescence intensities of $PSCA^+$ tumor compared with the $PSCA^-$ tumor from each mouse over time.

Surgical resection with real-time fluorescence guidance improves recurrence-free survival

To assess the potential utility of PSCA-targeted imaging with A11 Mb-IRDye800CW to aid tumor resection and improve recurrence-free survival, we compared surgical resection of prostate cancers by white light surgery alone to combined white light and fluorescence-guided surgery in a prospective, randomized study. We engrafted 22Rv1-PSCA-Fluc cells intramuscularly into nude mice ($n = 20$), which produced deeply invasive, difficult-to-resect tumors. Two weeks after tumor inoculation, tumor-bearing mice (confirmed by bioluminescence) were randomized into 2 groups with equal average preoperative tumor burdens (Fig. 5A and B). Forty-eight hours p.i., a surgeon blinded to treatment group resected all tumors under white light, attempting to resect tumor completely while preserving normal tissues (akin to radical prostatectomy). Following white light resection, mice randomized to the fluorescence cohort underwent a second surgery to remove fluorescing tissue. As shown in Fig. 5C, tumors were deeply invasive and the borders between tumor and surrounding tissues were not easily distinguishable under white light. In comparison, intraoperative fluorescence imaging facilitated clear visualization of residual fluorescing tumors. We could distinguish nearby neurovascular structures from tumor and achieve complete tumor resection (Supplementary Fig. S3 and Supplementary Video S1). Bioluminescent imaging 10 days after resection demonstrated that fluorescence-guided surgery resulted in more complete tumor

Published OnlineFirst October 9, 2018; DOI: 10.1158/1078-0432.CCR-18-1382

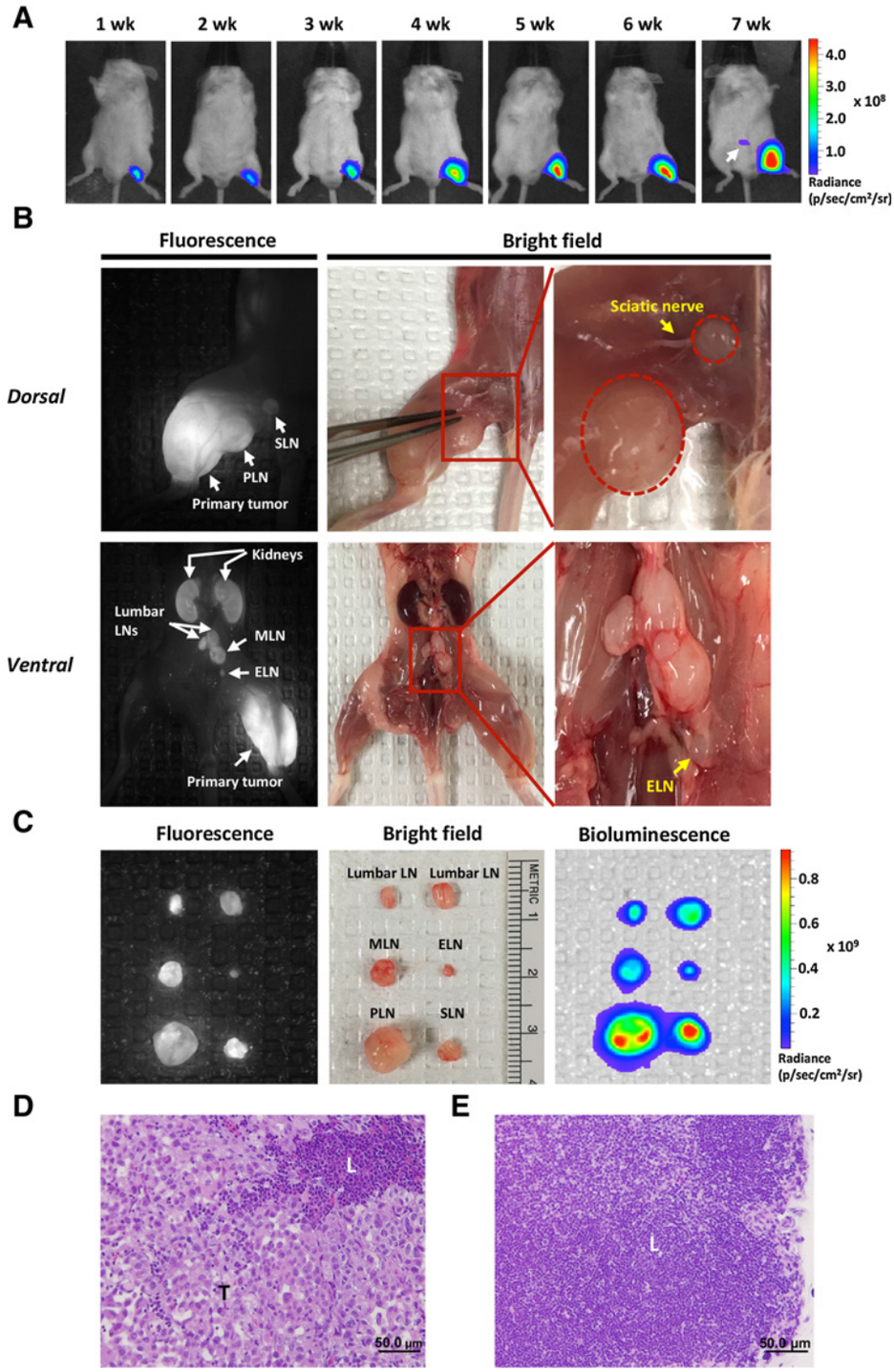

Figure 3.

Detection of tumor metastasis in LNs by A11 Mb-IRDye800CW fluorescent imaging. **A,** LN metastasis model was established by hock injection of PC3-PSCA-Fluc cells and the development of metastasis (white arrow) was monitored by BLI weekly. **B,** Optical fluorescence images of multiple metastatic LNs with A11 Mb-IRDye800CW probe. In dorsal view, the primary tumor and enlarged sentinel LNs (popliteal and sciatic LN) were detected by fluorescence imaging. In ventral view, metastatic lumbar LNs, medial iliac LN, and external iliac LN were detected by fluorescence imaging. **C,** *Ex vivo* optical imaging by BLI, fluorescence, and bright field. **D** and **E,** Histology of resected fluorescent LN (external iliac LN) showed tumor metastasis (**D**). Normal LN (**E**). T, tumor tissue; L, lymphatic tissue; SLN, sciatic LN; PLN, popliteal LN; MLN, medial iliac LN; ELN, external iliac LN. Scale bar, 50 μm.

removal compared with white light surgery alone. At this point, 8 of 10 mice in the white light surgery group showed detectable bioluminescence, whereas none of the mice in the fluorescence-guided surgery group showed residual signal (Fig. 5A). Bioluminescence of tumor burden as measured using region of interest analysis was significantly lower in the group that had undergone the fluorescence-guided surgery ($P < 0.001$). These differences in tumor burden were more significant at 20 days after operation (Fig. 5B). Histopathologic examination of the surgical margins of the thigh musculature (taken at the time of surgery) confirmed the presence of residual tumor in the white light group but not the fluorescence group (Fig. 5D). Significantly, the lower positive margin and decreased recurrence rate translated into an overall survival advantage among mice that received combined white

Published OnlineFirst October 9, 2018; DOI: 10.1158/1078-0432.CCR-18-1382

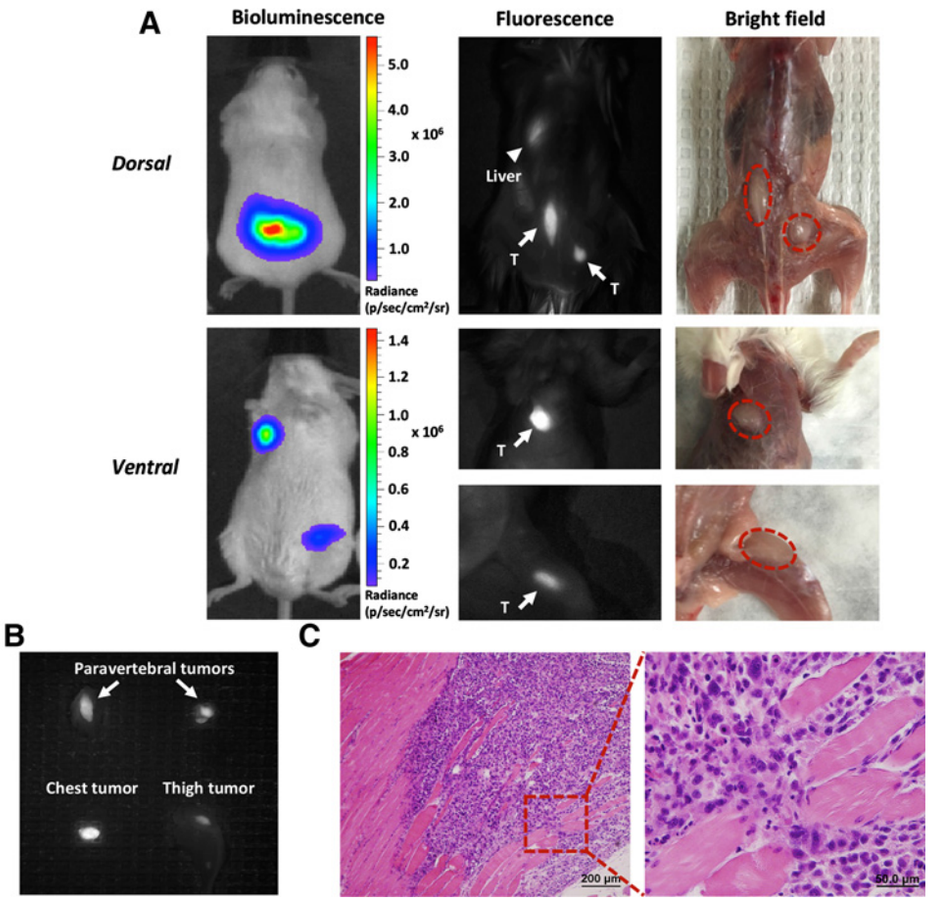

Figure 4.
Detection of PC3-PSCA-Fluc distant metastatic tumors by A11 Mb-IRDye800CW fluorescent imaging. **A,** Images of multiple distant metastases in SCID mice under the BLI, fluorescence and bright field. In dorsal view, fluorescence imaging identified the paravertebral tumors (arrows) that were detected by bioluminescence (marked by the red dotted lines in the bright field). Fluorescent signal in liver is due to clearance of minibody (arrowhead). In ventral view, the tumors located on the chest and the left thigh were detected by both bioluminescence and fluorescence imaging (arrows). **B,** *Ex vivo* fluorescent images of metastatic tumors from **A**. **C,** H&E staining of the resected fluorescent tissue sample (thigh tumor) confirmed tumor cell infiltration. T, tumor.

light and fluorescence surgery. The median survival for the white light surgery group was 24 days, whereas 90% of mice in the fluorescence-guided resection group survived with no evidence of tumor recurrence at the conclusion of the study at day 70 ($P < 0.001$; Fig. 5E).

A11 Mb-IRDye800CW fluorescence-guided surgical resection was also performed in SCID mice that developed PC3-PSCA-fluc metastatic LNs via hock injection. Real-time intraoperative fluorescence imaging provided identification of LNs with metastasis and facilitated surgical resection without injury to adjacent nerves (Supplementary Fig. S4 and Supplementary Video S2).

Imaging orthotopic and metastatic tumors with A11 Mb-IRDye800CW in a human *PSCA* knock-in mouse

One limitation of PSCA-specific antibody imaging in immunodeficient mouse models is that A11 minibody does not cross-react with the murine PSCA homologue, and whether binding of A11 Mb-IRDye800CW to normal tissue expressing PSCA could interfere with image contrast and hence impair surgical resection cannot be assessed. To evaluate A11 Mb-IRDye800CW fluorescence imaging in the context of normal *Psca* expression, we used a genetically engineered mouse model in which the human PSCA gene had been introduced into the murine Psca locus. As predicted based on the distribution of PSCA in normal human and murine tissues, endogenous h*PSCA* mRNA was detected in stomach, bladder, and prostate (Supplementary Fig. S5). RM9, a syngeneic mouse prostate cancer cell line, was engineered to express hPSCA and Fluc and implanted subcutaneously ($n = 5$; Supplementary Fig. S6) and orthotopically ($n = 8$) into hPSCA-KI mice (both homozygous and heterozygous males were used). Once tumor growth was detected by bioluminescence, the mice were administered A11 Mb-IRDye800CW and euthanized 48 hours later. Fluorescence imaging of hPSCA-KI mice bearing bilateral subcutaneous tumors showed strong signal in RM9-PSCA-Fluc tumors while no signal was detected in the control PSCA-negative RM9 tumors (Supplementary Fig. S6). The mice with orthotopic tumors were opened to expose the pelvic organs in order to simulate surgery. *In situ* NIR fluorescence imaging detected fluorescent signals in the antigen-positive tumors with high tumor to background contrast (Fig. 6A; Supplementary Fig. S6). Furthermore, in the orthotopic tumor model, fluorescence imaging clearly revealed the presence of LN metastases (mesentery and lumbar LNs), supporting the hypothesis that intraoperative imaging can be used to identify regional and distant LN metastases. Next, we evaluated the probe's biodistribution by harvesting the major organs, prostate, and metastatic lesions and examining them with *ex vivo* fluorescence imaging. As shown in Fig. 6B, the prostate (with cancer), metastatic LNs, liver, kidneys, and stomach emitted fluorescent signals, while the other organs and tissues (lung, heart, spleen, bone, pancreas, and muscle) showed no significant fluorescence. Fluorescent signals in liver, kidney, and bladder are due to metabolism and urinary excretion of the probe, although some bladder fluorescence is attributable to endogenous expression (Supplementary Fig. S7). The strong signal in

Published OnlineFirst October 9, 2018; DOI: 10.1158/1078-0432.CCR-18-1382

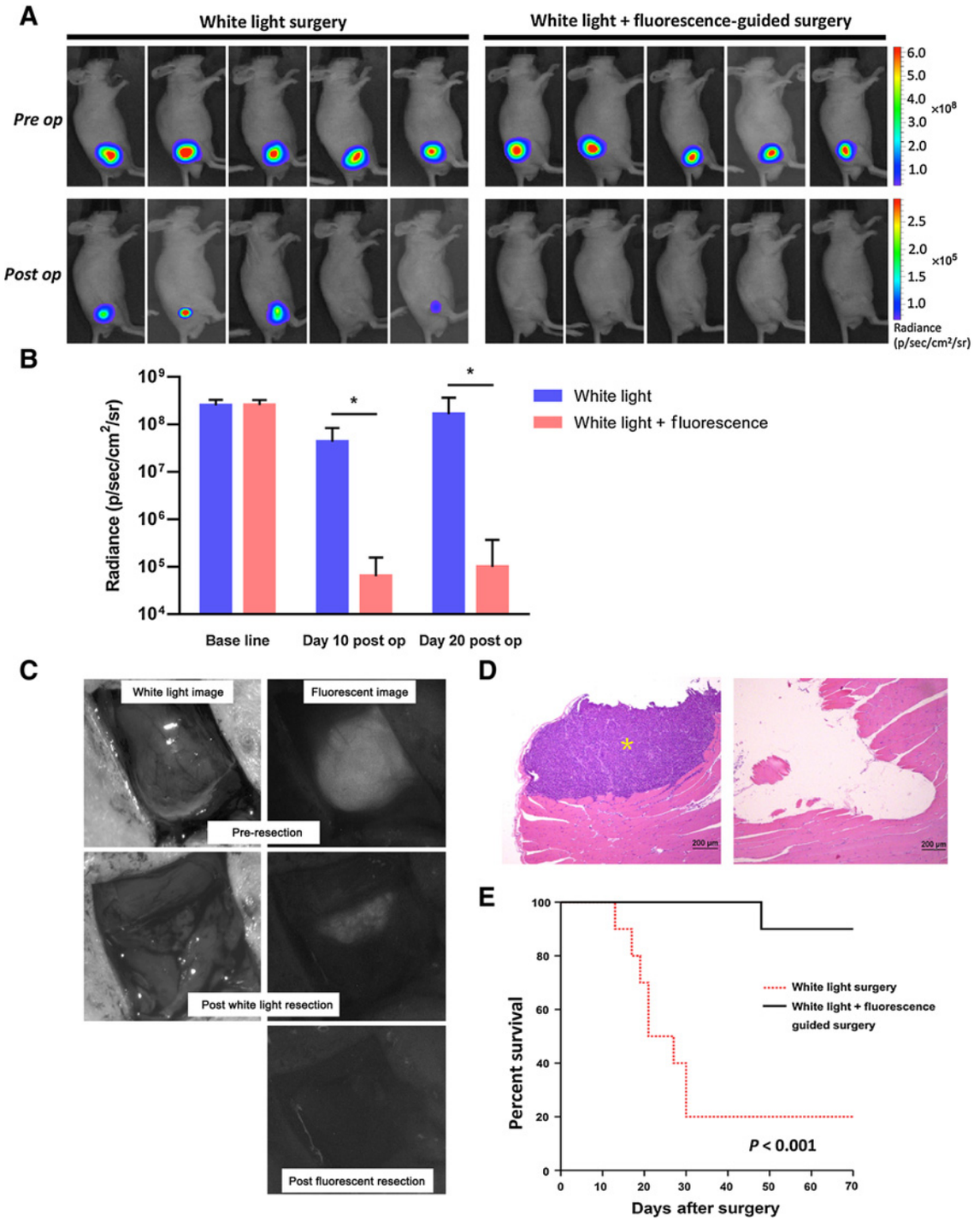

Figure 5.

A11 Mb-IRDye800CW fluorescent imaging enabled surgical resection of infiltrative 22Rv1-PSCA-Fluc tumors under fluorescence guidance in real time. **A,** Representative pre- and postoperative bioluminescence images: white light surgery only ($n = 10$) and white light + fluorescence-guided surgery ($n = 10$). **B,** Tumor resection under fluorescent guidance significantly decreased the tumor burden at days 10 and 20 after operation, compared with white light surgery alone. *, $P < 0.001$. **C,** Intraoperative images of tumors under white light and fluorescence before and after tumor resection surgery. **D,** H&E histology of surgical margins showing residual tumor tissue after white light surgery (left) and negative surgical margin after secondary fluorescence-guided surgery (right). Yellow asterisk, tumor cells. **E,** Kaplan–Meier analysis showing a significant difference in survival of the fluorescence-guided surgery group ($n = 10$) and the mice that received conventional white light surgery ($n = 10$; log-rank $P < 0.001$).

Published OnlineFirst October 9, 2018; DOI: 10.1158/1078-0432.CCR-18-1382

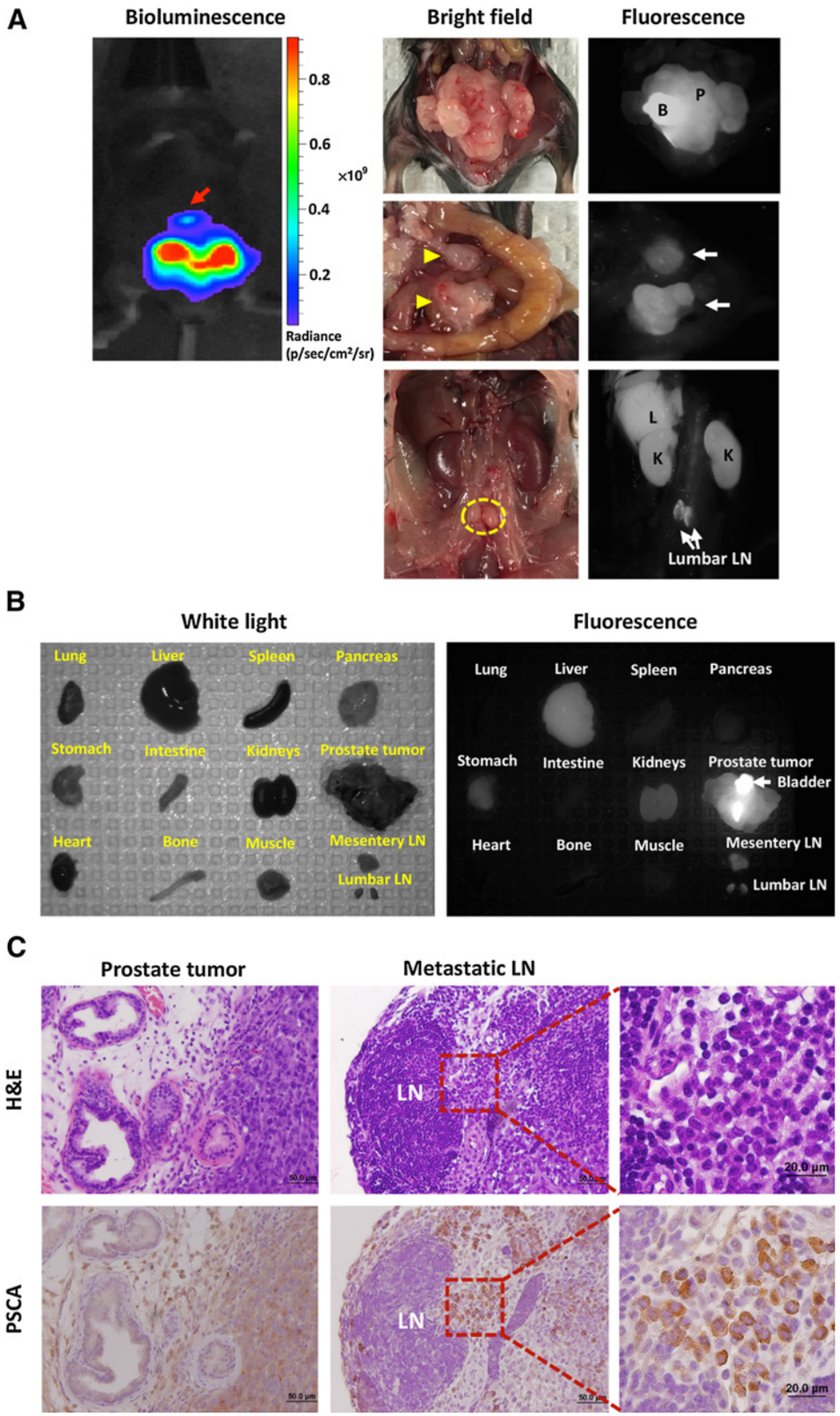

Figure 6.
Optical imaging with A11 Mb-IRDye800CW enabled detection of orthotopically implanted intraprostatic tumors and metastatic lesions in human *PSCA* knock-in transgenic mice. **A,** Bioluminescence image of the prostate tumor and metastasis (red arrow; left top panel). Optical images of the orthotopic tumor, mesentery (yellow arrowhead), and lumbar LNs (yellow dotted line) metastases under bright field and fluorescence. Fluorescence imaging with A11 Mb-IRDye800CW detected the orthotopic tumor and multiple LNs metastases. Nonspecific fluorescent signals in the liver and kidneys are due to the clearance of probe. **B,** *Ex vivo* optical imaging for evaluation of probe biodistribution in transgenic mouse. **C,** H&E and IHC staining for human PSCA confirmed the presence of tumor cells and PSCA expression in the prostate and metastatic lumbar LNs. **B,** Bladder; P, prostate tumor; L, liver; K, kidney; LN, lymph node.

stomach was due in part to autofluorescence of food contents in the stomach despite use of alfalfa-free pellets, although again some signal is attributable to expression of PSCA in stomach mucosa (Supplementary Fig. S7). Finally, histology and IHC staining for PSCA confirmed the presence of cancer in the prostate and involved LNs (Fig. 6C). These results demonstrate the ability

Published OnlineFirst October 9, 2018; DOI: 10.1158/1078-0432.CCR-18-1382

of A11 Mb-IRDye800CW to detect local and metastatic prostate cancers *in vivo* in a model most analogous to patients with prostate cancer.

Discussion

Effective intraoperative image-guided surgery is a major unmet need in the management of men with prostate cancer. Fluorescence image–guided surgery (FIGS) is one of the most promising methodologies to improve disease visualization, aiding tumor identification and complete resection, while avoiding injury to adjacent normal tissues such as the neurovascular bundles in the case of prostate cancer. Recent reports have demonstrated successful utilization of intraoperative fluorescent probes for imaging of tumors and in sentinel LN mapping of various types of cancer (29–31).

Here, we conjugated the NIR dye IRDye800CW to the anti-PSCA antibody fragment, A11 Mb, and tested whether fluorescence imaging with A11 Mb-IRDye800CW could aid in resection of a locally invasive prostate tumor during surgery, decrease tumor recurrence, and improve prognosis. Although it is not technically feasible to perform radical prostatectomy in mouse models, the deeply invasive intramuscular tumor model we used does recapitulate important features of radical prostatectomy, such as the difficulty of margin visualization under white light. Special attention was paid to conduct unbiased surgery blinded to the groupings during the first round of standard surgery under white light with the goal of removing as much tumor as possible while preserving adjacent normal tissues, akin to radical prostatectomy. The postoperative bioluminescence imaging studies clearly showed that more complete resection of cancer tissue was achieved by FIGS. Our results demonstrate that the new NIR probe clearly delineated between antigen-expressing tumor and healthy surrounding tissues, allowing the surgeon to precisely visualize tumor margins and achieve more complete tumor resection. This in turn led to a lower residual tumor burden, reduced recurrence, and ultimately significantly improved overall survival.

We previously reported that intraoperative fluorescent guidance with a Cy5 labeled PSCA diabody fragment (scFv dimer) could also enable detection of residual tumor and reduce positive surgical margins (26). In this study, IRDye800CW was selected because of its preliminary success in clinical studies due to its low autofluorescence and high spatial resolution (32, 33). Rosenthal and colleagues evaluated anti-EGFR cetuximab-IRDye800CW in patients with head and neck cancer. Cetuximab-IRDye800CW was well tolerated and provided robust fluorescence contrast between tumor and normal tissue during intraoperative surgical resection (32). More recently, Lamberts and colleagues injected bevacizumab-IRDye800CW intravenously into patients with primary breast cancer, targeting VEGF-A. The group demonstrated the safety and feasibility of a NIR fluorescent probe to improve tumor margin detection intraoperatively (33). In addition to its safety, NIR fluorescent emission can be captured with frame rates of up to 30 fps, which is ideal for real-time detection. Perhaps most importantly, IRDye800CW is compatible with existing laparoscopic and robotic surgical systems, which may facilitate clinical translation of this probe.

We selected the 80-kDa minibody format for this study for a number of reasons. First, anti-PSCA A11 minibody was capable of binding specifically PSAC-expressing tumors after conjugation with IRDye800CW, as shown by flow-cytometry study and by PSCA-specific fluorescent signals detected *in situ* and *ex vivo* compared with PSCA-negative control tumors and organs. A11 Mb-IRDye800CW *in vivo* imaging was able to produce PSCA-specific fluorescent signals with high contrast for all 3 cell lines used in the study that express PSCA at various levels; the PC3-PSCA and 22Rv1-PSCA cell lines have PSCA cell-surface density 5.2×10^5 antigens/cell and 2.1×10^6 antigens/cell, respectively; RM9-PSCA cells have lower PSCA expression than 22Rv1-PSCA as determined by IHC and flow cytometry (data not shown). Importantly, the range of PSCA expression levels is comparable to the expression observed in prostate cancer patient samples. Second, the fast tumor uptake and the more rapid clearance from nontarget tissues of A11 minibody compared with the parental antibody can provide practical time window for surgery. A 1- to 3-day window offers flexibility in scheduling and performance of probe injection and surgical procedure. Additionally, the engineered antibody fragment can be labeled with more than a single moiety. Tsai and colleagues have adapted the A11 minibody for dual PET and fluorescent imaging, which could allow for upfront PET imaging to localize tumor, followed by fluorescence guidance to identify and resect those lesions (34).

Lymphatic drainage is a major route of tumor dissemination in prostate cancer. The ability to detect nodal metastases and achieve complete nodal resection in patients with high-risk disease in the operating room is a major unmet clinical need for prostate cancer. Various fluorescent imaging probes have been developed to better visualize and characterize the lymphatic system. The NIR dye, ICG, has been extensively studied for intraoperative sentinel LN mapping in a variety of tumors such as skin, breast, and gastrointestinal cancers (35–37). In patients with cervical cancer, ICG showed sentinel node identification rates comparable with conventional radiotracers and blue dyes (38). However, the nontumor-specific property makes this dye less than ideal for real-time visualization of metastatic tumor lesions. Recently, Cai and colleagues developed Alexa Fluor 680–conjugated bombesin (BBN) peptides against the gastrin-releasing peptide receptor and detected LN metastases in mouse models. Fluorescence imaging with BBN-Alexa Fluor 680 was performed for up to 6 hours after postinjection (39). In the current study, we established a prostate xenograft mouse model with multiple LN metastases via hock injection. The tumor-infiltrated LNs, including small nodes with early-stage microscopic metastasis that may be easily overlooked by gross examination, were clearly detected by A11 Mb-IRDye800CW after systemic administration into the mice. The smallest size of affected lymph node (external iliac LN) imaged by A11 Mb-IRDye800CW was only 1 mm in diameter, and it was not distinguishable from normal nodes. The result indicates the potential of FIGS with A11 Mb-IRDye800CW in resecting tumors that are too small to identify as nodal disease at all or as pathologic nodal disease. One of the challenges of developing effective lymphatic imaging agents is delivering the probe into the LNs. A11 Mb-IRDye800CW showed stable retention in LNs due to the specific binding to tumor cells mediated by the antibody fragment. These advantages were confirmed in our study, demonstrating the suitability of the probe for detection and resection of involved LNs. The potential use of the probe in assisting in identifying residual disease for salvage pelvic node dissections is noteworthy.

PSMA ligand PET imaging is becoming recognized as a powerful tool for detection of a recurrent prostate cancer and for nodal

Published OnlineFirst October 9, 2018; DOI: 10.1158/1078-0432.CCR-18-1382

and bone metastases for high-risk primary prostate cancer (40). Although PSMA-targeted fluorescent imaging is possible, the current generation of PET probes are small molecules whose binding may be hindered by a large optical moiety such as IRDye800. PSCA-directed intraoperative imaging could be used in conjunction with either a PSCA PET probe or any of the current PSMA PET probes. In addition to a majority of prostate cancers, PSCA is also expressed by other malignancies such as pancreatic, bladder, and ovarian cancers, to which A11 Mb-IRDye800CW FIGS may be applied.

A unique feature of this study was the evaluation of A11 Mb-IRDye800CW in a transgenic mouse that expresses hPSCA. The distribution of PSCA in this mouse model was concordant with that in humans (stomach, bladder, and prostate). Primary tumor and metastatic lesions were clearly distinguishable from background with a high signal-to-background ratio. Although hPSCA-KI mice had low-level expression of PSCA in the normal mucosa of the stomach as determined by IHC and mRNA expression (41), imaging of the surgical area with A11 Mb-IRDye800CW was not interfered by the fluorescence in the stomach because of the distance between the 2 organs. In contrast, the bladder had strong fluorescent signal, although this was largely caused by clearance of the probe through the kidney. Residual signal from the bladder after removal of urine was faint, consistent with weak and spotty expression seen by IHC. Diuresis or catheterization could be used to clear bladder signal during surgery in order to avoid any potential loss of contrast at the level of the bladder neck. These results demonstrate the feasibility of the A11 Mb-IRDye800CW for fluorescence imaging and intraoperatively distinguishing local, locoregional and metastatic prostate cancer from normal tissue. In the present study, we explored the sensitivity, specificity, and utility of fluorescent imaging in multiple models, including distant LNs and other soft-tissue metastases. We can envision changes in practice with the advent of better PET imaging that may lend themselves to fluorescent imaging and complete surgical resection of distant metastases. The development of novel targeted fluorescent probe has the potential to transform the surgical landscape of prostate cancer, particularly in the age of robotics and cameras capable of detecting fluorescent images.

Disclosure of Potential Conflicts of Interest

A.M. Wu is a consultant/advisory board member for and holds ownership interest (including patents) in ImaginAb, Inc. R.E. Reiter is a consultant/advisory board member for and holds ownership interest (including patents) in ImaginAb, Inc. No potential conflicts of interest were disclosed by the other authors.

Authors' Contributions

Conception and design: M. Zhang, N. Kobayashi, K.A. Zettlitz, W.-T.K. Tsai, A.M. Wu, R.E. Reiter

Development of methodology: M. Zhang, N. Kobayashi, K.A. Zettlitz, E.A. Kono, W.-T.K. Tsai, Z.K. Jiang, C.P. Tran, R.E. Reiter

Acquisition of data (provided animals, acquired and managed patients, provided facilities, etc.): M. Zhang, N. Kobayashi, E.A. Kono, J. Yamashiro, J. Guan

Analysis and interpretation of data (e.g., statistical analysis, biostatistics, computational analysis): M. Zhang, N. Kobayashi, K.A. Zettlitz, W.-T.K. Tsai, R.E. Reiter

Writing, review, and/or revision of the manuscript: M. Zhang, N. Kobayashi, K.A. Zettlitz, E.A. Kono, W.-T.K. Tsai, A.M. Wu, R.E. Reiter

Administrative, technical, or material support (i.e., reporting or organizing data, constructing databases): N. Kobayashi, E.A. Kono, C.P. Tran, C. Wang

Study supervision: M. Zhang, N. Kobayashi

Acknowledgments

In vivo fluorescence imaging was performed at the California Nano-Systems Institute Advanced Light Microscopy/Spectroscopy and the Macro-Scale Imaging Shared Facilities at UCLA. This work was supported by NIH grants R01 CA174294, P30 CA016042, UCLA SPORE in Prostate Cancer 5P50CA092131-12, and Department of Defense W81 XWH-15-1-0725. Imaging, flow cytometry, pathology core services were supported by the Jonsson Comprehensive Cancer Center (P30 CA016042).

Received May 10, 2018; revised August 22, 2018; accepted October 3, 2018; published first October 9, 2018.

References

1. Siegel RL, Miller KD, Jemal A. Cancer statistics, 2016. CA Cancer J Clin 2016;66:7–30.
2. Chalfin HJ, Dinizo M, Trock BJ, Feng Z, Partin AW, Walsh PC, et al. Impact of surgical margin status on prostate-cancer-specific mortality. BJU Int 2012;110:1684–9.
3. Stephenson AJ, Eggener SE, Hernandez AV, Klein EA, Kattan MW, Wood DP Jr., et al. Do margins matter? The influence of positive surgical margins on prostate cancer-specific mortality. Eur Urol 2014;65:675–80.
4. Izard JP, True LD, May P, Ellis WJ, Lange PH, Dalkin B, et al. Prostate cancer that is within 0.1 mm of the surgical margin of a radical prostatectomy predicts greater likelihood of recurrence. Am J Surg Pathol 2014;38:333–8.
5. Hruby S, Englberger C, Lusuardi L, Schatz T, Kunit T, Abdel-Aal AM, et al. Fluorescence guided targeted pelvic lymph node dissection for intermediate and high risk prostate cancer. J Urol 2015;194:357–63.
6. Saika T, Miura N, Fukumoto T, Yanagihara Y, Miyauchi Y, Kikugawa T. Role of robot-assisted radical prostatectomy in locally advanced prostate cancer. Int J Urol 2018;25:30–5.
7. Vilaseca A, Nguyen DP, Touijer KA. Should fluorescence mapping be used to guide pelvic lymph node dissection? J Urol 2015;194:280–1.
8. Chennamsetty A, Zhumkhawala A, Tobis SB, Ruel N, Lau CS, Yamzon J, et al. Lymph node fluorescence during robot-assisted radical prostatectomy with indocyanine green: prospective dosing analysis. Clin Genitourin Cancer 2017;15:e529–e34.
9. Yuh B, Artibani W, Heidenreich A, Kimm S, Menon M, Novara G, et al. The role of robot-assisted radical prostatectomy and pelvic lymph node dissection in the management of high-risk prostate cancer: a systematic review. Eur Urol 2014;65:918–27.
10. Mattei A, Fuechsel FG, Bhatta Dhar N, Warncke SH, Thalmann GN, Krause T, et al. The template of the primary lymphatic landing sites of the prostate should be revisited: results of a multimodality mapping study. Eur Urol 2008;53:118–25.
11. Freitag MT, Radtke JP, Hadaschik BA, Kopp-Schneider A, Eder M, Kopka K, et al. Comparison of hybrid (68)Ga-PSMA PET/MRI and (68)Ga-PSMA PET/CT in the evaluation of lymph node and bone metastases of prostate cancer. Eur J Nucl Med Mol Imaging 2016;43:70–83.
12. Kanagawa M, Doi Y, Oka S, Kobayashi R, Nakata N, Toyama M, et al. Comparison of trans-1-amino-3-[18F]fluorocyclobutanecarboxylic acid (anti-[18F]FACBC) accumulation in lymph node prostate cancer metastasis and lymphadenitis in rats. Nucl Med Biol 2014;41:545–51.
13. Schwenck J, Rempp H, Reischl G, Kruck S, Stenzl A, Nikolaou K, et al. Comparison of (68)Ga-labelled PSMA-11 and (11)C-choline in the detection of prostate cancer metastases by PET/CT. Eur J Nucl Med Mol Imaging 2017;44:92–101.
14. Lutje S, Rijpkema M, Goldenberg DM, van Rij CM, Sharkey RM, McBride WJ, et al. Pretargeted dual-modality immuno-SPECT and near-infrared

Published OnlineFirst October 9, 2018; DOI: 10.1158/1078-0432.CCR-18-1382

fluorescence imaging for image-guided surgery of prostate cancer. Cancer Res 2014;74:6216–23.
15. Bu L, Shen B, Cheng Z. Fluorescent imaging of cancerous tissues for targeted surgery. Adv Drug Deliv Rev 2014;76:21–38.
16. Stroup SP, Kane CJ, Farchshchi-Heydari S, James CM, Davis CH, Wallace AM, et al. Preoperative sentinel lymph node mapping of the prostate using PET/CT fusion imaging and Ga-68-labeled tilmanocept in an animal model. Clin Exp Metast 2012;29:673–80.
17. Hillier SM, Maresca KP, Lu G, Merkin RD, Marquis JC, Zimmerman CN, et al. 99mTc-labeled small-molecule inhibitors of prostate-specific membrane antigen for molecular imaging of prostate cancer. J Nucl Med 2013;54:1369–76.
18. Polom K, Murawa D, Rho YS, Nowaczyk P, Hunerbein M, Murawa P. Current trends and emerging future of indocyanine green usage in surgery and oncology: a literature review. Cancer 2011;117:4812–22.
19. Holliger P, Hudson PJ. Engineered antibody fragments and the rise of single domains. Nat Biotechnol 2005;23:1126–36.
20. Lam JS, Yamashiro J, Shintaku IP, Vessella RL, Jenkins RB, Horvath S, et al. Prostate stem cell antigen is overexpressed in prostate cancer metastases. Clin Cancer Res 2005;11:2591–6.
21. Gu Z, Thomas G, Yamashiro J, Shintaku IP, Dorey F, Raitano A, et al. Prostate stem cell antigen (PSCA) expression increases with high gleason score, advanced stage and bone metastasis in prostate cancer. Oncogene 2000;19:1288–96.
22. Raff AB, Gray A, Kast WM. Prostate stem cell antigen: a prospective therapeutic and diagnostic target. Cancer Lett 2009;277:126–32.
23. Knowles SM, Tavare R, Zettlitz KA, Rochefort MM, Salazar FB, Jiang ZK, et al. Applications of immunoPET: using 124I-anti-PSCA A11 minibody for imaging disease progression and response to therapy in mouse xenograft models of prostate cancer. Clin Cancer Res 2014;20:6367–78.
24. Knowles SM, Zettlitz KA, Tavare R, Rochefort MM, Salazar FB, Stout DB, et al. Quantitative immunoPET of prostate cancer xenografts with 89Zr- and 124I-labeled anti-PSCA A11 minibody. J Nucl Med 2014;55:452–9.
25. Gu Z, Yamashiro J, Kono E, Reiter RE. Anti-prostate stem cell antigen monoclonal antibody 1G8 induces cell death in vitro and inhibits tumor growth in vivo via a Fc-independent mechanism. Cancer Res 2005; 65:9495–500.
26. Sonn GA, Behesnilian AS, Jiang ZK, Zettlitz KA, Lepin EJ, Bentolila LA, et al. Fluorescent image-guided surgery with an anti-prostate stem cell antigen (PSCA) diabody enables targeted resection of mouse prostate cancer xenografts in real time. Clin Cancer Res 2016;22:1403–12.
27. Leyton JV, Olafsen T, Lepin EJ, Hahm S, Bauer KB, Reiter RE, et al. Humanized radioiodinated minibody for imaging of prostate stem cell antigen-expressing tumors. Clin Cancer Res 2008;14:7488–96.
28. Lepin EJ, Leyton JV, Zhou Y, Olafsen T, Salazar FB, McCabe KE, et al. An affinity matured minibody for PET imaging of prostate stem cell antigen (PSCA)-expressing tumors. Eur J Nucl Med Mol Imaging 2010;37:1529–38.
29. Chen Y, Dhara S, Banerjee SR, Byun Y, Pullambhatla M, Mease RC, et al. A low molecular weight PSMA-based fluorescent imaging agent for cancer. Biochem Biophys Res Commun 2009;390:624–9.
30. Hoogstins CE, Tummers QR, Gaarenstroom KN, de Kroon CD, Trimbos JB, Bosse T, et al. A novel tumor-specific agent for intraoperative near-infrared fluorescence imaging: a translational study in healthy volunteers and patients with ovarian cancer. Clin Cancer Res 2016;22:2929–38.
31. Proulx ST, Luciani P, Christiansen A, Karaman S, Blum KS, Rinderknecht M, et al. Use of a PEG-conjugated bright near-infrared dye for functional imaging of rerouting of tumor lymphatic drainage after sentinel lymph node metastasis. Biomaterials 2013;34:5128–37.
32. Rosenthal EL, Warram JM, de Boer E, Chung TK, Korb ML, Brandwein-Gensler M, et al. Safety and Tumor Specificity of Cetuximab-IRDye800 for surgical navigation in head and neck cancer. Clin Cancer Res 2015;21: 3658–66.
33. Lamberts LE, Koch M, de Jong JS, Adams ALL, Glatz J, Kranendonk MEG, et al. Tumor-Specific Uptake of Fluorescent Bevacizumab-IRDye800CW microdosing in patients with primary breast cancer: a phase I Feasibility Study. Clin Cancer Res 2017;23:2730–41.
34. Zettlitz KA, Tsai WK, Knowles SM, Kobayashi N, Donahue TR, Reiter RE, et al. Dual-modality immunoPET and near-infrared fluorescence (NIRF) imaging of pancreatic cancer using an anti-prostate cancer stem cell antigen (PSCA) cys-diabody. J Nucl Med 2018. doi 10.2967/jnumed.117.207332.
35. Namikawa K, Tsutsumida A, Tanaka R, Kato J, Yamazaki N. Limitation of indocyanine green fluorescence in identifying sentinel lymph node prior to skin incision in cutaneous melanoma. Int J Clin Oncol 2014;19:198–203.
36. Toh U, Iwakuma N, Mishima M, Okabe M, Nakagawa S, Akagi Y. Navigation surgery for intraoperative sentinel lymph node detection using Indocyanine green (ICG) fluorescence real-time imaging in breast cancer. Breast Cancer Res Treat 2015;153:337–44.
37. Currie AC, Brigic A, Thomas-Gibson S, Suzuki N, Moorghen M, Jenkins JT, et al. A pilot study to assess near infrared laparoscopy with indocyanine green (ICG) for intraoperative sentinel lymph node mapping in early colon cancer. Eur J Surg Oncol 2017;43:2044–51.
38. Buda A, Crivellaro C, Elisei F, Di Martino G, Guerra L, De Ponti E, et al. Impact of indocyanine green for sentinel lymph node mapping in early stage endometrial and cervical cancer: comparison with conventional radiotracer (99m)Tc and/or Blue Dye. Ann Surg Oncol 2016;23:2183–91.
39. Cai QY, Yu P, Besch-Williford C, Smith CJ, Sieckman GL, Hoffman TJ, et al. Near-infrared fluorescence imaging of gastrin releasing peptide receptor targeting in prostate cancer lymph node metastases. Prostate 2013;73:842–54.
40. Schwarzenboeck SM, Rauscher I, Bluemel C, Fendler WP, Rowe SP, Pomper MG, et al. PSMA Ligands for PET imaging of prostate cancer. J Nucl Med 2017;58:1545–52.
41. Bahrenberg G, Brauers A, Joost HG, Jakse G. Reduced expression of PSCA, a member of the LY-6 family of cell surface antigens, in bladder, esophagus, and stomach tumors. Biochem Biophys Res Commun 2000;275:783–8.

AACR American Association for Cancer Research

Clinical Cancer Research

Near-Infrared Dye-Labeled Anti-Prostate Stem Cell Antigen Minibody Enables Real-Time Fluorescence Imaging and Targeted Surgery in Translational Mouse Models

Mo Zhang, Naoko Kobayashi, Kirstin A. Zettlitz, et al.

Clin Cancer Res 2019;25:188-200. Published OnlineFirst October 9, 2018.

A dual-modality linker enables site-specific conjugation of antibody fragments for ^{18}F-immunoPET and fluorescence imaging

Kirstin A Zettlitz[1#], Christopher M Waldmann[1#], Wen-Ting K Tsai[1], Richard Tavaré[1], Jeffrey Collins[1], Jennifer M Murphy[1], Anna M Wu[1]

[1]Crump Institute for Molecular Imaging, Department of Molecular and Medical Pharmacology, David Geffen School of Medicine at University of California Los Angeles, CA, USA

[#]contributed equally to this work

For correspondence or reprints contact either of the following:

Kirstin A Zettlitz, Department of Molecular Imaging and Therapy, Beckman Research Institute at City of Hope, 1500 East Duarte Road, Duarte, CA 91010. ORCID ID: 0000-0003-4870-6603. E-mail: kzettlitz@coh.org.

Jennifer M Murphy, Crump Institute for Molecular Imaging at UCLA, 570 Westwood Plaza, Los Angeles, CA 90095. E-mail: jmmurphy@mednet.ucla.edu

Current address for Christopher M Waldmann: Department of Nuclear Medicine, University Medical Center Mainz, Germany

Current address for R Tavaré: Regeneron Pharmaceuticals, Inc., Tarrytown, NY 10591

Current address for KA Zettlitz and AM Wu: Department of Molecular Imaging and Therapy, Beckman Research Institute, City of Hope, Duarte, CA 91010

Short running title: Dual-modality linker for immunoPET/FIGS

Words: 5420
Figures: 5; Tables: 2
References: 33

ABSTRACT

Rationale

Antibody-based dual-modality (PET/fluorescence) imaging enables both pre-surgery antigen-specific immunoPET for non-invasive whole-body evaluation and intra-operative fluorescence for visualization of superficial tissue layers for image guided surgery.

Methods

We developed a universal dual-modality linker (DML) that facilitates 1) site-specific conjugation to a cysteine residue bearing antibody fragment; 2) introduction of a commercially available fluorescent dye (via amine-reactive prosthetic group); 3) rapid and efficient radiolabeling via click chemistry with ^{18}F-labeled *trans*-cyclooctene (^{18}F-TCO).

To generate a dual-modality antibody fragment-based imaging agent, the DML was labeled with the far-red dye sulfo-Cy5 (sCy5), site-specifically conjugated to the C-terminal cysteine of the anti-prostate stem cell antigen (PSCA) cys-diabody A2 (A2cDb), and subsequently radiolabeled by click chemistry with ^{18}F-TCO. The new imaging probe was evaluated in a human PSCA-positive prostate cancer xenograft model by sequential immunoPET and optical imaging. Uptake in target tissues was confirmed by ex vivo biodistribution.

Results

We successfully synthesized a dual-modality linker (DML) for conjugation of a fluorescent dye and fluorine-18. The anti-PSCA A2cDb was site-specifically conjugated with either DML or DML-sCy5 and radiolabeled via click chemistry with ^{18}F-TCO. ImmunoPET imaging confirmed in vivo antigen-specific targeting of prostate cancer xenografts as early as 1 h post injection. Rapid renal clearance of the 50 kDa antibody fragment enables same-day imaging. Optical imaging showed antigen-specific fluorescent signal in PSCA-positive xenografts and high contrast to surrounding tissue and PSCA-negative xenografts.

Conclusion

The dual-modality linker (DML) enables site-specific conjugation away from the antigen-binding site of antibody fragments, with controlled linker-to-protein ratio and combines signaling moieties for two imaging systems into one molecule. Dual-modality imaging could provide both non-invasive whole-body imaging with organ level biodistribution and fluorescent image guided identification of tumor margins during surgery.

Key Words: immuno-PET, fluorescence image-guided surgery (FIGS), cys-diabody, fluorine-18, click chemistry

INTRODUCTION

Although a variety of molecular imaging modalities are available, no single one provides overall structural, functional, and molecular information. Combining two signaling moieties in one molecule can provide complementary imaging applications; therefore, targeted multi-modality imaging and theranostics approaches are becoming more popular (*1*). Ideally, dual-modality imaging would facilitate whole-body imaging for staging and surgical planning, as well as real time imaging for guided surgery and could improve patient outcomes especially in cancers with curative surgery as the primary treatment option (e.g. prostate or pancreatic cancer) (*2,3*). One promising combination is dual-modality positron emission tomography (PET) and fluorescence imaging, which enables a preoperative whole-body evaluation of tumor location and burden and fluorescence guidance to identify positive tumor margins and/or local metastases (fluorescence image-guided surgery, FIGS).

Targeted dual-modality imaging requires selecting a favorable combination of radionuclide and fluorescence dye, an antigen-specific targeting moiety with suitable pharmacokinetics for imaging, and a conjugation technique that results in a predictable and consistent product (*1,4*). Monoclonal antibodies (mAbs) show high antigen specificity and affinity, making them valuable targeting vectors both for imaging and therapy. IgGs contain numerous reactive amino acids available for conjugation to chelators or radionuclides and fluorescent dyes and a variety of therapeutic mAbs against tumor targets (e.g. EGFR, HER-2, CD20, EpCAM, PSMA) have been studied as dual-modality imaging agents for preclinical imaging (*1,5*). Major disadvantages of using full-length IgGs for imaging are the long half-life, delaying imaging (4-6 days post injection, p.i.), and unwanted biological effects mediated by the Fc portion.

However, antibodies can be engineered into smaller fragments with optimized pharmacokinetics, such as diabodies (scFv dimer, ca. 50 kDa) that exhibit rapid localization to antigen expressing tumor tissue (peak uptake: 1-2 h p.i.) and sufficient clearance from normal

tissues and blood pool (half-life: 2-5 h, in mice) to facilitate high-contrast imaging within a few hours post tracer injection (*6*). Removal of the Fc domain eliminates interaction with the immune system and FcRn recycling, resulting in biological inertness. Diabodies can be further engineered to contain C-terminal cysteine residues (cys-diabody, cDb) that enable site-specific conjugation opposite from the antigen-binding site through thiol-reactive groups (*7*). Site-specific labeling result in more homogeneous and better defined constructs, prevents interference with antigen binding, and allows a precisely controlled load-to-protein ratio (*8*).

Fluorescence image guidance during surgery has become available for clinical trials due to specialized intraoperative imaging systems with acquisition times that enable real-time imaging (*9,10*). Most antibody-based probes in clinical trials use near-infrared fluorescent dyes (NIRF, ~700-1000 nm), such as IRDye800CW, because tissue exhibits almost no autofluorescence in the NIR spectrum and NIR light can be detected at millimeters tissue depth (*11*).

We have previously targeted the anti-prostate stem cell antigen (PSCA) for dual-modality imaging of prostate and pancreatic cancer by conjugating the cys-minibody A11cMb and the cys-diabody A2cDb with near-infrared fluorescent dyes (Cy5.5 or IRDye800CW, site-specifically) and iodine-124 or zirconium-89 (random labeling to tyrosine or lysine residues, respectively) (*12,13*). However, we believe, the antibody fragment-based dual-modality imaging approach can be improved by choosing a more favorable fluorescent dye, positron emitter and conjugation method.

The far-red dye sulfonate Cyanine 5 (sCy5, ex 646 nm, em 662 nm) offers an attractive alternative to IRDye800CW for conjugation to smaller antibody fragments, adding less molecular weight (~780 Da), less charge (net charge -1) and allowing conjugation in aqueous solutions. The high absorption coefficient and reasonable quantum yield (0.27) result in excellent brightness. Furthermore, cyanine-based dyes are residualizing, and the significant retention in cells (several days) extents the detection window for the fluorescent signal (*14,15*).

The fast pharmacokinetics of the cys-diabody format align with the half-life of fluorine-18 ($t_{1/2}$ 110 min), which offers excellent imaging properties (97% positron emission or β^+ decay, mean positron range 0.6 mm). Because fluorine-18 is widely available and ^{18}F-FDG is commonly used, clinicians are accustomed to both acquisition and interpretation of ^{18}F-FDG-PET scans, and transition towards ^{18}F-labeled diabody scans should be straightforward.

The conjugation of short-lived radionuclides is complicated by elaborate procedures under time constraint and in conditions that might damage the protein or the fluorescent dye. Rapid bioorthogonal reactions with high second-order rate constants (click chemistry) could overcome these challenges for ^{18}F-labeling of proteins (*16*). The inverse electron demand [4+2] Diels-Alder (IEDDA) reaction between 1,2,4,5-tetrazines (TZ) and *trans*-cyclooctene (TCO) is an extremely rapid cycloaddition, proceeds without a catalyst and is effective under mild conditions (neutral pH, room temperature) (*17,18*).

We developed a universal multi-functional dual-modality linker (DML) to enable site-specific conjugation to engineered cysteine residues, conjugation of fluorescent dyes via amine-reactive groups and rapid ^{18}F-labeling via click chemistry. To generate a dual-modality antibody-based imaging agent, the DML was labeled with sCy5, site-specifically conjugated to the C-terminal cysteine of A2cDb and subsequently radiolabeled by click chemistry with ^{18}F-TCO. The new imaging probe (^{18}F-DMLsCy5-A2cDb) was evaluated in a human PSCA-positive prostate cancer xenograft model by sequential immunoPET and optical imaging.

MATERIALS AND METHODS

Dual-Modality Linker (DML) Synthesis

A detailed description of the linker synthesis can be found in the supplementary information. In short, the linker scaffold was prepared by conjugation of mal-amido-PEG_2-NHS (Broadpharm) with *N*-α-*tert*-butyloxycarbonyl-*L*-lysine (Combi-Blocks). Subsequent introduction of an amino-functionalized tetrazine moiety via peptide coupling, removal of the *tert*-butyloxycarbonyl protecting group from *L*-lysine and coupling of the amine-reactive sulfo-cyanine5 NHS ester (Lumiprobe) concluded the synthesis of DML-sCy5. The purity was assessed by high performance liquid chromatography (HPLC) and the identity confirmed by electrospray ionization-mass spectrometry.

Site-Specific Conjugation of the Dual-Modality Linker to A2cDb

Generation and production of the anti-PSCA cys-diabody 2B3 A2 (A2cDb) were previously described (*19,20*). DML or DML-sCy5 (3-5-fold molar excess) was incubated with reduced (TCEP, 1 h, 22°C) A2cDb (100 µg/50 µL) for 2 h at room temperature or overnight at 4°C. Conjugates were separated from excess linker using Micro Bio-Spin size exclusion columns (BioRad) pre-blocked with PBS, 1%FBS. Dye-to-protein ratio was determined by measuring protein (280 nm) and dye (650 nm, correction factor 0.04) concentration on a NanoDrop 2000.

Conjugates were analyzed by SDS-PAGE and by size exclusion chromatography using a Superdex-75 HR10/30 column in an Äkta purifier (GE Healthcare).

Binding to human PSCA-expressing prostate cancer cells (22Rv1-PSCA) was analyzed by flow cytometry (*21*). Cells were incubated with serial dilutions of A2cDb-DMLsCy5 for 2 h at 4°C and after washing were analyzed using a LSRFortessa™ X-20 Sorp (BD Biosciences). Data were analyzed using FlowJo (version 9.3.2) and were fitted to a one-site-saturation binding model in Prism 7 (GraphPad Software, Inc.). The apparent affinity was calculated from three independent binding curves.

Radiosynthesis of 2-[^{18}F]-(*E*)-5-(2-Fluoroethoxy)cyclooct-1-ene (^{18}F-TCO) and Radiolabeling of A2cDb-DML by Click Chemistry

^{18}F-TCO was synthesized using the ELIXYS FLEX/CHEM automated radiochemical synthesizer (Sofie Biosciences) and eluted in DMSO:0.5% sodium-ascorbate solution 1:1 (v/v) as previously described (*22*). More details can be found in the supplementary information (*22-24*).

^{18}F-TCO (37-111 MBq) was added to A2cDb-DML or A2cDb-DMLsCy5 (100-300 µg in PBS) to a final DMSO concentration of 10% and incubated at room temperature for 10 minutes. Labeling efficiency was determined by ITLC (ITLC strips for monoclonal antibody preparation, Biodex Medical Systems) with acetonitrile as solvent and gamma counted in a Wizard 3' 1480 Automatic Gamma Counter (Perkin Elmer). Radiolabeled antibody fragments were purified using Micro Bio-spin columns and radiochemical purity was determined by ITLC as described above. The immunoreactive fraction was determined by incubating a trace amount (<0.5 pmol) of ^{18}F-DML-A2cDb with excess antigen expressing cells (22Rv1-PSCA) for 1 h at room temperature and gamma counting supernatant versus cell bound activity.

Prostate Cancer Xenograft Mouse Model (22Rv1-PSCA)

All procedures performed involving animals were approved by the University of California Los Angeles Chancellor's Animal Research Committee.

Cell lines 22Rv1 and 22Rv1-PSCA were cultured in RPMI1640, 10% FBS (*21*) and tumors were inoculated subcutaneously (1x10^6 cells/100 µL in 1:1 PBS:Matrigel (BD Biosciences)) in the shoulder of male nude mice (8-12 weeks, ~25 g, JAX002019, Jackson Laboratories) as previously described (*13*).

ImmunoPET/CT and Near-Infrared Fluorescence (NIRF) Imaging

Approximately 10 µg (3-4.8 MBq) of ^{18}F-DML-A2cDb or ^{18}F-DMLsCy5-A2cDb were injected into the tail vein of tumor bearing mice (3-4 mice/group, n=2). Mice were anesthetized with

1.5% isoflurane and small animal PET scans (Inveon PET, Siemens) were acquired for 60 min (dynamic scan), followed by static 10-min scans at 2 and 4 hours p.i. Images were reconstructed using OSEM-MAP algorithms (ordered subset expectation maximization-maximum a posteriori), overlaid with CT scans (CrumpCAT, UCLA in-house small animal scanner) and shown as whole body MIP (maximum intensity projection).

Optical imaging was conducted post mortem with the skin removed or of dissected tumors and organs ex vivo using the IVIS Lumina II system (PerkinElmer) with settings: 675 ex/694 em (Cy5.5) and 5 sec exposure time. Living Image Software (IVIS Imaging Systems, PerkinElmer) was used to display fluorescence/visible light overlays.

ROI Analysis and Ex Vivo Biodistribution

PET image analysis was performed using AMIDE (*25*). For quantitative region of interest (ROI) analysis the mean voxel value was converted to percent injected dose per gram (%ID/g_{ROI}, assuming a tissue density of 1 g/mL) using the decay-corrected injected dose and empirically determined cylinder factor for ^{18}F in the Inveon PET scanner. Partial volume correction was not applied, due to the complexity of organ shape, volume and proximity to organs with high activity.

Ex vivo biodistributions were performed after PET and optical imaging (4 h p.i.). Organs and tissues were collected, weighed and gamma counted. The %ID/g was calculated based on a standard containing 1% of the injected dose.

Statistical Analysis

Radiolabeling values are reported as mean ± SD. Ex vivo biodistribution data are shown as box-and-whiskers (min to max) plots and values reported as mean ± SEM. For statistical analysis multiple t tests (Holm-Sidak method, with alpha = 0.05) were performed (Prism 7, GraphPad Software, Inc.).

RESULTS

Synthesis of the Dual-Modality Linker (DML)

We designed and successfully synthesized a multifunctional linker (Fig. 1A) that contains functional groups for 1) site-specific conjugation to engineered antibody fragments by thiol-reactive maleimide; 2) incorporation of a fluorescent dye via amine-reactive NHS ester and 3) rapid and efficient radiolabeling by the reaction of 1,2,4,5-tetrazine with ^{18}F-labeled *trans*-cyclooctene (^{18}F-TCO) via the bioorthogonal inverse electron-demand [4+2] cycloaddition (click chemistry). Starting from α-boc-*L*-lysine, the synthesis was achieved in two steps. The purity was >95% as confirmed by HPLC.

Site-Specific Conjugation of the Dual-Modality Linker to A2cDb

The DML was deprotected and conjugated with sulfo-cyanine5 NHS ester (DMLsCy5, Fig. 1B) followed by conjugation to the reduced C-terminal cysteine residues of the anti-PSCA A2 cys-diabody (A2cDb-DML-sCy5) (Fig. 1C).

Successful conjugation of the DML or DML-sCy5 to A2cDb was confirmed by SDS-PAGE analysis (denaturing, non-reducing conditions). The unconjugated cys-diabody predominantly exists as a covalent dimer migrating at 50 kDa (theoretical M_W 50.6 kDa). With the C-terminal interchain disulfide bridge reduced and conjugated to DML or DML-sCy5 the majority of the protein migrates at ~25 kDa, corresponding to the molecular weight of the monomer. The blue sCy5 can be seen under white light concurrent with the monomer band of A2cDb-DMLsCy5 (Fig. 2A). Purity and integrity of the conjugated A2cDb (non-covalent dimer) was confirmed by size exclusion chromatography (Fig. 2B). Both A2cDb-DML and A2cDb-DMLsCy5 eluted as single peaks at similar elution times as the unconjugated A2cDb (22.3 min), and A2cDb-DMLsCy5 showed a concurring peak for the fluorescent dye (650 nm). These results confirm that conjugation of the DML did not disrupt dimer formation of the cys-diabody. Specific binding of A2cDb-DMLsCy5 to cell surface expressed antigen was verified by flow cytometry

using the prostate cancer cell line 22Rv1 transduced to express PSCA (22Rv1-PSCA). The low nanomolar apparent affinity (K_D 4.3 ± 2.1 nM, n=3), as calculated from saturation binding curves, was unchanged compared with previously published data (*13,20*).

Radiofluorination of A2cDb-DML and A2cDb-DMLsCy5 using ^{18}F-TCO click chemistry was carried out within 10 minutes at room temperature and resulted in comparable specific activities (Table 1). Labeling efficiencies varied depending on the amount of ^{18}F-TCO that could be added to the reaction (limited by the final DMSO concentration of 10%). Radiochemical purity (after size exclusion spin column) and immunoreactive fraction were comparable between ^{18}F-DML-A2cDb and ^{18}F-DMLsCy5-A2cDb.

Non-Invasive Whole Body ^{18}F-ImmunoPET Imaging shows PSCA Specific Tumor Uptake

Single-modality ^{18}F-DML-A2cDb or dual-modality ^{18}F-DMLsCy5-A2cDb (10 µg/3-4.8 MBq) were injected intravenously into male nude mice bearing 22Rv1 (left shoulder) and 22Rv1-PSCA (right shoulder) xenografts (Fig. 3). Antigen-specific uptake of both tracers is seen in the PSCA-expressing tumor as early as 1 h p.i. (Fig. 3A,C) and is retained over the 4 h imaging study (Fig. 3B,D). Minimal activity in the negative tumor, presumably caused by blood pool activity, decreased over time. Clearance of ^{18}F-DML-A2cDb (Fig. 3A,B) appears to be primarily renal and activity is excreted into the urine (bladder), some clearance occurs through the hepatobiliary route and excretion of activity with the feces can be seen. The biodistribution of ^{18}F-DMLsCy5-A2cDb differed from single-modality ^{18}F-DML-A2cDb with higher blood pool activity at all time points (visible in the heart) and higher activity both in liver and kidneys (Fig. 3C,D). Importantly, specificity of both tracers is retained as PSCA-specific tumor uptake (22Rv1-PSCA) is higher compared with 22Rv1 and, despite the differing biodistributions, uptake in 22Rv1-PSCA is similar for both tracers over four hours.

Intraoperative Fluorescent Imaging Identifies PSCA-Positive Tumor Tissue

Following the last PET/CT scan (4 h p.i.), optical imaging of the same mice was performed post mortem with the skin removed (mimicking a surgical setting) using the IVIS Lumina II system. Fluorescent signal was detected in the PSCA-positive xenografts of mice injected with ^{18}F-DMLsCy5-A2cDb (Fig. 4A). Signal intensity was higher in 22Rv1-PSCA tumors (right shoulder) compared with the 22Rv1 tumors (left shoulder) and with surrounding tissue. Tumors were further analyzed ex vivo to compare the relative fluorescence signals without interference from other organs or autofluorescence from the skin (Fig. 4B). While ^{18}F-DMLsCy5-A2cDb clearly distinguishes PSCA-positive from negative tumors, no signal is detected in tumors from the ^{18}F-DML-A2cDb group. Fluorescence imaging of excised organs and tissues showed expected autofluorescence in the stomach, intestine and to a lesser extent in the kidneys of mice injected with ^{18}F-DML-A2cDb (Fig. S1). In the ^{18}F-DMLsCy5-A2cDb group, higher fluorescent signal is detected in the organs of clearance: liver, gall bladder, spleen and kidneys, consistent with the immunoPET images.

Quantitative ROI Analysis and Ex Vivo Biodistribution

Quantitative ROI analysis of ^{18}F-DML-A2cDb immunoPET showed rapid blood clearance, renal clearance/excretion and antigen-specific retention of the tracer in the tumor (22Rv1-PSCA). ^{18}F-DMLsCy5-A2cDb immunoPET revealed a larger fraction of the tracer clearing through the liver and slower decrease of activity in the kidneys (Fig. 5A).

Ex vivo biodistributions (4 h p.i., Fig. 5B, Table 2) confirmed that uptake in PSCA-expressing tumors was similar for ^{18}F-DML-A2cDb and the dual-modality ^{18}F-DMLsCy5-A2cDb (2.8 ± 1.1 and 2.9 ± 0.4 %ID/g, respectively) and was significantly higher than in 22Rv1 tumors (0.3 ± 0.1 and 0.8 ± 0.2 %ID/g, respectively, $p<0.05$ for both). The longer retention of ^{18}F-DMLsCy5-A2cDb radioactive signal seen in the immunoPET scans was consistent with higher remaining activity in the liver (4.8 ± 0.3 %ID/g), kidneys (15.2 ± 1.1 %ID/g) and spleen (2.2 ±

0.2 %ID/g). In contrast, ^{18}F-DML-A2cDb shows the highest activity excreted in the intestine at 4 h p.i. (13.7 ± 2.7 %ID/g, including contents).

DISCUSSION

ImmunoPET imaging could improve diagnosis and surgical planning, and fluorescence image-guided surgery could enable more complete resection of diseased tissues in cancer patients that stand to benefit from surgery (e.g. pancreatic and prostate cancer). Combining both signaling moieties into a single agent guarantees direct correlation between the diagnostic imaging for surgical planning and the imaging used to direct surgery (*1*).

While the combination of PET and fluorescence imaging has been extensively studied, most approaches utilized intact antibodies and random conjugation methods, that result in a Poisson distribution of number of dye to protein (D/P) fractions with distinct pharmacokinetic characteristics (affinity, clearance and distribution, fluorescence quenching and residualizing of metabolites) (*26*). Smaller antibody fragments exhibit optimized pharmacokinetics for imaging (better tumor penetration and faster clearance) and can be combined with shorter-lived radionuclides to reduce the radiation dose to healthy tissues (compared to traditional immunoPET with IgGs and long-lived isotopes). However, because of their smaller size, antibody fragments are all the more prone to undergo changes in tissue retention and blood clearance upon modification with radionuclides, chelators or fluorescent dyes (depending on site, shape, size, hydrophobicity, and charge) (*27*). Thus, controlling the location and stoichiometry of modifications is critical.

We generated a universal multi-functional linker (dual-modality linker, DML) that allows consistent conjugation with a known number of linker per protein and to defined sites, thereby minimizing batch-to-batch heterogeneity and guaranteeing more predictable properties. Most importantly, two imaging moieties can be added to the protein with a single modification.

The DML was successfully labeled with sCy5 and site-specifically conjugated to the anti-PSCA A2 cys-diabody (A2cDb-DMLsCy5) and did not impair the dimeric conformation or binding characteristics of A2cDb. Radiofluorination was conducted using click chemistry within

10 minutes (^{18}F-DMLsCy5-A2cDb) and in vivo specificity was shown for both modalities by successive PET and fluorescence imaging of mice bearing PSCA-positive and negative xenografts. ^{18}F-immunoPET showed fast and specific tumor uptake and rapid clearance from circulation resulting in high contrast images as early as 1 hour post injection. Post mortem optical imaging confirmed high-contrast fluorescence in the PSCA-expressing tumors and excellent delineation of cancerous cells from surrounding tissue.

The exceptional speed of the IEDDA reaction facilitates the use of fluorine-18 (^{18}F, $t_{1/2}$ 109.8 min), which is well matched to the biological half-life of the diabody format. Williams et al compared different sized derivatives of the same full length IgG (scFv, diabody, minibody, F(ab')$_2$, IgG) with respect to affinity (K_D) and imaging figure of merit (IFOM), an indicator for how rapidly a statistically significant tumor image can be acquired (*28,29*). The analysis suggested that same-day imaging would be best accomplished with the diabody format (3 - 5 h interval post injection) and that if the IFOM was calculated for ^{18}F only the diabody was competitive, as the larger sized fragments have too long half-lives and the smaller monovalent scFv showed much shorter tumor retention. The in vivo results using ^{18}F-DMLsCy5-A2cDb presented in this work indeed show that same-day immunoPET imaging is feasible and further corroborate previous studies with ^{18}F-labeled diabodies in several models (HER2, CEA, CD20) (*29-31*).

While radioactive decay happens only once, the fluorescence dye can provide greater sensitivity for intraoperative guidance, because it can be repeatedly activated by excitation light. The long intracellular (lysosomal) half-life of sCy5 ($t_{1/2}$ 3.9 ± 0.5 days) further extends the possible time window between presurgical whole body immunoPET and FIGS (*15*).

The fluorescence dye sulfo-Cy5 was chosen for this study over the previously used IRDye800CW because we hypothesized that it would have less impact on the pharmacokinetic properties of the A2 cys-diabody due to its smaller size, lower charge and lower hydrophobicity. While the antigen-specific tumor uptake was similar between ^{18}F-DML-A2cDb

and ^{18}F-DMLsCy5-A2cDb, significant differences were observed for the clearance of the dual-modality tracer with longer retention times in liver, spleen and kidneys. This could be due to the relatively high dye-to-protein (D/P) ratio of 1.1 ± 0.3, since a study by Cilliers et al suggests that D/P ratios of 0.3 or less are necessary to limit the impact of fluorophores on antibody pharmacokinetics after comparing two IgGs (Herceptin and Avastin) labeled non-site-specifically with either IRDye800CW or AlexaFluor680 at different D/P ratios (*26*).

Because of the modular linker system the fluorophore can be easily exchanged if desired and because the linker-to-protein ratio is precisely controlled the D/P ratio can also be tailored, for example by mixing DML and DML-sCy5. Future studies will have to evaluate the dual-modality tracer ^{18}F-DMLsCy5-A2cDb with optimized D/P ratio in more relevant preclinical cancer models (orthotopic tumors or in transgenic mice) to assess sufficient contrast to surrounding tissues and the impact of tissue autofluorescence in the far-red light range. Another consideration is that normal tissue expression of PSCA in prostate, bladder and stomach is not reflected in the xenograft model because the A2cDb does not cross react with murine PSCA.

A limitation of the radiolabeling procedure was the low concentration of ^{18}F; this strained the kinetics in the labeling reaction due to the maximum amount of organic solvent the protein can be exposed to. However, future optimization of the radiosynthesis, purification and elution procedures should lead to higher ^{18}F-TCO concentration/specific activity and thus higher labeling efficiencies.

The high clinical relevance of targeted dual-modality probes for prostate cancer is reflected by the variety of ongoing preclinical studies exploring e.g. PSMA inhibitors, monoclonal antibodies or gastrin-releasing peptide receptor ligands for dual-modality imaging (*5,32,33*). Site-specific conjugation to engineered cysteine residues is well established and the DML could be broadly applied to antibody fragments, single domain antibodies or alternative

scaffolds targeting cell surface markers for molecular imaging with any combination of dual-modality PET/fluorescence. Alternative targeting moieties and tumor markers should be explored in future studies to confirm the universal applicability of the dual-modality linker. The precision and speed of the IEDDA reaction has also been shown to be feasible in vivo and the DML could be used for pretargeted imaging strategies (*34*,*35*).

CONCLUSION

This study presents a universal dual-modality linker for site-specific conjugation to antibody fragments via engineered cysteine residues. This linker enables stoichiometric conjugation of near-infrared fluorescence dyes away from the antigen binding site and the use of rapid and efficient click chemistry for radiolabeling with fluorine-18. Dual-modality imaging could provide both non-invasive whole body imaging to localize PSCA-positive cancer and fluorescence image guided identification of tumor margins and lymphatic spread.

DISCLOSURE

This work was supported by NIH R01 CA174294, the UCLA SPORE in Prostate Cancer NIH P50 CA092131, Department of Defense Synergistic IDEA Award W81XWH-15-1-0725 and by a generous gift from Ralph and Marjorie Crump to the Crump Institute. Small-animal imaging was funded in part by the UCLA Jonsson Comprehensive Cancer Center (JCCC) Support Grant (NIH CA016042). AM Wu is a member of the JCCC.

AM Wu holds ownership interest in and is a consultant/advisory board member for ImaginAb, Inc. The other authors disclosed no potential conflicts of interest.

ACKNOWLEDGEMENTS

We would like to thank the staff of the UCLA Biomedical Cyclotron and Dr. Umesh Gangadharmath for providing [^{18}F]fluoride for our study. We thank Felix B. Salazar for technical assistance and the UCLA Crump Preclinical Imaging Technology Center.

KEY POINTS

Question: Can antibody fragments be site-specifically conjugated for immuno-PET and fluorescence imaging using a novel dual-modality linker (DML)?

Pertinent findings: To generate a dual-modality antibody-based imaging agent, the DML was labeled with sCy5, site-specifically conjugated to the C-terminal cysteine of A2cDb and subsequently radiolabeled by click chemistry with ^{18}F-TCO. The new imaging probe (^{18}F-DMLsCy5-A2cDb) was evaluated in a human PSCA-positive prostate cancer xenograft model by sequential immunoPET and optical imaging and showed antigen-specific uptake in PSCA-expressing tumors.

Implications for patient care: The humanized antibody fragment could be translated into the clinic and provide both non-invasive whole body PET imaging to localize PSCA-positive cancer and fluorescence image guided identification of tumor margins during surgery.

REFERENCES

1. Azhdarinia A, Ghosh P, Ghosh S, Wilganowski N, Sevick-Muraca EM. Dual-labeling strategies for nuclear and fluorescence molecular imaging: a review and analysis. *Mol Imaging Biol.* 2012;14:261-276.

2. Bond-Smith G, Banga N, Hammond TM, Imber CJ. Pancreatic adenocarcinoma. *BMJ.* 2012;344:e2476.

3. Heidenreich A, Bastian PJ, Bellmunt J, et al. EAU guidelines on prostate cancer. part 1: screening, diagnosis, and local treatment with curative intent-update 2013. *Eur Urol.* 2014;65:124-137.

4. Lee S, Chen X. Dual-modality probes for in vivo molecular imaging. *Mol Imaging.* 2009;8:87-100.

5. Lutje S, Rijpkema M, Franssen GM, et al. Dual-modality image-guided surgery of prostate cancer with a radiolabeled fluorescent anti-PSMA monoclonal antibody. *J Nucl Med.* 2014;55:995-1001.

6. Olafsen T, Wu AM. Antibody vectors for imaging. *Semin Nucl Med.* 2010;40:167-181.

7. Olafsen T, Cheung CW, Yazaki PJ, et al. Covalent disulfide-linked anti-CEA diabody allows site-specific conjugation and radiolabeling for tumor targeting applications. *Protein Eng Des Sel.* 2004;17:21-27.

8. Adumeau P, Sharma SK, Brent C, Zeglis BM. Site-specifically labeled immunoconjugates for molecular imaging—part 1: cysteine residues and glycans. *Mol Imaging Biol.* 2016;18:1-17.

9. Gioux S, Choi HS, Frangioni JV. Image-guided surgery using invisible near-infrared light: fundamentals of clinical translation. *Mol Imaging.* 2010;9:237-255.

10. Vahrmeijer AL, Hutteman M, van der Vorst JR, van de Velde CJ, Frangioni JV. Image-guided cancer surgery using near-infrared fluorescence. *Nat Rev Clin Oncol.* 2013;10:507-518.

11. Te Velde EA, Veerman T, Subramaniam V, Ruers T. The use of fluorescent dyes and probes in surgical oncology. *Eur J Surg Oncol.* 2010;36:6-15.

12. Tsai WK, Zettlitz KA, Tavare R, Kobayashi N, Reiter RE, Wu AM. Dual-modality ImmunoPET/fluorescence imaging of prostate cancer with an anti-PSCA cys-minibody. *Theranostics.* 2018;8(21):5903-5914.

13. Zettlitz KA, Tsai WK, Knowles SM, et al. Dual-Modality Immuno-PET and Near-Infrared Fluorescence Imaging of Pancreatic Cancer Using an Anti-Prostate Stem Cell Antigen Cys-Diabody. *J Nucl Med.* 2018;59:1398-1405.

14. Hughes LD, Rawle RJ, Boxer SG. Choose your label wisely: water-soluble fluorophores often interact with lipid bilayers. *PLoS One.* 2014;9:e87649.

15. Cilliers C, Liao J, Atangcho L, Thurber GM. Residualization rates of near-infrared dyes for the rational design of molecular imaging agents. *Mol Imaging Biol.* 2015;17:757-762.

16. Lang K, Chin JW. Bioorthogonal reactions for labeling proteins. *ACS Chem Biol.* 2014;9:16-20.

17. Li Z, Cai H, Hassink M, et al. Tetrazine-trans-cyclooctene ligation for the rapid construction of 18F labeled probes. *Chem Commun (Camb).* 2010;46:8043-8045.

18. Reiner T, Zeglis BM. The inverse electron demand Diels-Alder click reaction in radiochemistry. *J Labelled Comp Radiopharm.* 2014;57:285-290.

19. Lepin EJ, Leyton JV, Zhou Y, et al. An affinity matured minibody for PET imaging of prostate stem cell antigen (PSCA)-expressing tumors. *Eur J Nucl Med Mol Imaging.* 2010;37:1529-1538.

20. Sonn GA, Behesnilian AS, Jiang ZK, et al. Fluorescent Image-Guided Surgery with an Anti-Prostate Stem Cell Antigen (PSCA) Diabody Enables Targeted Resection of Mouse Prostate Cancer Xenografts in Real Time. *Clin Cancer Res.* 2016;22:1403-1412.

21. Saffran DC, Raitano AB, Hubert RS, Witte ON, Reiter RE, Jakobovits A. Anti-PSCA mAbs inhibit tumor growth and metastasis formation and prolong the survival of mice bearing human prostate cancer xenografts. *Proc Natl Acad Sci U S A.* 2001;98:2658-2663.

22. Collins J, Waldmann CM, Drake C, et al. Production of diverse PET probes with limited resources: 24 (18)F-labeled compounds prepared with a single radiosynthesizer. *Proc Natl Acad Sci U S A.* 2017;114:11309-11314.

23. Molander GA, Shin I. Synthesis and Suzuki-Miyaura cross-coupling reactions of potassium Boc-protected aminomethyltrifluoroborate with aryl and hetaryl halides. *Org Lett.* 2011;13:3956-3959.

24. Yang J, Karver MR, Li W, Sahu S, Devaraj NK. Metal-catalyzed one-pot synthesis of tetrazines directly from aliphatic nitriles and hydrazine. *Angew Chem Int Ed Engl.* 2012;51:5222-5225.

25. Loening AM, Gambhir SS. AMIDE: a free software tool for multimodality medical image analysis. *Mol Imaging.* 2003;2:131-137.

26. Cilliers C, Nessler I, Christodolu N, Thurber GM. Tracking Antibody Distribution with Near-Infrared Fluorescent Dyes: Impact of Dye Structure and Degree of Labeling on Plasma Clearance. *Mol Pharm.* 2017;14:1623-1633.

27. Boswell CA, Tesar DB, Mukhyala K, Theil FP, Fielder PJ, Khawli LA. Effects of charge on antibody tissue distribution and pharmacokinetics. *Bioconjug Chem.* 2010;21:2153-2163.

28. Williams LE, Wu AM, Yazaki PJ, et al. Numerical selection of optimal tumor imaging agents with application to engineered antibodies. *Cancer Biother Radiopharm.* 2001;16:25-35.

29. Cai W, Olafsen T, Zhang X, et al. PET imaging of colorectal cancer in xenograft-bearing mice by use of an 18F-labeled T84.66 anti-carcinoembryonic antigen diabody. *J Nucl Med.* 2007;48:304-310.

30. Olafsen T, Sirk SJ, Olma S, Shen CK, Wu AM. ImmunoPET using engineered antibody fragments: fluorine-18 labeled diabodies for same-day imaging. *Tumour Biol.* 2012;33:669-677.

31. Zettlitz KA, Tavare R, Collins J, et al. 18F-labeled anti-human CD20 cys-diabody for same-day immunoPET in a model of aggressive B-cell lymphoma in human CD20 transgenic mice. *Eur J Nucl Med Mol Imaging.* 2018;259:*in press*.

32. Baranski AC, Schafer M, Bauder-Wust U, et al. PSMA-11-Derived Dual-Labeled PSMA Inhibitors for Preoperative PET Imaging and Precise Fluorescence-Guided Surgery of Prostate Cancer. *J Nucl Med.* 2018;59:639-645.

33. Zhang H, Desai P, Koike Y, et al. Dual-Modality Imaging of Prostate Cancer with a Fluorescent and Radiogallium-Labeled Gastrin-Releasing Peptide Receptor Antagonist. *J Nucl Med.* 2017;58:29-35.

34. Denk C, Svatunek D, Filip T, et al. Development of a (18) F-labeled tetrazine with favorable pharmacokinetics for bioorthogonal PET imaging. *Angew Chem Int Ed Engl.* 2014;53:9655-9659.

35. Devaraj NK, Weissleder R. Biomedical applications of tetrazine cycloadditions. *Acc Chem Res.* 2011;44:816-827.

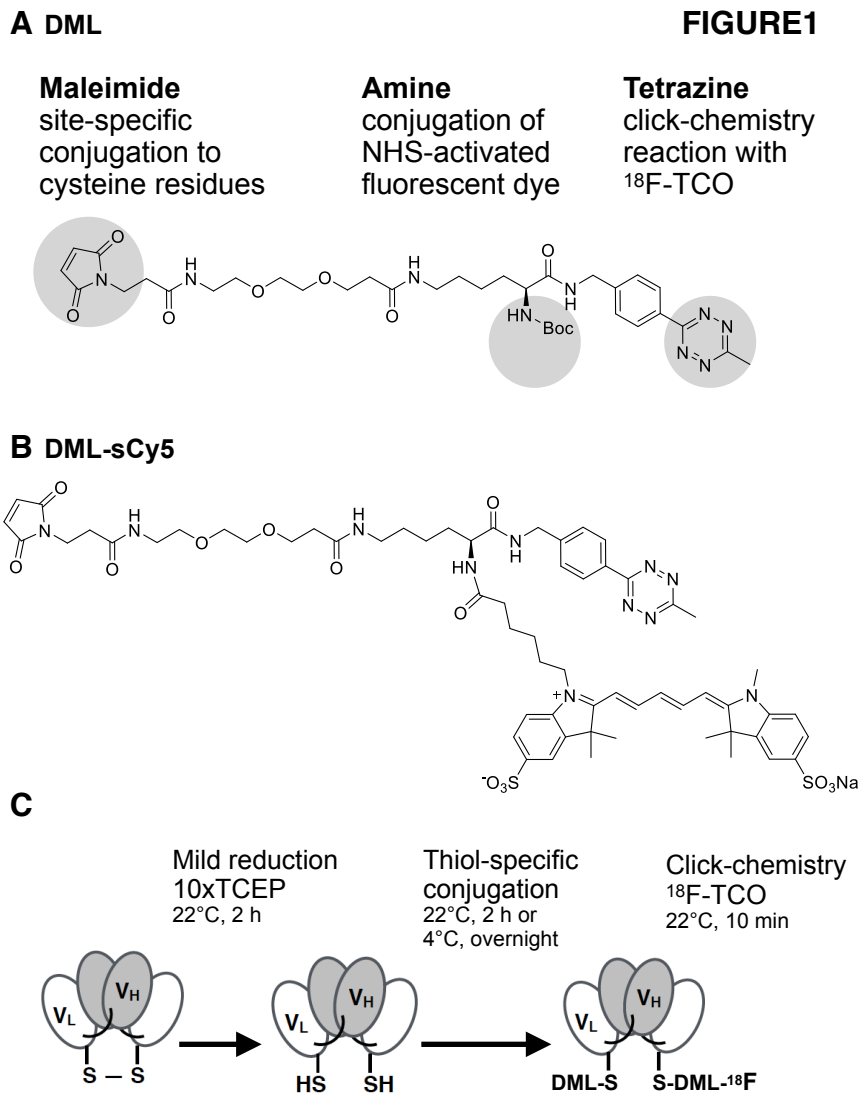

FIGURE 1. Concept: Dual-modality linker. A) Structure of the dual-modality linker (DML) containing three functional groups. **B)** Sulfo-Cyanine5 NHS ester was conjugated to the amine group (DML-sCy5). **C)** Schematic of site-specific conjugation and radiolabeling. Reducing the A2 cys-diabody C-terminal disulfide-bridge presents thiol groups for conjugation with the maleimide group. Radiofluorination is achieved by click-chemistry using ^{18}F-TCO. TCEP = tris(2-carboxyethyl)phosphine; V$_H$ = heavy-chain variable domain; V$_L$ = light-chain variable domain; TCO = *trans*-cyclooctene.

FIGURE2

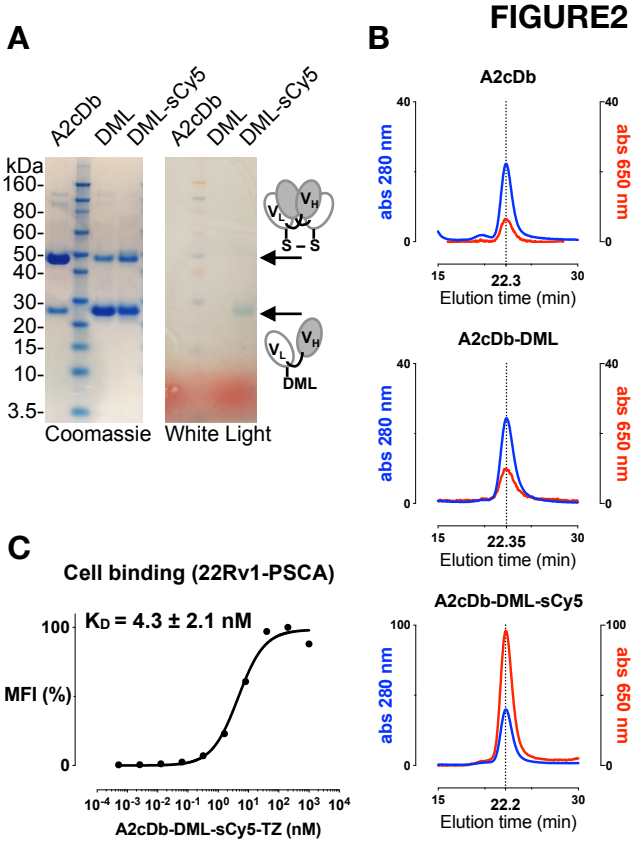

FIGURE 2. Biochemical characterization of the DML-conjugated A2 cys-diabody. A) SDS-PAGE analysis of A2cDb and site-specifically conjugated A2cDb under non-reducing conditions: Coomassie -stained (left) and unstained (right). **B)** Size exclusion chromatography of A2cDb (top panel), A2cDb-DML (middle panel) and A2cDb-DML-sCy5 (bottom panel) show similar elution profiles for the protein (280 nm). The fluorescent dye (sCy5, 650 nm) elutes at the same time as the protein (22.2 min) confirming conjugation to the A2cDb. **C)** Binding of A2cDb-DML-sCy5 to 22Rv1-PSCA cells analyzed by flow cytometry. The saturation binding curve of one of three independent experiments is shown. The apparent affinity of A2cDb_DML-sCy5 was calculated using a single-site specific binding model.

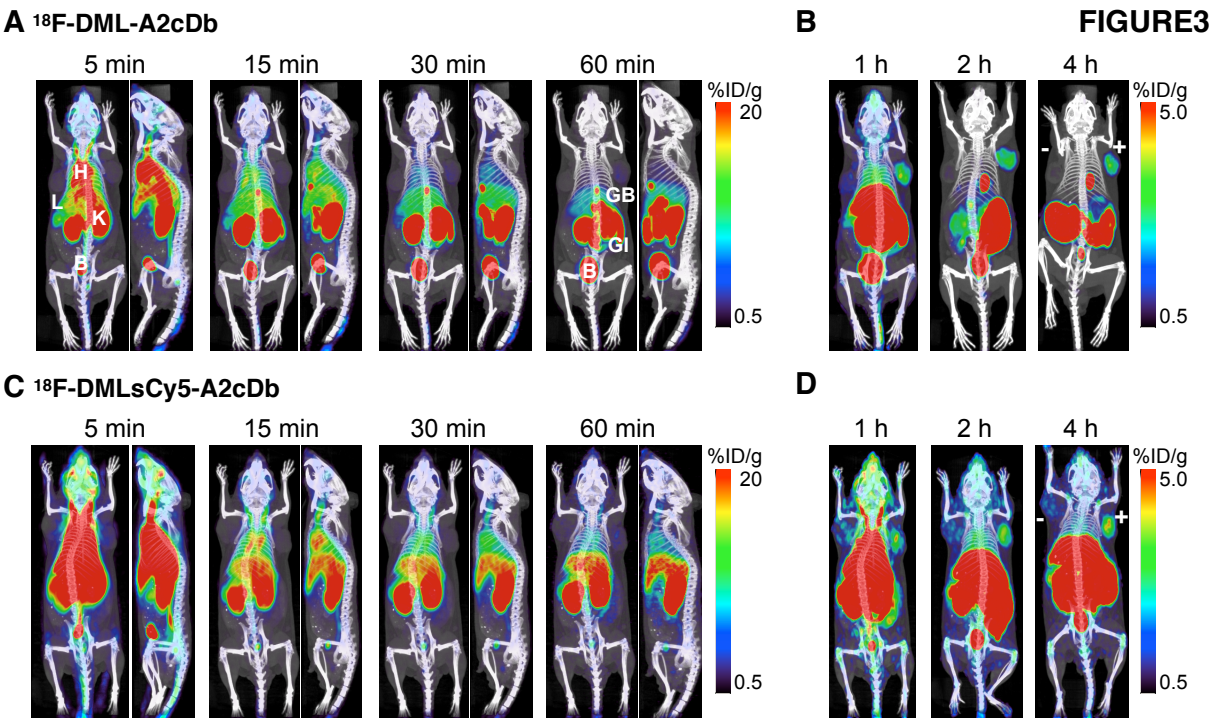

FIGURE 3. ImmunoPET imaging shows antigen-specific uptake in PSCA-positive prostate cancer xenografts. Nude mice bearing PSCA-negative (22Rv1, left shoulder) and PSCA-positive (22Rv1-PSCA, right shoulder) subcutaneous xenografts were imaged with **A)** single modality ^{18}F-DML-A2cDb, 60-min dynamic scan and **B)** 10-min static scans at 1, 2 and 4 h p.i. or **C)** dual-modality ^{18}F-DMLsCy5-A2cDb, 60-min dynamic scan and **D)** 10-min static scans at 1, 2 and 4 hours p.i. Depicted are representative scans (of $n \geq 6$) as whole-body maximum intensity projection small-animal PET/CT overlays.

FIGURE4

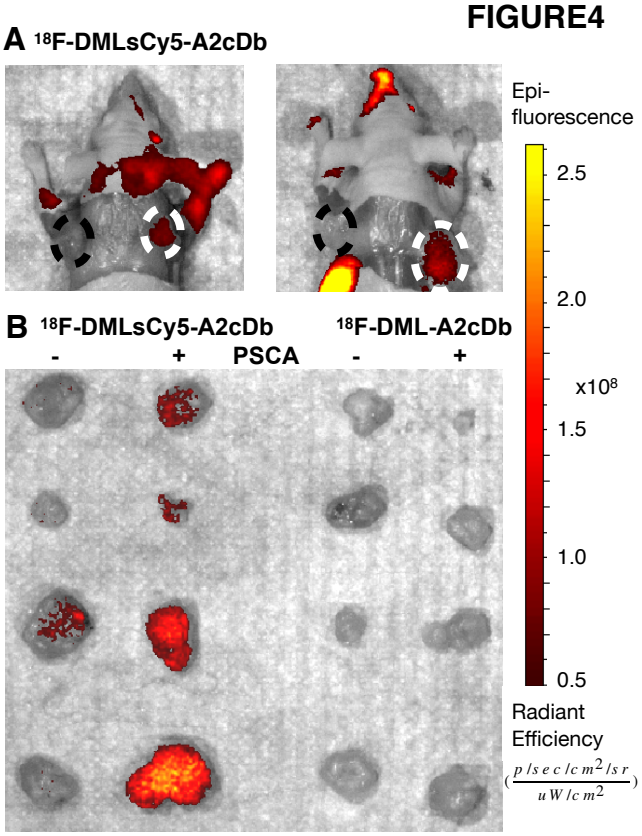

FIGURE 4. The same mice were assessed by optical imaging. A) Post mortem optical imaging of mice with skin removed. Mice injected with dual-modality ^{18}F-DMLsCy5-A2cDb show antigen-specific fluorescence signal in the PSCA-positive tumor on the right shoulder (dashed white circle). Two representative mice (of n = 7) are shown. **B)** 22Rv1 (-) and 22Rv1-PSCA (+) xenografts were analyzed ex vivo to compare the relative fluorescent signal without obstruction from other organs.

FIGURE5

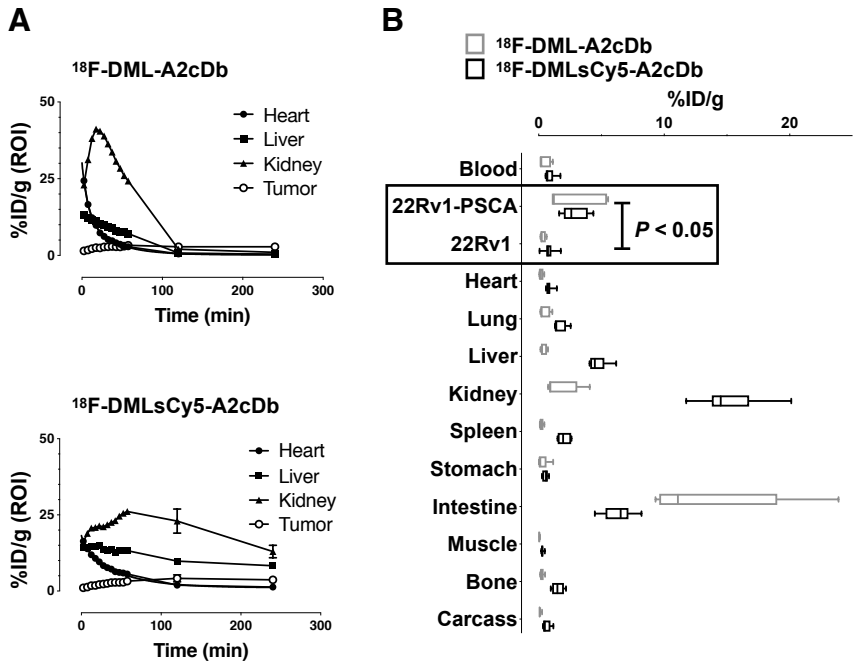

FIGURE 5. Quantitative ROI analysis and ex vivo biodistribution. A) Quantitative ROI analysis of blood (heart), liver, kidney and 22Rv1-PSCA (tumor). **B)** Ex vivo biodistribution 4 h p.i. of ^{18}F-DML-A2cDb (n=6) and ^{18}F-DMLsCy5-A2cDb (n=7). Tumors and organs were harvested and gamma counted. Depicted as box-and-whiskers (min to max) plots.

TABLE 1. Radiolabeling of A2cDb using ^{18}F-TCO click chemistry.

	^{18}F-DML-A2cDb		^{18}F-DMLsCy5-A2cDb	
	Mean	SD	Mean	SD
Dye-to-protein ratio	n.d.		1.07	0.26
Labelling Efficiency [%]	77.1	17.7	52.7	18.6
Specific Activity [MBq/µg]	0.41	0.12	0.50	0.30
Radiochemical Purity [%]	97.3	1.6	89.1	10.6
Immunoreactivity [%]	42.9	8.7	41.5	6.9
N	3		3	

TABLE 2. Ex vivo biodistribution 4 h p.i. Values are depicted as %ID/g Mean ± Standard error of mean.

	^{18}F-DML-A2cDb		^{18}F-DMLsCy5-A2cDb	
	Mean	SEM	Mean	SEM
Blood	0.44	0.19	0.90	0.17
22Rv1-PSCA (pos)	2.84	1.07	2.89	0.38
22Rv1 (neg)	0.32	0.09	0.82	0.19
Heart	0.18	0.07	0.85	0.11
Lung	0.44	0.17	1.67	0.19
Liver	0.37	0.10	4.81	0.29
Kidney	1.71	0.56	15.2	1.1
Spleen	0.21	0.06	2.02	0.17
Stomach	0.31	0.10	0.54	0.08
Intestine	13.7	2.7	6.37	0.46
Muscle	0.05	0.01	0.30	0.04
Bone	0.25	0.06	1.53	0.17
Carcass	0.11	0.04	0.66	0.13
N	6		7	